Nano-particles carried by multiple dynein motors: A Self-Regulating Nano-Machine

Fayer, I.[a] & Halbi, G.[b], Aranovich, D.[b], Gat, S.[b], Bar, S.[b], Erukhimovitch, V.[b], Rony Granek[a,c,*], Anne Bernheim-Groswasser[b,c,*]

[a] The Stella and Avram Goren-Goldstein Department of Biotechnology Engineering, Ben-Gurion University of the Negev, Beer Sheva 84105, Israel.

[b] The Department of Chemical Engineering, Ben-Gurion University of the Negev, Beer Sheva 84105, Israel.

[c] The Ilse Katz Institute for Meso and Nanoscale Science and Technology, Ben-Gurion University of the Negev, Beer Sheva 84105, Israel.

* Corresponding authors: Rony Granek & Anne Bernheim-Groswasser

E-mails: rgranek@bgu.ac.il, bernheim@bgu.ac.il

Classification

Keywords

active transport, processivity time, intracellular transport, nano-particles, nano-carriers, dynein, helical motion, obstacle bypassing, self-regulation, smart design, multi-motor complex.

Author Contributions

Anne Bernheim-Groswasser – development of experimental setup model, analysis of results, writing the article.

Rony Granek – development of the theoretical model, analysis of results, writing the article.

Itay Fayer – development of the theoretical model and computer code, analysis of results, writing the article.

Gal Halbi – development of experimental model and carry-out of experiments, analysis of results, writing the article.

Dina Aranovich – development of experimental set-up model and carry-out of experiments and analysis of results.

Shachar Gat – development of experimental set-up model and carry-out of experiments and analysis of results.

Shy Bar – development of experimental set-up model and carry-out of experiments.

Vitaly Erukhimovitch – analysis of results.

Abstract

Native cargos achieve efficient intra-cellular active transport by recruiting multiple motors proteins from the cytoplasm. Here we investigate the motion of spherical nano-particles (NPs) – acting as model cargos – grafted with flexible polymers, each ending with a nuclear localization signal (NLS) peptide, thereby allowing recruitment of mammalian cytoplasmic dynein. Bead-motility assays show several unique features. As the number of motors increases, the run-time and run-length increase, the longitudinal velocity mean decreases, whereas its width shows a non-monotonous behavior. Moreover, both single and multi-motor NPs perform angular (i.e., projected transverse) motion. Strikingly, the directions of angular and longitudinal motions are correlated, such that retrograde steps are combined with right-handed motion. We formulate a theoretical model to simulate the multi-dynein transported NP. The model builds on a recently theoretical description of single yeast dynein stepping on the curved microtubule surface, modified to account for mammalian dynein, and generalized to include motor-motor elastic and excluded-volume coupling. The simulation results are majorly in agreement with our experimental results. Moreover, long time trajectories exhibit both left- and right- handed helical motion around the MT symmetry axis, consistent with the measured and simulated angular velocity. The model gives further insight into the mechanism of the NP motion and suggests that the NPs are self-regulating the number of participating motors, optimizing between single motor, for obstacle bypassing, and multi-motor behavior, for persistent directional motion. We suggest that native cargos could use a similar mechanism to achieve efficient transport in the crowded cellular environment.

Significance Statement

The mechanism of active transport of native cargos, such as HIV, is a long-standing conundrum. Their need for persistence motion towards the nucleus, while bypassing obstacles in the super-crowded intracellular milieu, requires sophisticated natural design. To fathom this machinery, we study a smartly designed nano-particle that recruits *several* dynein motor-proteins from the cytoplasm. Motility assays and model simulations reveal long run-times, long run-lengths, and helical motion around the microtubule symmetry axis. Moreover, the nano-particles self-regulate the number of dyneins participating in the motion, which optimizes its motility properties. We suggest that alternating between single motor motility, which is beneficial for obstacle bypassing, and multiple motor states, which engender persistent motion towards the nucleus, the NP achieves optimal transport efficiency.

/body

Introduction

Active, motor-protein mediated transport is crucial for the intracellular conveying of a large variety of cargos in eukaryotes. Notably, microtubule-associated (MT-associated) motor proteins, dynein and kinesin, play here a cardinal role, hence, fueling a variety of vital biological processes (1-3). While dynein is responsible for transport towards the cell center, members of the kinesin family are mostly responsible for transport towards the cell periphery (4-7). The dynamic interplay between these two classes of motion orchestrates over the subcellular arrangement of organelles, e.g., mitochondria (8)p and Golgi-complexes (1). In addition, different types of viruses have evolved to harness the dynein machinery for efficient targeting of the nucleus, where the infection process of the host cell takes place. HIV and herpes-simplex virus, for instance, express nuclear localization signal (NLS) peptides (7) that recruit dynein from the cytoplasm (9-13). Likewise, adenoviruses use other ligands (e.g., hexon) for engaging the active transport mechanisms (14, 15). Recently, preliminary theoretical work has been performed to mimic these viruses in rationally designed cargos that could be used for drug delivery applications (16).

While knowledge of single dynein motility has been extensively increasing in the last decade (17-23), much less is known about the collective motility of multiple motors as they carry a single cargo. Several observations lead to the prevailing belief that native cargos are carried by more than one motor (24-28). Studies of supercoiled DNA plasmids enriched by NFκB receptors showed robust nuclear temporal localization (29), supporting multiple dynein recruitment mediated by NLS binding. Complexes of fluorescently labeled single-stranded DNA, such as the VirE2 protein of Agrobacterium and the VirE2 itself, contain putative NLS regions that can recruit dynein (30).

The collective behavior of motor proteins carrying a single cargo is often described in oversimplified terms such as cooperative or agonistic behavior (where motors walk at unison) *vs.* antagonistic (where motors interfere with each other walk) (31-35). Nevertheless, this distinction is far from being clear cut. Moreover, recently, complex modes of motion have also been observed, in particular, a remarkable helical motion of dynein coated beads, demonstrating both right- and left- handed helices (36-38). Notably, a theoretical description for the sideway motion of a *single* yeast dynein has been recently put forward (39), in qualitative accord with these experiments.

Previous theoretical works modeled certain features of multi-motor motion (16, 31, 32, 35, 40-46). Yet, these theoretical studies do not account for essential features for dynein stepping, e.g.,

they do not include the detailed locations of the dynein binding sites over the MT surface. In this spirit, as mentioned above, the *single motor* stepping was recently revisited to describe this two dimensional (2D) stepping of a single yeast dynein (39). The 2D stepping model correctly accounts for the measured longitudinal step-size distribution and predicts a broad angular distribution of steps with small right-handed bias.

Motivated by previous theoretical work (16), we present here combined experimental-theoretical research on a rationally designed particle that, on the one hand, can serve as a model particle for native cargos and, on the other hand, allows quantitative examination of several transport characteristics. Our strategy is based on grafting a spherical NP with prescribed grafting density of Biotin-Polyethylene-glycol-thiol (Biotin-PEG-thiol) molecules and end-linking a controlled fraction of them with a single NLS, see Fig. 1A. It is expected, therefore, that under exposure to cell extract (CE), an NLS peptide will first recruit an α-importin protein, followed by binding of a β-importin protein, which subsequently will recruit dynein. Thus, the PEG, which connects between the dynein and the NP, serves as a spacer polymer with variable flexibility (depending on its contour length, i.e., molecular weight). These spacers allow, by stretching, for motors originating from the NP sides to readily reach the MT surface (Fig. 2A), thereby increasing the number of motors participating in the transport. It follows that the NP characteristics, such as PEG grafting density, linked NLS fraction, PEG contour length, particle size, and CE concentration, all together govern over the number of dynein motors that bind to the MT simultaneously – which brings a great advantage for the use of this model cargo.

Our NPs are quite different from the cargos reported in Refs. (36-38); the latter lack critical characteristics if they are to serve as model native cargos. First, they do not involve the native protein assembly for the recruitment of dynein from the cytoplasm. Second, their size is one order of magnitude larger than typical native cargo size (radius 20-100 nm). Third, the cargos used in Refs (36, 37) lack control of mechanical coupling between motors. As such, they are less suitable for a fundamental experimental and theoretical study (of a model multi-motor cargo) that could lead to a profound understanding of the motion of native cargos.

In this work, we performed bead-motility assays using total internal reflection fluorescence (TIRF) microscopy. Single-particle tracking algorithms were used to extract the NPs' trajectories. We measured different properties of the trajectories: (i) modes of motion, i.e., unidirectional, bidirectional, and hops between crossing MTs, (ii) run lengths, (iii) run times, and (iv) off-axis

steps. On the theoretical side, the NP active transport is modeled by including a few competing processes, such as binding/unbinding to/from the MT surface and the stepping kinetics of individual dynein motor proteins. These are performed on the 2D curved microtubule surface, and are influenced by both the elastic coupling between motors (*via* the spacer polymers) and the excluded-volume interaction between motors. We used Monte-Carlo (MC) simulations to describe these dynamics. We then highlight the unique features of the multi-motor carried NP, based on a close comparison between experiment and theory (simulations), which gives mutual support to one another. Moreover, this comparison provides insight into the mechanism of NP motion, in particular, the role of multiple motor action during transport, and it suggests a possible mechanism for NP obstacle bypassing.

Results

I. Experiment

I.1 NP preparation and analysis

The NP-complex (henceforth, NP) synthesis process entails several consecutive steps, where at each step, a single component is added (Fig. 1A). Bare NPs saturated with NeutrAvidin were conjugated with Biotin-PEG spacers, then incubated for a short time in a solution containing SV40 T large antigen NLS peptide at variable concentrations.

The resulting NPs are being characterized (SI Sec.1) using cryo-transmission electron microscopy (cryo-TEM), dynamic light scattering (DLS), zeta potential (ζ-potential), and ultraviolet-visible (UVVis) adsorption isotherm, yielding the surface density and mean number of grafted Biotin-PEG-thiols (B-PEG-SHs), $\langle N \rangle$, that are end-conjugated by NLS (PEG-NLS) – see Fig. S1.2. The latter can be transformed into a mean *anchoring* distance between neighboring PEG-NLSs ξ^*. The resulting anchoring distance, ξ^*, is depicted in Fig. 1B against [NLS], showing that incubation of NPs in higher [NLS] solutions lead to a shorter distance between adjacent PEG-NLSs until it reaches saturation above [NLS] = 4×10^{-6} M. Note that the theoretical value of the (free polymer) gyration radius is R_g = 2.27 nm (for a PEG Mw = 5 kDa; SI Sec.2).Thus, since NeutrAvidin diameter is about 5nm (47), and since the NeutrAvidins are closely packed on the NP surface, we may conclude that the anchored PEG molecules are effectively in the so-called

"mushroom regime"(48), $\xi^* > R_g$.

Next, NPs are incubated in (Hela) cell extract (CE), allowing the recruitments of α- and β-importins, followed by mammalian dynein association; the recruitments of the importins and dynein are verified *via* Western Blot (Fig. 1C). Fig. 1C(a) shows the WB image after exposure to cell extract, demonstrating antibody specific binding to importin-α2. Fig. 1C(b) shows the WB image demonstrating dynein recruitment. Group 1 (in both (a) and (b)) refers to Hela cells extract without NPs; group 2 refers to NPs coated with B-PEG-SH incubated in Hela cells extract; and group 3 refers to PEG-NLS coated NPs, which were also incubated in Hela cells extract. Note that although importin-β binding was not directly verified, dynein recruitment requires importin-β binding, suggesting that, in the absence of NLS, the dynein machinery is not recruited to the NP surface.

I.2 NP motility assays

Nano particles were washed from the excess cell extract, incubated in an ATP solution, and then were injected into a flow cell in which MTs are adsorbed and immobilized on a glass surface. We investigated the different modes of motion of the NPs, under four different [NLS] and [CE] as defined in Table 1 (henceforth referred to as systems I, II, III, IV) and used total internal reflection fluorescence (TIRF) microscopy to follow the NPs motion. (An additional system with high [CE] was examined. However, it is not shown or discussed here since its motility is strongly reduced presumably due to molecular crowding effects, see SI Sec.4) First, we used marked minus-end MTs to confirm the expected correlation between the MT polarity and the NP motional direction – as dictated by dynein bias to move towards the minus-end (Fig. 3A). Next, a standard particle tracking algorithm was used to extract the NPs center-of-mass position with nm-scale precision (49, 50) (SI Sec.3), resulting in time-dependent individual trajectories. In addition, since only a small fraction of the MTs were minus-end labeled, we have determined the MT polarity by using the NP most frequent motional direction.

To analyze the NP motion, we differentiated the NPs trajectories into retrograde and

anterograde motion, with respect to the movement along the MT long-axis (henceforth 'longitudinal motion'). We have detected four major modes of motion (Fig. 3 and Table 1) : (i) NPs moving continuously towards the MT minus-end (Fig. 3.A-B); (ii) NPs that have reached the MT end after exhibiting continuous anterograde motion – sometimes followed by a short retrograde motion (i.e., towards the MT plus-end) – and then, the NPs have either detached from the MT or remained immobile (Fig. 3.C-D); (iii) NPs performing bidirectional motion (Fig. 3.E-F), such that a single NP trajectory comprises of both anterograde and retrograde long, continuous, paths of comparable length and velocity; and (iv) NPs traversing between crossing MTs (Fig. 3.G-H). Two comments are worthy at this point: First, the trajectories involving shifting between crossing MT tracks (mode (iv) above) are very unlikely to occur if the NP is carried by a single motor. Since such traversing events do occur, it is safe to assume that the NP is carried by more than one motor. Second, the bidirectional trajectories are less than 10% (out of all the trajectories) and occur predominantly in one of the most diluted samples (system III; see Table 1).

We tested the influence of the [NLS] and [CE] on the NPs motion. In Table 1, we summarize the estimated values of the mean inter-anchor distance ξ^* of PEG-NLS for the four systems (deduced from the data presented in Fig. 1B and SI. Sec.1). Note that ξ^* serves as an estimated lower bound for the mean inter-anchoring distance ξ of the PEG-NLS-$\alpha\beta$-dynein ($\alpha\beta$ refers to the α and β importin complex), such that ξ should approach ξ^* (from above) as [CE] increases (ξ has not been measured). Moreover, given the expected sub-mM concentrations of dynein (51), we assume the system is much below the saturation of dynein binding "isotherm," such that increase of [CE] (hence dynein) is likely to increase dynein surface concentration, i.e., decrease of ξ. Thus, systems I- IV, having the same [CE], are expected to have the same value of ξ/ξ^*. Note that the value of ξ^* determines the mean number of PEG-NLS per NP *via* $\langle N\rangle = \frac{4\pi R^2}{\xi^{*2}}$. This implies that $\langle N\rangle$ varies between 5 and 37 for [NLS] varying between 0.025 and 0.3 μM (Table. 1 and SI. Sec.1).

We now focus only on the ensemble of NPs performing the unidirectional motion. The mean properties of their trajectories are shown in Fig. 4 and summarized in SI Sec.4 as per system. Notably, about 90% of their steps are of anterograde ($v_x > 0$) type (see Fig. S4.1 for the distributions of the *temporal absolute* velocity, v, longitudinal velocity, v_x, and transverse velocity, v_y). To further characterize the NP motions – as also shown in Fig. 4 and SI Sec.4 – we have extracted the mean values of the longitudinal velocity (anterograde, $v_x > 0$,and

retrograde, $v_x < 0$) and of the transverse velocity (left, $v_y < 0$, and right, $v_y > 0$). As [NLS] and [CE] increase – implying a decrease of ξ and increase of the number of NP bound motors, $\langle N_m \rangle = \frac{4\pi R^2}{\xi^2}$ – the corresponding absolute and longitudinal velocities decrease. Conversely, the probability of retrograde and anterograde motions do not vary greatly. Notably, in the diluted systems (I, II, and III), the longitudinal anterograde velocity, $\langle v_x \rangle \mid v_x > 0$, is significantly higher – in absolute values – than the retrograde velocity $\langle v_x \rangle \mid v_x < 0$, suggesting that NPs move mostly in the direction of the MT minus-end. Moreover, in these NLS diluted systems, the transverse motion is significantly smaller than the longitudinal velocity. Similar to the above analysis, in SI Sec.5, we summarize the properties of the observed bidirectional motion.

The results demonstrate a decrease of the NP velocities on the (assumed) increase in the mean number of motors participating in the transport, presumably due to inter-motor interactions. Moreover, we have examined the average NP run-time, $\langle \tau_p \rangle$, and run length (along the MT symmetry axis), $\langle \lambda \rangle$, for the different system concentrations (Fig. 4; SI Sec.4). We observe an increase of $\langle \tau_p \rangle$ with increasing system concentrations (decrease of ξ), also consistent with the expected increase number of participating motors. Note, however, that since $\langle \lambda \rangle = \langle v_x \times \tau_p \rangle$, the run length dependence on system concentrations (influencing ξ) is non-monotonous and shows a maximum for system IV.

As discussed above, while most dynein motor studies assume purely longitudinal motion, more recent studies discovered rich transverse dynamics (36, 37, 52, 53). Accordingly, we analyzed the NP trajectories for transverse motion. First, we calculated (SI Sec.3) the estimated transverse motion of the NPs for the different systems (Fig. 4 A, D). To obtain further insight, as shown in Fig. 5 and SI Sec. 6, we map the transverse velocity into an angular velocity, $\omega = \frac{\Delta\phi}{\Delta t}$ (where $\Delta\phi$ is the angular increment of a single time step, Δt), assuming an ideal angular motion with constant orbital radius, $R_{\mathrm{orb}} = 153$ nm (Fig. 6A); the latter is estimated by considering molecular dimensions (SI Sec.3). The angular motion, together with the longitudinal motion, implies that if the MT had been elevated above the surface, the NP would have performed a helical motion around the MT symmetry axis. Assuming that the fluctuations in angular motion are relatively small, we could consider the mean angular velocity as a representative number and estimate the mean pitch size of the assumed helix using $\langle \bar{H} \rangle = 2\pi \langle v_x \rangle / \langle \omega \rangle$ (SI Sec.3) . This leads to the results shown in Fig. 5C and SI Sec.6.

However, using the theoretical model simulations presented in the next section, we demonstrate in S.Movie 1-4 and Fig. 6 selected trajectories of a single NP, showing angular motion "fluctuations" of different magnitudes, such that the NP effectively performs both right- and left-handed helical motion in a single trajectory. We define a helical motion as a single and complete turn ($\phi = 2\pi$) around the MT. Therefore, we now split the angular motion into right- and left-handed motion (Fig. 5 and SI Sec.6). For the most diluted systems, I and II, the resulting mean of the absolute angular velocities shows that indeed the right- and left- handed motions occur at similar angular velocities, which almost cancel each other when we consider the overall mean value, as suspected. The resulting helical pitches for the anticipated right- and left- handed helices (in a hypothetical surface free experiment) are comparable to each other (Fig. 5 and SI Sec.6).

Furthermore, we analyze the correlations between longitudinal direction and angular directions. In Fig. 5B, we present the mean angular velocity for separated anterograde and retrograde motions. The results show pronounced correlations between the longitudinal and angular directions, showing that backward (retrograde) steps – although being relatively rare – are highly correlated with right-handed motion. These strong correlations are diminished as we move from systems I to III, suggesting that the increasing number of NP bound motors is suppressing these correlations, and they are clearly a single motor property. The implications of such extraordinary behavior will be addressed in the Discussion section.

II. Theory

II.1 Theoretical model and simulations

To explain the above experimental results and gain profound knowledge regarding the NP motion and behavior, we constructed a model for the active transport of the NP. Previous work on multi-motor complexes builds on a single motor motion on a 1D microtubule track (31, 32, 35, 41, 54), and as such, cannot describe the motion of the NP around the 2D MT surface. The single motor stepping was recently revisited to describe 2D stepping of a single *yeast* dynein on the microtubule surface; this stepping model correctly accounts for the measured longitudinal step-size distribution and, moreover, predicts a broad angular distribution of steps (of a single motor) with a small right-handed bias (39). More recently, Yildiz *et al.* (37) studied the single *mammalian* dynein stepping kinetics, providing the longitudinal- and transverse- step-size distributions. Using Yildiz *et al.* raw data (55), we adjusted our yeast dynein model (39) to describe single *mammalian* dynein (SI

Sec.7).

Our model entails an NP on which polymers of equal contour length and fixed density – corresponding to a prescribed mean spacing ξ^* – are grafted at random positions. Each free polymer-end is assigned with a dynein motor, such that $\xi = \xi^*$ by definition. Thus, $\xi = \sqrt{4\pi}\,\mathrm{R}/\sqrt{N_m}$, where R is the NP radius and N_m is the number of motors that are anchored to the NP surface. Dynein is assumed to perform binding/unbinding kinetics to/from the MT surface, competing with its stepping kinetics (SI Sec.8). Note that by the term "unbinding" we refer to the full detachment of the motor from the MT. This implies that its two MTBDs get disconnected from the MT, such that the inverse of the single motor unbinding rate defines its processivity time. Likewise, "binding" refers to the attachment of a motor to the MT surface from the bulk solution. The motors motion on the 2D curved microtubule surface is influenced by the elastic coupling between them (*via* the spacer polymers) – a coupling that influences both the motors step vector distribution and the binding-unbinding kinetics. In addition, we account for the excluded-volume interaction between motors that prevents them from stepping over each other. We used Monte-Carlo (MC) simulations to describe the different competing processes, while readjusting the NP center of mass and rotational angle after each MC step to achieve mechanical force balance – processes that are orders of magnitude faster than the binding/unbinding and stepping processes (SI Sec.9).

We note that our model does not include a few experimental setup constraints and boundary conditions. First, it permits free motion of the NP around the MT surface (similar to the bridge-like setup of Yildiz *et al.* (36)), unlike our experimental setup in which the motion might be impaired due to the presence of the impenetrable glass surface. Second, it does not include MT ends (i.e., MTs are considered infinite) and MT junctions (i.e., only isolated MT tracks are considered).

II.2 Theoretical predictions

Results were obtained for various NP configurations, which are characterized by two parameters: R and N_m. For each (R, N_m), we ran the simulations for a few hundreds of (identical) particles to obtain high statistical accuracy. Below we discuss NP of radius R=20 nm and number of motors ranging between N_m=1 to N_m=13. Note that, due to the very rapid motion of the bare NP associated with its small drag coefficient (SI Sec.9), the motor motion should hardly be affected by the

presence of the NP, and in fact, in our model, it is not affected at all. Thus, the ($R = 20$ nm, $N_m = 1$) configuration is used as a representative of the single motor case. The motility characteristics of each NP configuration are described in Figs. 7-10, and in SI Sec.10, using time increment $\Delta t = 0.27$ sec – identical to the experimental one. In SI Sec.11, we complement these with analyses on the timescale of a single MC step (which is 1-2 orders of magnitude smaller). Selected trajectories of single-motor, three-motor, and seven NPs are shown in Fig 6 and S.Movie 1-3, demonstrating rich, fluctuating, helical motions. It is of great interest to unravel how such behavior is influenced by the number of motors. Below we elaborate on these results.

Longitudinal velocity: Fig. 7A shows the mean longitudinal velocity, $\langle v_x \rangle$, against N_m. We find suppression of $\langle v_x \rangle$ from the single motor velocity (833 ± 4 nm/s) as N_m increases. The corresponding standard deviation about the mean also varies with N_m; a maximum appears at $N_m = 4$ (corresponding to $\xi = 35.4$ nm), whereas the minimal standard deviation corresponds to the single motor case. In addition, as seen in Fig. 7B, the characteristic run-time, $\langle \tau_p \rangle$, and longitudinal run-length, $\langle \lambda \rangle$, are also affected by the value of N_m. We observe an effectively monotonous increase of run-time and (longitudinal) run-length with an increase of N_m up to $N_m = 13$.

To better understand the connection between these results and the actual number of motors participating in the motion, we calculated the mean number (per MC unit time) – over all runs – of transient MT-bound motors, $\langle M_B \rangle$ for each (R, N_m) configuration (Fig. 8A). As expected, as N_m increases the value of $\langle M_B \rangle$ increases, yet, surprisingly, it effectively saturates at around $\langle M_B \rangle$ = 2. Furthermore, we extracted the fractions of time for different NP "states"; we *define* an NP state by the number of MT-bound (transporting) motors M_B (Fig. 8C). Note that although $\langle M_B \rangle$ is roughly between one and two, the motor number distributions show that there is some non-negligible contribution of the three- and four- motor states (while five motors and above have negligible contribution). Fig. 8B shows the corresponding mean velocity for each state, avoiding NP temporal velocities associated with transitions between these states *via* binding-unbinding events.

As manifested by the STD shown in Fig. 7A (and by the histograms in Fig. S10.2), the width of the NP longitudinal velocity distribution varies with N_m. We associate this width *both* with the width of the velocity distribution at each motor number state (not shown here) and with the probability distribution of these states (Fig. 8C), which is sensitive to the value of N_m. For $N_m \geq$

2, we unexpectedly observed a second peak around $\upsilon_x = 0$, which becomes more pronounced as N_m increases. This is more strongly demonstrated by the equivalent histograms corresponding to a single MC time-step (SI Sec.11). We associate this new peak to the growing abundance – with increasing N_m – of states $M_B \geq 2$ (Fig. 8C). These states have a greater chance for "jamming configurations," i.e., configurations where the "jamming events" (controlled by excluded-volume interaction, see SI Sec.8) are dominating.

From this analysis, we can conclude that the increase of N_m leads to a non-linear increase of $\langle M_B \rangle$. This increase of $\langle M_B \rangle$ leads, in turn, to longer run-times, $\langle \tau_p \rangle$, and diminishing $\langle \upsilon_x \rangle$, yet the effect on the run-time is more pronounced than on $\langle \upsilon_x \rangle$ such that, in most cases, the resulting run-length, $\langle \lambda \rangle$, is also enhanced. Moreover, the increase of $\langle M_B \rangle$ leads to a slightly narrower NP longitudinal velocity distribution for $N_M > 4$. While an increase of run-time is expected even without the inclusion of motor-motor coupling (16), the decrease of velocity is a sole consequence of the (elastic and excluded volume) motor-motor interactions. Similarly, the *non-trivial* change of width of the υ_x distribution with increasing N_m (see STD in Fig. 7A) reflects the competition between: (i) the increase of the M_B fluctuations (i.e., the corresponding STD, $\langle \delta M_B \rangle$; SI Sec.11), acting to increase the velocity fluctuations, (ii) the variability of the velocity fluctuations within each participating motors state (i.e. $\langle \delta \upsilon_{x,M_B} \rangle$; SI Sec.11), which can be attributed to motor-motor coupling, and (iii) the contributions of the binding\unbinding events.

Angular / Transverse motion: Consider now the angular motion around the MT symmetry axis that leads to a transverse motion on the projected base plane. As can be seen in Fig. 6 and S.Movie 1-4, the motion is composed of apparent both left- and right- handed helices combined with large fluctuations. However, on a very long trajectory, the net helical motion (in which the right- and left- handed helices cancel each other) might appear minor, and will not reflect the true nature of the motion. Therefore, we require here very delicate analyses that will reflect both characteristics.

The variation of the mean angular velocity $\langle \omega \rangle$ and its STD with N_m is shown in Fig. 9A (and SI Sec.11), both demonstrating a monotonous decrease with an increase of N_m. As all values are positive, this suggests a net right-handed helical motion of the NP for all motor numbers. Combined with a variation of the mean longitudinal velocity with N_M (Fig. 7A), and the relation $\langle \bar{H} \rangle = 2\pi \langle \upsilon_x \rangle / \langle \omega \rangle$ describing the mean helical pitch size $\langle \bar{H} \rangle$, this leads to the dependence of variation of $\langle \bar{H} \rangle$ shown in Fig. 10C, exhibiting an increase for growing N_m.

However, as discussed in the experimental section, this pitch size represents the *net* helical

motion, i.e., it includes cancelations of left- and right- handed helices (as seen in Fig. 6 and S.Movie 1-4). To refine the helical motion analyses, we define a helix (be it left- or right- handed) whenever the angular motion completes a full round (i.e., $\phi = \pm 2\pi$). Note that, even within a single full round, the motion consists of large and frequent right- and left- handed fluctuations.

In Fig. 10A, we show the resulting mean pitch size for left- ($\phi = -2\pi$) and right- ($\phi = +2\pi$) handed helices separately, and the mean pitch size regardless of the helix vorticity. Notably, the pitch sizes obtained for all these three definitions are all comparable to each other and are much shorter than those deduced using the mean angular velocity – all increase with increasing N_m. To complement these results, we also present, in SI Sec.11, the mean angular velocity separately for left- and right- handed motion.

Longitudinal and angular/transverse motion are correlated: To gain further insight into the complex motion of the NP, we wish to verify whether the longitudinal and angular motions are correlated. In Fig. 9B, we *dissect* the angular velocity for forward and backward steps associated with MC time-step (i.e., positive and negative longitudinal velocities). As seen, backward steps have a greater (positive) mean angular velocity, with the single motor NP showing the largest value. This implies that when a backward step is being performed, the NP is likely to move to the right. Both angular velocity types, associated with either forward or backward steps, show a decrease with increasing motor number N_m.

Discussion

Quantitative comparison between experiment and theory might be hampered by two issues: (i) the lack of knowledge of the relative NP motor coverage $\theta = \left(\frac{\xi^*}{\xi}\right)^2$, which corresponds to the mean number of NP-bound motors $\langle N_m \rangle = \langle N \rangle \times \theta$, where $\langle N \rangle$ is the mean number of PEG-NLS polymers per NP, and (ii) the expected (wide) binomial distribution of N_m between the different NPs. Regarding the first issue, while we cannot reliably estimate the experimental θ, we can reasonably assume that for a given [NLS], the increase of [CE] implies increase of θ, which allows qualitative comparison between different systems – as discussed below. Regarding the second issue, in SI Sec.12, we have computed – using the binomial distribution – some of the reported motility characteristics for a varying $\langle N_m \rangle$. For the mean longitudinal and transverse velocities calculated on the MC time step scale, this analysis shows a small increase of their values (relative

to the values for a deterministic motor number N_m) especially for small motor numbers; this is due to the contribution from NPs with very few motors ($N_m = 1,2,3$), whose velocities are always larger (Fig. 7A). Yet, the trends we have deduced theoretically for the deterministic number of motors (Figs. 7-10) are not altered. When we move to the experimental time scale (0.27 sec), the difference is almost non-discernable. Moreover, the run-times and run-lengths are even less affected by the N_m fluctuations, probably due to the contributions from NPs with large N_m for which these values are much higher.

Qualitative comparison between experiment and theory shows several similarities regarding the dependence of both longitudinal and angular motion on the number of NP-bound motors. Note again that (in the experiment) we have estimated the number of PEG-NLS (N) for the different [NLS] used for the motility assays. First, as N increases, while keeping [CE] fixed (or in other words, θ fixed) – implying an increase of N_m (or $\langle N_m \rangle$), we observe both theoretically and experimentally decrease of the longitudinal mean velocity (Figs 4A, 7A and SI section 11). As for the angular velocity, ω, while the theoretical values show a decrease of ω with increasing N_m, the estimated experimental values do not follow a clear trend. Regarding the actual values of ω and v_x, we can discern that both their values in the experimental system III match the theoretical values for $N_m = 4$ (or, $\langle N_m \rangle = 4$). This could have been accidental. However, we find further evidence suggesting that the match is not accidental. Since N in system IV is 3.5 times larger than in system III (Table 1) while they both have the same [CE], it follows that in system IV, $\langle N_m \rangle$ should be 3.5 times larger as well, i.e., $\langle N_m \rangle \cong 14$. Comparison of ω and v_x between system IV (experimental) and extrapolated theoretical values (linear fit) for $N_m = 14$ ($\omega = 0.5\ \mathrm{rad/sec}, v_x = 516\mathrm{nm}$) indicates a rough agreement between theory and experiment. As for these four systems run-times and run-lengths, both simulation and experimental values show an increase of their values with increasing N_m (due to increase of $\langle N \rangle$).

Further support of the above match appears in the width of the distributions of v_x as exemplified by the corresponding STD. In the simulations, we observed first an increase of STD, followed by a decrease as N_m increases, with a maximum STD at $N_m = 4$. In the experimental results, the maximum STD corresponds to system III (SI sec.4). Importantly, these two systems are just those found above to match in longitudinal and angular velocities.

Considering systems I and II, the most prominent effect seen in both experimental and theoretical studies is the strong correlation between backward (retrograde) and right-handed

motions (Figs. 5B and 9A). Moreover, both theoretical and experimental studies show diminishing of theses correlation with increasing N_m. Thus, it is clear that these correlations emerge from the single motor property and are somewhat suppressed by the action of multiple motors.

The bidirectional motion remains an *enigma*. It is essentially observed only in system III, which is an intermediate system between one and many NP-bound motors ($N_m \cong 4$ by our analysis). Previous work of Ross and coworkers (56) suggested that a single dynein can move in both directions, whereas other works (6, 19, 20, 23, 57) argue that dynein moves mainly towards the MT-minus end. Our experimental work is unable to elucidate which of the two properties is correct, while our theoretical work is limited in this sense as it is based on an MT minus-end directed dynein trajectories.

Conclusions

In this paper, we reported on a combined experimental and theoretical study of NPs that are carried by a multiple number of mammalian dynein motor-proteins. We focus on the different motility characteristics of these multi-motor NPs in comparison to the known and well-studied case of the single dynein (6, 17-20, 37, 38, 53, 57-60). The multi-motor NPs differ from single motor behavior is several aspects. First, as the number of NP-bound motors (N_m) increases, we observe decrease of the mean longitudinal velocity (υ_x). Second, we observe increase of the run-times (τ_p) and run-lengths (λ). Third, the width of the longitudinal velocity distribution also depends peculiarly on the number of NP-bound motors, showing a maximum width at an intermediate value.

We also found that both single and multi-motor NPs perform an angular (transverse) motion that, together with the longitudinal motion, forms a helical trajectory around the MT symmetry axis. This is consistent with previous findings of Yildiz and coworkers (36, 37) in which large particles were studied (about 500 nm radius) and in which the number of particle-bound motors was not varied. Importantly, here we have demonstrated that the helical motion stems from single motor properties, and is somewhat suppressed (an increase of the helical pitch) as N_m increases.

One of the most peculiar features of the angular motion is its correlation to the direction of the longitudinal motion (i.e., anterograde or retrograde motion along the MT long-axis). We have unambiguously shown that retrograde motional intervals dictate large right-handed motion. Moreover, this characteristic also appears as a single motor property, and it diminishes as more motors are available.

The remarkable agreement between theory and experiment give mutual support to both. This has allowed us to use the simulations to unravel NP motional configurations that cannot be accessed in the experiment. In particular, we have deduced from the simulation the partitioning between the different number of motors that participate in the motion. These results have shown that most of the trajectories involve mainly one or two motors, with the mean value approaching two for large N_m. In this way, the NP manages to maintain considerable longitudinal velocity, resulting in a longer run-length.

Our theoretical results for the NP motility features – supported by the experimental ones – suggest that the NPs are self-regulating nano-machines whose behavior is different from the single motor behavior. The self-regulation of the number of participating motors – regardless of the number of NP-bound motors – at a mean M_B value between 1 and 2 with dominating states $M_B = 1, 2, 3$, suggests that the NP is able to optimize between single motor and multi-motor motility properties. This allows the NP to achieve the following features: (i) longer run-time and run-length, (ii) substantial helical motion, (iii) significant longitudinal velocity, and (iv) retrograde motional intervals strongly correlated with large right-handed motion, especially during the temporal state of a single participating (MT-bound) motor. The latter plausibly implies on a mechanism for obstacle bypassing that was not reported so far. We propose that when the NP encounters an obstacle, a right-handed shift is beneficial to make a detour and bypass it. This behavior is strongly enhanced by alternating to the single motor state ($M_B = 1$).

Hence, we conclude that the NP can be regarded as a model native cargo that achieves maximal transport efficiency by optimally using the viable motors bound to its surface. The ability of the NP to make long trajectories enhances its intracellular active transport towards the nucleus. In addition, by maintaining its helical motion, and in particular making large right-handed steps when stepping backward, we posit that the NP is capable of bypassing obstacles that reside on the MT tracks, or in their vicinity. Indeed, this suggestion (yet, without the mention of the backward-right-handed correlated motion) has already been put forward (36). We plan to further investigate this hypothesis in future work. Furthermore, it remains an open question of whether highly efficient native cargos – such as HIV, Herpes-Simplex, and adenoviruses – also regulate the number of participating motors, as our nano-particle does.

Materials and Methods

Experimental procedure

Materials

Hela cell extracts preparation. Hela cell extracts were prepared according to Fu et al. (61). Briefly, Hela cells were grown in DMEM medium supplemented with 10% of Fetal Bovine Serum (FBS) and 1% of penicillin-streptomycin at 37 °C and 5% CO_2. The cells were detached by Trypsin-EDTA solution, washed with Phosphate Buffered Saline (PBS) (0.01 Phosphate buffer, 0.0027M KCL, 0.137M NaCl, pH7.4), and pelleted for 5 min at RT and 500 g. The cells were then incubated on ice with lysis buffer (12 mM Pipes, 2mM MgCl2, 1 mM EGTA, 0.4% Triton X-100, 10% protease inhibitor cocktail, pH 6.8) for 15 min. Finally, the lysates were cleared by centrifugation at 2,700 g and then at 100,000 g, at 4˚C for 10 min each. The cell extracts are diluted 10x with lysis buffer without Triton and protease inhibitors, and the total protein mass concentration is determined by Bradford assay. Sucrose was added to the extracts (10% in mass), which were then flash-frozen in liquid nitrogen and stored at -80°C. For the motility experiments, the extracts were used within four weeks.
Nuclear Localisation Signal (NLS). The NLS sequence (PKKKRKVED) originates from SV40 T large antigen (62). We use N-terminally bromine (Br-Ac) modified NLS. The bromine group is followed by a GGGG sequence ('raft'). To generate a fluorescently labeled NLS peptide, Tetramethylrhodamine (TAMRA) was covalently attached to the NLS raft. Except for UVVis absorption experiments, all experiments were performed using the non-labeled NLS.

NPs preparation. Green Fluorescent microspheres (Bangs Labs or Invitrogen) were used for NP preparation. The total surface area of the bare NPs was maintained constant through all experiments. NPs preparation starts with their incubation with 10µM Neutravidin (31000, Thermo Fisher) for 20 minutes at 25°C. Excess Neutravidin was separated via dialysis. (Streptavidin-coated NPs (Bang Labs) can replace bare NPs as a starting point for NP preparation). The NPs were then incubated with 1mM Biotin-PEG-thiol-5kDa (PG2-BNTH-5, NANOCS) for 30 min at 25°C. Excess Biotin-PEG-thiol was separated by two cycles of centrifugation (6800 g for 8 min at 25°C). These conditions apply for all centrifugations used for NPs preparation steps. Then, NLS peptides were covalently bound to the NPs via their bromine group, which react with the thiol group on the PEG molecule. The reaction was performed at 25°C for 20 minutes. Excess NLS was separated by two cycles of centrifugation. Finally, the NPs were incubated with Hela cell extracts at 30°C for 20 min, allowing the recruitment of α- and β-importins, and mammalian dynein motors to the surface of the NPs. The NPs were separated from excess cell extracts by centrifugation, washed with BRB80 (80 mM PIPES, 1 mM MgCl2, 1 mM EGTA, pH 6.8) supplemented with 1mM Mg-ATP, and centrifuged again. Finally, the NPs were suspended in 60µL BRB80 supplemented with 1mM Mg-ATP and stored on ice until used. In the motility assay experiments, we used two different batches of cell extracts. An identical cell extract was used in systems I and II, and another extract in systems III, IV, and V. To assure full activity of the motility protein

machinery, the NPs were used within 3h.

Methods

Cryo-electron microscopy (Cryo-TEM). Samples for cryo-TEM were prepared according to a standard procedure (63). Vitrified specimens of the NPs solution were prepared on a copper grid coated with a perforated lacy carbon 300 mesh (Ted Pella Inc.). 2.5μL drop of that solution was applied on the grid and blotted with a filter paper to form a thin liquid film, few tens of nanometers thick. The blotted samples were immediately plunged into liquid ethane at its freezing point (-183°C) using an automatic plunge freezer (Leica, EM GP). The vitrified specimens were then transferred into liquid nitrogen for storage. Samples were analyzed using an FEI Tecnai 12 G2 TEM, at 120kV with a Gatan cryo-holder maintained at -180°C. Images were recorded on a slow scan cooled charge-coupled device CCD camera (Gatan manufacturer, Pleasanton, CA, USA) at low dose conditions, to minimize electron beam radiation damage. Recording is performed using Digital Micrograph software (Gatan).

Dynamics light scattering and ζ-potential experiments. DLS and ζ-potential measurements were used to conclude on the NP hydrodynamic diameter (D_h) and charge at the various decoration steps. For these experiments, we use bare NPs of 0.196 μm in diameter. DLS and ζ-potential measurements were performed on a Malvern NanoZS instrument (ZN-NanoSizer, Malvern, England) operating with a 2 mW HeNe laser at a wavelength of 632.8 nm. The detection angle is 173° and 17° for DLS and ζ-potential measurements, respectively. All measurements were done in a temperature-controlled chamber at 25 °C (± 0.05°C); for the analysis of D_h and ζ-potential, the viscosity is taken to be the same as that of water (0.8872cP). The intensity size (hydrodynamic diameter) distribution was extracted from the intensity auto-correlation function calculated using an ALV/LSE 5003 correlator over a time window of 30 s (10 runs of 3 sec) using the software CONTIN. Each measurement was repeated 3 times. The value of D_h was averaged over 3 independent experiments; error bars indicate the standard deviations for these 3 experiments. For ζ-potential measurements, the solution was transferred to a U-tube cuvette (DTS1070, Malvern, England); the instrument was operated in automatic mode. The electrophoretic mobility of the NPs was measured, from which the ζ-potential value is determined by applying the Henry equation (64). The ζ-potential values were averaged over 3 independent experiments with 30 runs per experiments; error bars indicate the standard deviations for these 3 experiments.

UVVis absorption experiments. UVVis absorption experiments were used to determine the mean number of bound PEG-NLS molecules per NP, ⟨N⟩, and the mean anchoring distance between adjacent PEG-NLS molecules, ξ*. UVVis absorption experiments were carried out using fluorescently labeled NLS (TAMRA-NLS) and bare NPs of 45 nm in diameter. The concentration of TAMRA-NLS was determined using an extinction coefficient of $\varepsilon_{553} = 0.0639 \left[\frac{1}{\mu\text{M cm}}\right]$. The value of ⟨N⟩ (and ξ^*) were averaged over 3 independent experiments; error bars indicate the standard deviations for these 3 experiments.

Western Blot. Western-Blot (WB) was used to confirm the recruitment of importins, and dynein

motors by the PEG-NLS coated NPs. In WB experiments, we use NPs of 0.22µm in diameter, [NLS] = 14.8 µM, and [CE] = 3.4mg/ml. The NPs were prepared as detailed above, then pelleted at 6800g for 10 min at 25°C, resuspended in 1x Laemmli Sample Buffer, and boiled for 5 min to promote detachment of the bound proteins. The proteins were separated by electrophoresis using a 12% agarose gel, transferred to a nitrocellulose membrane. The membrane was incubated for 1h in a blocking buffer of PBST (PBS supplemented with 0.1 v/v% Tween) and 10% (v/w) dry skim milk (Sigma-Aldrich). The membrane was washed 3 times with PBST for 5 min, and then incubated for 1h at 25°C with anti-Dynein (Santa Cruz, sc-13524), anti-Karyoprotein α2 (Santa Cruz, sc-55538), or anti-Karyoprotein β1 antibody (Santa Cruz, sc-137016). The primary antibodies were diluted 1:500 (v/v) in blocking buffer prior use. Then, the membrane was washed 3 times with PBST and incubated with an anti-Mouse HRP conjugated secondary antibody (Santa Cruz, sc-2005) diluted 1:5000 (v/v) in PBST supplemented with 0.5% (v/w) skim milk, for 1h at 25°C. To finalize the procedure, the membrane was washed 3 times with PBST and incubated with an ECL Western blot Reagent (1705060, Bio-Rad), for 5 min in the dark. Images were collected by chemiluminescence using Fusion FX imaging system (Vilber Lourmat, France).

Motility assay experiments

Chamber preparation. Flow cells were prepared using a glass slide and a glass coverslip (washed with deionized water, EtOH 70%, and dried using nitrogen (gas)), and two stripes of warm Parafilm placed in between them, to form a few mm width channel. The chamber was incubated for 5 min with 20 µl (chamber volume) Biotinylated Casein 0.1mg/ml and washed with 3 volumes of BRB80. Biotinylated Casein is prepared by biotinylation of *k*-Casein (Sigma-Aldrich) using EZ-Link (Thermo Fisher, 21336). Then, the chamber was incubated with 20 µl of 1mg/ml Neutravidine (Thermo Fisher, #31000) for 5 min at 23°C, and washed with 3 volumes of BRB80.

Microtubules preparation. Black tubulin from porcine brain, purified via three polymerization/depolymerization cycles (65), was kindly provided by Uri Raviv (Hebrew University). Purified tubulin was flash-frozen in liquid nitrogen and kept at -80˚C until used. Biotin-fluorescently labeled microtubules were prepared according to the protocol described in Christopher Gell et al. work (66). A tubulin mix containing 51µM black tubulin, 6µM Biotin tubulin (T333P, Cytoskeleton), 3µM Rhodamine tubulin (TL590M, Cytoskeleton), and 3mM GMPCPP (NU-405S, Jena Bioscience) was mixed on ice, divided, flash-frozen in liquid nitrogen, and kept at -80°C until used. Prior mix preparation, the black tubulin was thawed and kept on ice for 5 min, then centrifuged for 10 min at 126000g and 4°C. The supernatant was kept on ice, and its concentration was determined by absorbance at 280nm ($\varepsilon_{280} = 115000 \left[\frac{1}{\mathrm{M\ cm}}\right]$). For microtubules (MTs) assembly, an aliquot of the tubulin mix was thawed and diluted with BRB80 to a final concentration of 4µM, then incubated for 3 hours at 37°C to promote MTs assembly. For motility assay experiments, the MTs were diluted to 40nM with warm (37°C) Wash Buffer (WshB) (BRB80 containing 0.02mM Paclitaxel, 15mM Glucose, 0.1mg/ml Glucose oxidase, 0.02mg/ml Catalase, and 50mM DTT) and used on the same day.

Formation of marked-end microtubules. Marked end microtubules were prepared using bright fluorescent MTs seeds that serve as nucleation sites for the polymerization of dim fluorescent, *N*-Ethylmaleimide (NEM) modified tubulin (67, 68). NEM modified tubulin was used to inhibit MT seeds minus-end assembly. NEM modified tubulin was prepared by mixing 100μM black tubulin with 1mM NEM (Sigma-Aldrich) and 0.5mM GMPCPP in BRB80 and placing that solution on ice for 10 min. The reaction was quenched by the addition of 8 mM β-mercaptoethanol. The NEM-tubulin mix was incubated on ice for an additional 10 min.

For marked-end MTs preparation, a tubulin mix containing 3.2μM black tubulin, 4μM Rhodamine tubulin, 0.8μM Biotin tubulin and 1mM GMPCPP in BRB80 was incubated for 15 min at 37°C, to produce short 'bright' MT seeds. One volume of bright MT seeds mixed with seven volumes of a 'dim' tubulin mix containing 3.6μM black tubulin, 0.4μM Rhodamine tubulin, 0.8μM Biotin tubulin, 3.2μM NEM modified tubulin, and 1mM GMPCPP in BRB80, was incubated at 37°C for 1h to promote polymerization. The marked-end MTs were diluted to 40nM with warm (37°C) WshB and used on the same day.

Motility assay experiments. The mean diameter of bare NPs used in the motility assays is 45nm. For the experiments, 40nM of microtubules were introduced in the flow cell and incubated for 10 min at 23°C. The chamber was washed with 3 volumes of WshB to remove unbound microtubules. Prior assay, the NPs were pelleted by centrifugation at 6800 g for 8 min at 4°C, resuspended in 60μL Motility Buffer (BRB80 containing 0.02mM Paclitaxel, 15mM Glucose, 0.1mg/ml Glucose oxidase, 0.02mg/ml Catalase, and 50mM DTT, 0.1% Methyl cellulose 4000cP, and 10mM of Mg-ATP), and incubated on ice for 5 min. Prior insertion in the flow cell, the NPs are brought to 23°C. Samples were excited by total internal reflection illumination at 488 and 568 nm (LAS-AF-6000, Leica Microsystems). Images were captured using an Andor DU-897 EMCCD camera (Oxford Instruments).

Data analysis

Particle tracking and image analysis are detailed in SI.3 section. In short, we use the IDL multi-particle tracking method (49) implemented for MATLAB to automatically detect distinct NP trajectories. Using this method, we extract the 2D center-of-mass coordinates $(X(t), Y(t))$ per time point t of the individual NPs. The NP velocity v was calculated by taking the NP's center-of-mass position at times t and $t + \Delta t$ and dividing it by Δt. The longitudinal velocity was calculated by projecting the NP velocity on the MT long symmetry axis, $v_{\mathrm{x}} = v \cdot \hat{u}_{MT}$, where $\hat{u}_{MT}$ is the MT the unit vector. Positive v_{x} corresponds to anterograde motion. Similarly, the transverse motion, $v_{\mathrm{y}} = v \cdot \hat{n}_{MT}$, was determined by projecting the NP velocity on the MT normal unit vector, $\hat{n}_{MT}$. The corresponding transverse step is given by $\Delta y = v_{\mathrm{y}} \Delta t$. Right-handed transverse motion is defined as positive and left-handed transverse motion as negative (see SI.3). We use the mean value of transverse steps, $\langle \Delta y \rangle$, to extract the mean angular velocity, $\langle \omega \rangle$, and its error, ω_e, as follows:

$\langle\omega\rangle \pm \omega_e = \frac{1}{\Delta t}\arcsin\left(\frac{\langle\Delta y\rangle}{R_{orb}}\right) \pm \frac{1}{\Delta t}\left(\frac{\langle\Delta y\rangle}{R_{orb}} \times \frac{1}{\sqrt{1-\left(\frac{SEM(\Delta y)}{R_{orb}}\right)^2}}\right)$, where $SEM(\Delta y)$ is the standard error of the mean (SEM) value of Δy, and $R_{orb} \cong 153$ nm is the distance from the MT center and the NP center-of-mass (see SI.3). Next, we estimate the mean helical pitch, $\langle\bar{H}\rangle$, and its corresponding error, H_e, as follows:

$\langle\bar{H}\rangle \pm \bar{H}_e = \frac{2\pi}{|\langle\omega\rangle|}|\langle v_x\rangle| \pm \sqrt{\left(\frac{2\pi}{\langle\omega\rangle} \times SEM(v_x)\right)^2 + \left(\frac{2\pi \times \langle v_x\rangle}{\langle\omega\rangle^2} \times \omega_e\right)^2}$, where $SEM(v_x)$ is the SEM value of Δv_x.

Acknowledgments

This research was supported by the Focal Technological Area Program of the Israeli National Nanotechnology Initiative (INNI).

References

1. Hirokawa N (1998) Kinesin and dynein superfamily proteins and the mechanism of organelle transport. *Science* 279(5350):519-526.
2. Vale RD (2003) The molecular motor toolbox for intracellular transport. *Cell* 112(4):467-480.
3. Vaisberg EA, Koonce MP, & McIntosh JR (1993) Cytoplasmic dynein plays a role in mammalian mitotic spindle formation. *The Journal of cell biology* 123(4):849-858.
4. Gerson-Gurwitz A, *et al.* (2011) Directionality of individual kinesin-5 Cin8 motors is modulated by loop 8, ionic strength and microtubule geometry. *The EMBO journal* 30(24):4942-4954.
5. Hirokawa N, Noda Y, Tanaka Y, & Niwa S (2009) Kinesin superfamily motor proteins and intracellular transport. *Nature reviews Molecular cell biology* 10(10):682.
6. Hirose K (2012) *Handbook of dynein* (Pan Stanford).
7. Salman H, *et al.* (2005) Nuclear localization signal peptides induce molecular delivery along microtubules. *Biophysical journal* 89(3):2134-2145.
8. Pilling AD, Horiuchi D, Lively CM, & Saxton WM (2006) Kinesin-1 and Dynein are the primary motors for fast transport of mitochondria in Drosophila motor axons. *Molecular biology of the cell* 17(4):2057-2068.
9. Campbell EM & Hope TJ (2015) HIV-1 capsid: the multifaceted key player in HIV-1 infection. *Nature Reviews Microbiology* 13(8):471.
10. Jayappa KD, Ao Z, & Yao X (2012) The HIV-1 passage from cytoplasm to nucleus: the process involving a complex exchange between the components of HIV-1 and cellular machinery to access nucleus and successful integration. *International journal of biochemistry and molecular biology* 3(1):70.
11. Carnes SK & Aiken C (2019) Host proteins involved in microtubule-dependent HIV-1 intracellular transport and uncoating. *Future Virology* 14(5):361-374.
12. Dharan A & Campbell EM (2018) Role of microtubules and microtubule-associated proteins in HIV-1 infection. *Journal of virology* 92(16):e00085-00018.
13. McDonald D, *et al.* (2002) Visualization of the intracellular behavior of HIV in living cells. *The Journal of cell biology* 159(3):441-452.
14. Scherer J & Vallee RB (2011) Adenovirus recruits dynein by an evolutionary novel mechanism involving direct binding to pH-primed hexon. *Viruses* 3(8):1417-1431.
15. Kelkar SA, Pfister KK, Crystal RG, & Leopold PL (2004) Cytoplasmic dynein mediates adenovirus binding to microtubules. *Journal of virology* 78(18):10122-10132.
16. Cohen O & Granek R (2014) Nucleus-targeted drug delivery: theoretical optimization of nanoparticles decoration for enhanced intracellular active transport. *Nano letters* 14(5):2515-2521.
17. Gennerich A, Carter AP, Reck-Peterson SL, & Vale RD (2007) Force-induced bidirectional stepping of cytoplasmic dynein. *Cell* 131(5):952-965.
18. Can S, Lacey S, Gur M, Carter AP, & Yildiz A (2019) Directionality of dynein is controlled by the angle and length of its stalk. *Nature* 566(7744):407.
19. Qiu W, *et al.* (2012) Dynein achieves processive motion using both stochastic and coordinated stepping. *Nature structural & molecular biology* 19(2):193.
20. Reck-Peterson SL, *et al.* (2006) Single-molecule analysis of dynein processivity and stepping behavior. *Cell* 126(2):335-348.
21. Ori-McKenney KM, Xu J, Gross SP, & Vallee RB (2010) A cytoplasmic dynein tail mutation impairs motor processivity. *Nature cell biology* 12(12):1228.
22. Cianfrocco MA, DeSantis ME, Leschziner AE, & Reck-Peterson SL (2015) Mechanism and regulation of cytoplasmic dynein. *Annual review of cell and developmental biology* 31:83-108.
23. Reck-Peterson SL, Redwine WB, Vale RD, & Carter AP (2018) The cytoplasmic dynein transport machinery and its many cargoes. *Nature Reviews Molecular Cell Biology* 19(6):382-398.
24. Gross SP, Vershinin M, & Shubeita GT (2007) Cargo transport: two motors are sometimes better than one. *Current biology* 17(12):R478-R486.
25. Vershinin M, Carter BC, Razafsky DS, King SJ, & Gross SP (2007) Multiple-motor based transport and its regulation by Tau. *Proceedings of the National Academy of Sciences* 104(1):87-92.
26. Hendricks AG, Holzbaur EL, & Goldman YE (2012) Force measurements on cargoes in living cells reveal collective dynamics of microtubule motors. *Proceedings of the National Academy of Sciences* 109(45):18447-18452.
27. Grotjahn DA, *et al.* (2018) Cryo-electron tomography reveals that dynactin recruits a team of dyneins for processive motility. *Nature structural & molecular biology* 25(3):203-207.
28. Torisawa T, *et al.* (2014) Autoinhibition and cooperative activation mechanisms of cytoplasmic dynein. *Nature cell biology* 16(11):1118-1124.
29. Mesika A, Kiss V, Brumfeld V, Ghosh G, & Reich Z (2005) Enhanced intracellular mobility and nuclear accumulation of DNA plasmids associated with a karyophilic protein. *Human gene therapy* 16(2):200-208.
30. Rossi L, Hohn B, & Tinland B (1996) Integration of complete transferred DNA units is dependent on the activity of virulence E2 protein of Agrobacterium tumefaciens. *Proceedings of the National Academy of Sciences* 93(1):126-130.
31. Peker I & Granek R (2016) Multimotor Driven Cargos: From Single Motor under Load to the Role of Motor–Motor Coupling. *The Journal of Physical Chemistry B* 120(26):6319-6326.
32. Müller MJ, Klumpp S, & Lipowsky R (2008) Tug-of-war as a cooperative mechanism for bidirectional cargo transport by molecular motors. *Proceedings of the National Academy of Sciences* 105(12):4609-4614.
33. Derr ND, *et al.* (2012) Tug-of-war in motor protein ensembles revealed with a programmable DNA origami scaffold. *Science* 338(6107):662-665.
34. Hancock WO (2014) Bidirectional cargo transport: moving beyond tug of war. *Nature reviews Molecular cell biology* 15(9):615.

35. Müller MJ, Klumpp S, & Lipowsky R (2010) Bidirectional transport by molecular motors: enhanced processivity and response to external forces. *Biophysical journal* 98(11):2610-2618.
36. Can S, Dewitt MA, & Yildiz A (2014) Bidirectional helical motility of cytoplasmic dynein around microtubules. *Elife* 3:e03205.
37. Elshenawy MM, *et al.* (2019) Cargo adaptors regulate stepping and force generation of mammalian dynein–dynactin. *Nature chemical biology*:1-9.
38. DeWitt MA, Chang AY, Combs PA, & Yildiz A (2012) Cytoplasmic dynein moves through uncoordinated stepping of the AAA+ ring domains. *Science* 335(6065):221-225.
39. Fayer I & Granek R (2019) Directional stepping model for yeast dynein: Longitudinal-and side-step distributions. *Biophysical journal*.
40. TyleráMcLaughlin R (2016) Collective dynamics of processive cytoskeletal motors. *Soft Matter* 12(1):14-21.
41. Berger F, Keller C, Lipowsky R, & Klumpp S (2013) Elastic coupling effects in cooperative transport by a pair of molecular motors. *Cellular and Molecular Bioengineering* 6(1):48-64.
42. Khataee H & Howard J (2019) Force generated by two kinesin motors depends on the load direction and intermolecular coupling. *Physical review letters* 122(18):188101.
43. Miles CE (2018) A Hop, Switch, and Jump: Stochasticity in Models of Motor-Mediated Intracellular Transport. (The University of Utah).
44. Wang Q & Kolomeisky AB (2019) Theoretical Analysis of Run Length Distributions for Coupled Motor Proteins. *The Journal of Physical Chemistry B*.
45. Guérin T, Prost J, Martin P, & Joanny J-F (2010) Coordination and collective properties of molecular motors: theory. *Current opinion in cell biology* 22(1):14-20.
46. Kolomeisky AB & Fisher ME (2007) Molecular motors: a theorist's perspective. *Annu. Rev. Phys. Chem.* 58:675-695.
47. Rosano C, Arosio P, & Bolognesi M (1999) The X-ray three-dimensional structure of avidin. *Biomolecular Engineering* 16(1-4):5-12.
48. De Gennes P (1988) Model polymers at interfaces. *Physical basis of cell-cell adhesion*, (CRC Press Boca Raton, FL), pp 39-60.
49. Crocker JC & Grier DG (1996) Methods of digital video microscopy for colloidal studies. *Journal of colloid and interface science* 179(1):298-310.
50. Savin T & Doyle PS (2007) Statistical and sampling issues when using multiple particle tracking. *Physical Review E* 76(2):021501.
51. Ananthanarayanan V (1986) Dynein dynamics during meiotic nuclear oscillations of fission yeast. (Harvard Medical School, Boston).
52. Ando J, *et al.* (2020) Small stepping motion of processive dynein revealed by load-free high-speed single-particle tracking. *Scientific Reports* 10(1):1-11.
53. Lippert LG, *et al.* (2017) Angular measurements of the dynein ring reveal a stepping mechanism dependent on a flexible stalk. *Proceedings of the National Academy of Sciences* 114(23):E4564-E4573.
54. Klumpp S, Keller C, Berger F, & Lipowsky R (2015) Molecular motors: Cooperative phenomena of multiple molecular motors. *Multiscale Modeling in Biomechanics and Mechanobiology*, (Springer), pp 27-61.
55. Yildiz A & Canty JT (2019) Private Communication.
56. Ross JL, Wallace K, Shuman H, Goldman YE, & Holzbaur EL (2006) Processive bidirectional motion of dynein–dynactin complexes in vitro. *Nature cell biology* 8(6):562.
57. Li L, Alper J, & Alexov E (2016) Cytoplasmic dynein binding, run length, and velocity are guided by long-range electrostatic interactions. *Scientific reports* 6:31523.
58. Belyy V, *et al.* (2016) The mammalian dynein–dynactin complex is a strong opponent to kinesin in a tug-of-war competition. *Nature cell biology* 18(9):1018.
59. Bameta T, Padinhateeri R, & Inamdar MM (2013) Force generation and step-size fluctuations in a dynein motor. *Journal of Statistical Mechanics: Theory and Experiment* 2013(02):P02030.
60. Roberts AJ, *et al.* (2009) AAA+ Ring and linker swing mechanism in the dynein motor. *Cell* 136(3):485-495.
61. Fu M-m & Holzbaur EL (2013) JIP1 regulates the directionality of APP axonal transport by coordinating kinesin and dynein motors. *Journal of Cell Biology* 202(3):495-508.
62. Kalderon D, Roberts BL, Richardson WD, & Smith AE (1984) A short amino acid sequence able to specify nuclear location. *Cell* 39(3):499-509.
63. Danino D, Bernheim-Groswasser A, & Talmon Y (2001) Digital cryogenic transmission electron microscopy: an advanced tool for direct imaging of complex fluids. *Colloids and Surfaces A: Physicochemical and Engineering Aspects* 183:113-122.
64. Delgado ÁV, González-Caballero F, Hunter R, Koopal L, & Lyklema J (2007) Measurement and interpretation of electrokinetic phenomena. *Journal of colloid and interface science* 309(2):194-224.
65. Shemesh A, Ginsburg A, Levi-Kalisman Y, Ringel I, & Raviv U (2018) Structure, assembly, and disassembly of tubulin single rings. *Biochemistry* 57(43):6153-6165.
66. Gell C, *et al.* (2010) Microtubule dynamics reconstituted in vitro and imaged by single-molecule fluorescence microscopy. *Methods in cell biology*, (Elsevier), Vol 95, pp 221-245.
67. Phelps K & Walker R (2000) NEM tubulin inhibits microtubule minus end assembly by a reversible capping mechanism. *Biochemistry* 39(14):3877-3885.
68. Hyman A (1991) Preparation of marked microtubules for the assay of the polarity of microtubule-based motors by fluorescence. *J Cell Sci* 1991(Supplement 14):125-127.

Figures

Fig. 1

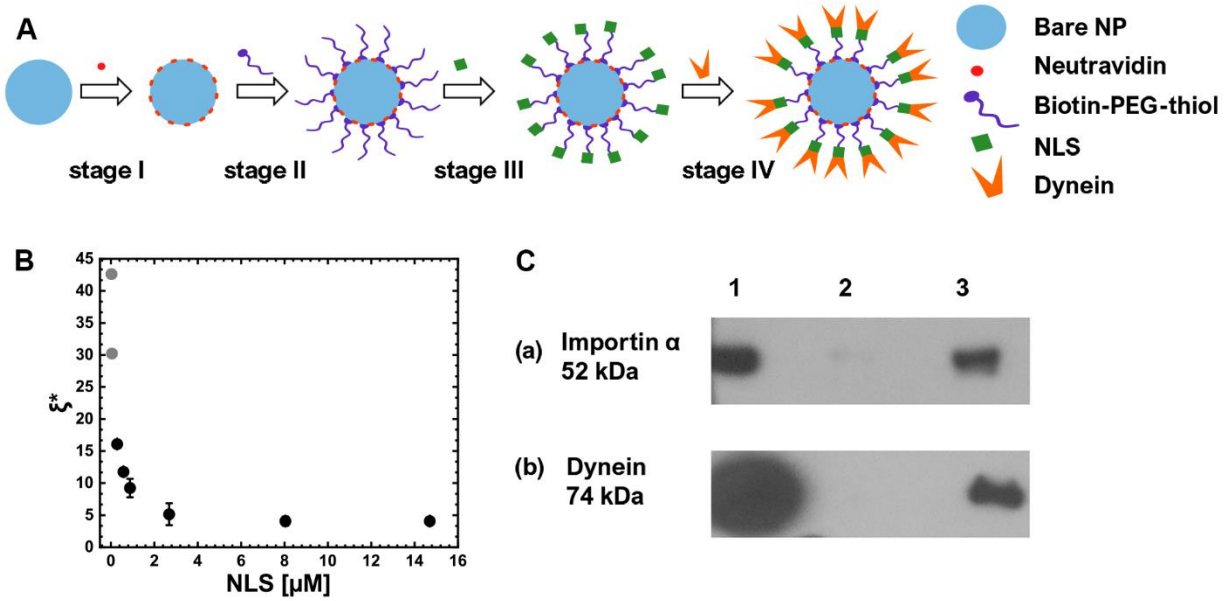

Figure 1. – **NPs synthesis and characterization** (A) NP-complex synthesis process entails several consecutive steps, where at each step, a single component is added. (B) Mean anchoring distance between neighboring PEG-NLSs, ξ^*, against the concentration of NLS. The grey dots correspond to extrapolated values which were calculated from the fit of $\langle N \rangle$ vs. [NLS] (see Table1, SI.1 and Fig. S1.2). Error bars indicate the standard deviations for 3 experiments. (C) Western blot (WB) analysis results demonstrating the recruitment of importin-α2 (a) and mammalian Dynein motors (b) to the NPs after incubation in Hela cells extract. Group 1 (in both (a) and (b)) refers to Hela cells extract without NPs, group 2 refers to NPs coated with Biotin-PEG-SH, and group 3 refers to PEG-NLS coated NPs. The concentration of cells extract used in WB is 3.4 mg/ml.

Fig. 2

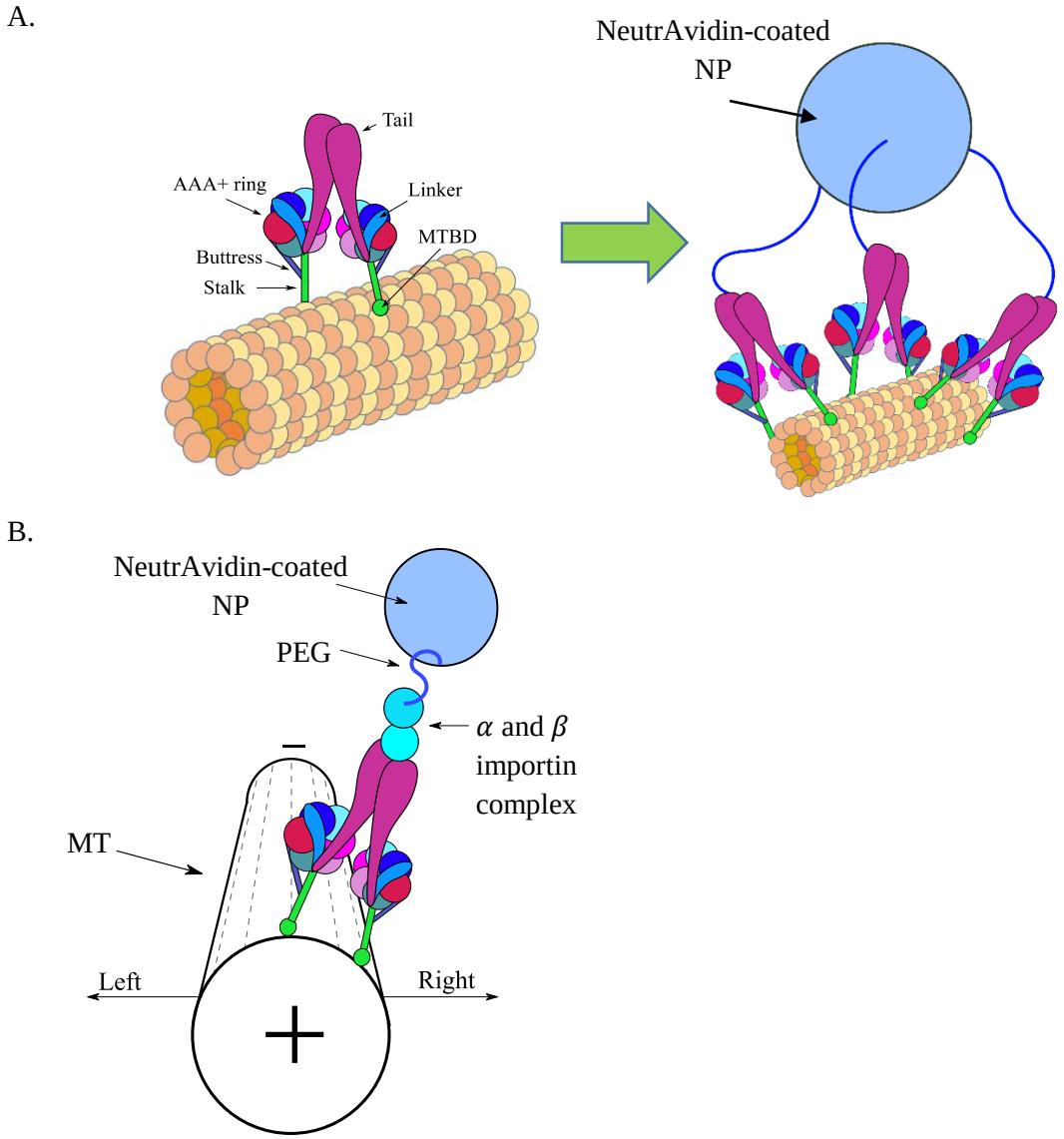

Figure 2 – **Illustration of single dynein and multi-motor NP (not to scale). Some biological factors, such as dynactin and adaptors, are not shown even though necessary for the motor activity. (A)** *Left* – Single dynein motor-protein bound to the MT surface. The MT protofilaments and the corresponding α and β tubulin subunits are represented by the collection of orange and yellow spheres. *Right* – A simplified illustration of an NP having three anchored PEG polymers over its surface, each of which connected to a single dynein. The NeutrAvidin-coated NP is represented by the light-blue sphere, and the PEG polymers are represented by the curved blue lines. **(B)** Illustration of the spatial orientation, which is used throughout the article, and of the NP, including the α and β importin complex. Here, the MT is represented with fewer details, where the dashed lines represent the MT protofilaments.

Table 1

System		I	II	III	IV
NLS conc. [μM]		0.025	0.05	0.05	0.3
CE conc. [μM]		3.4	3.4	3.4	3.4
$\langle N \rangle$		5.2	10.4	10.4	36.6
ξ* [nm]		42.6	30.2	30.2	16.1
Motion mode		Fraction			
		I	II	III	IV
1.	**Unidirectional motion**	1	1	0.91	0.96
1.1	Pure anterograde motion	0	0	0.67	0.65
1.2	Anterograde motion + stuck at the end	0.11	0.24	0.09	0.19
1.3	Anterograde motion + some retrograde motion	0.87	0.52	0.09	0
1.4	MT track crossing	0.02	0.24	0.06	0.12
2.	**Bidirectional motion**	0	0	0.09	0.04

Table 1 – **Summary of the systems studied and their basic properties:** NLS and CE concentrations, estimated mean number $\langle N \rangle$ of PEG-NLS per NP, estimated anchoring distance (ξ^*), and fractions of the different modes of motion. An identical cell extract was used in systems III and IV, and another extract was used in systems I and II. The NPs mean diameter is 45 nm.

Fig. 3

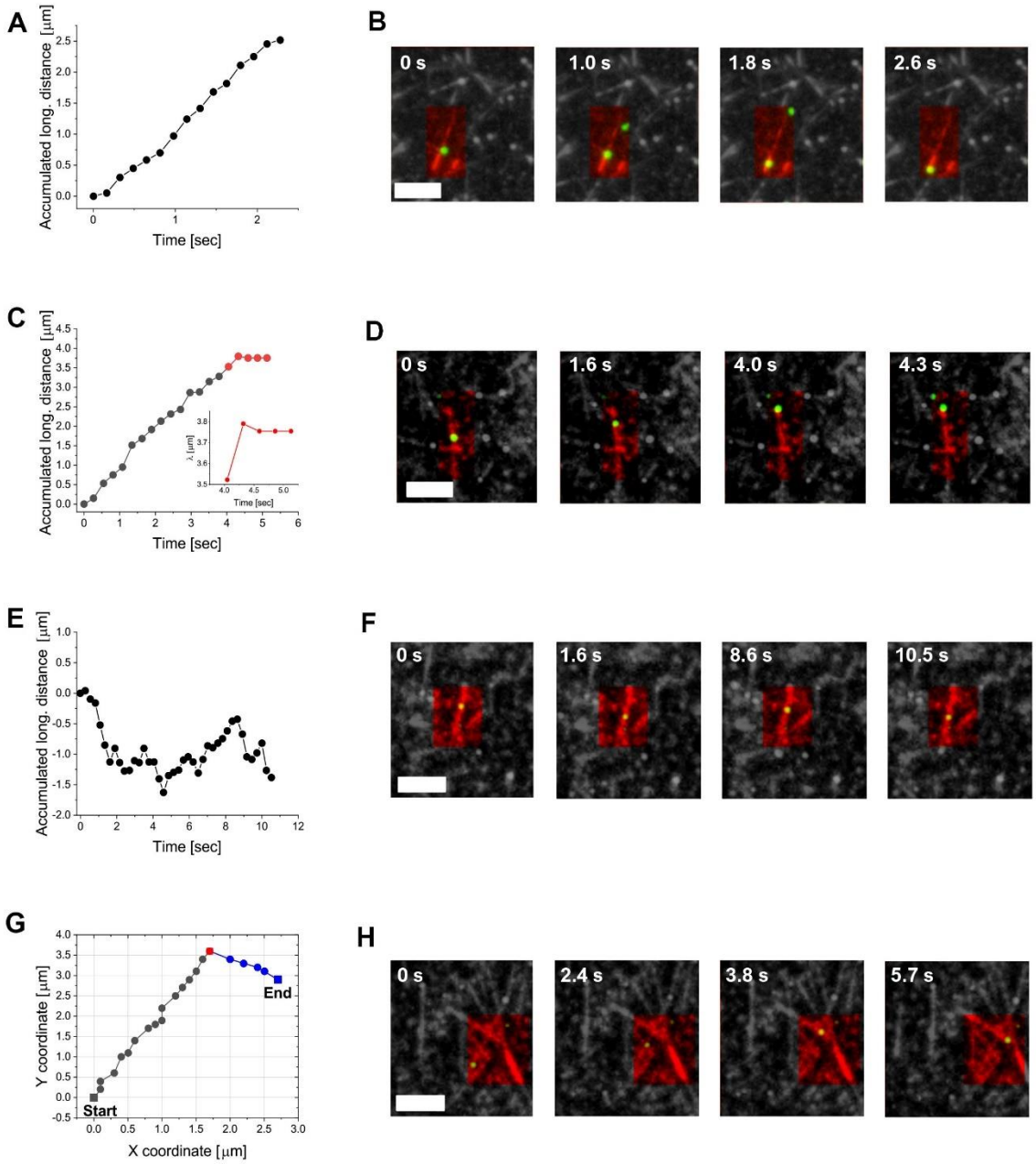

Figure 3 – **Examples of NPs motion modes.** Three first rows show the accumulated longitudinal distance of an NP and the corresponding snapshots for different motion modes. **(A-B)** Anterograde motion of an NP moving towards the MT minus-end (marked-end MTs are shown). **(C-D)** Anterograde motion with a retrograde step at the end of the NP trajectory. The NP remains stagnant for some time before detaching. **(E-F)** Bidirectional motion of an NP. **(G-H)** Trajectory of an NP hopping between crossing MT tracks. The MT tracks are colored in red, and the NPs in green (the NPs mean diameter is 45 nm, Scale bars are 50 nm). The concentrations of NLS is 0.05µM, and that of cells extract is 3.4 mg/ml. The time interval between frames is 0.27s.

Fig. 4

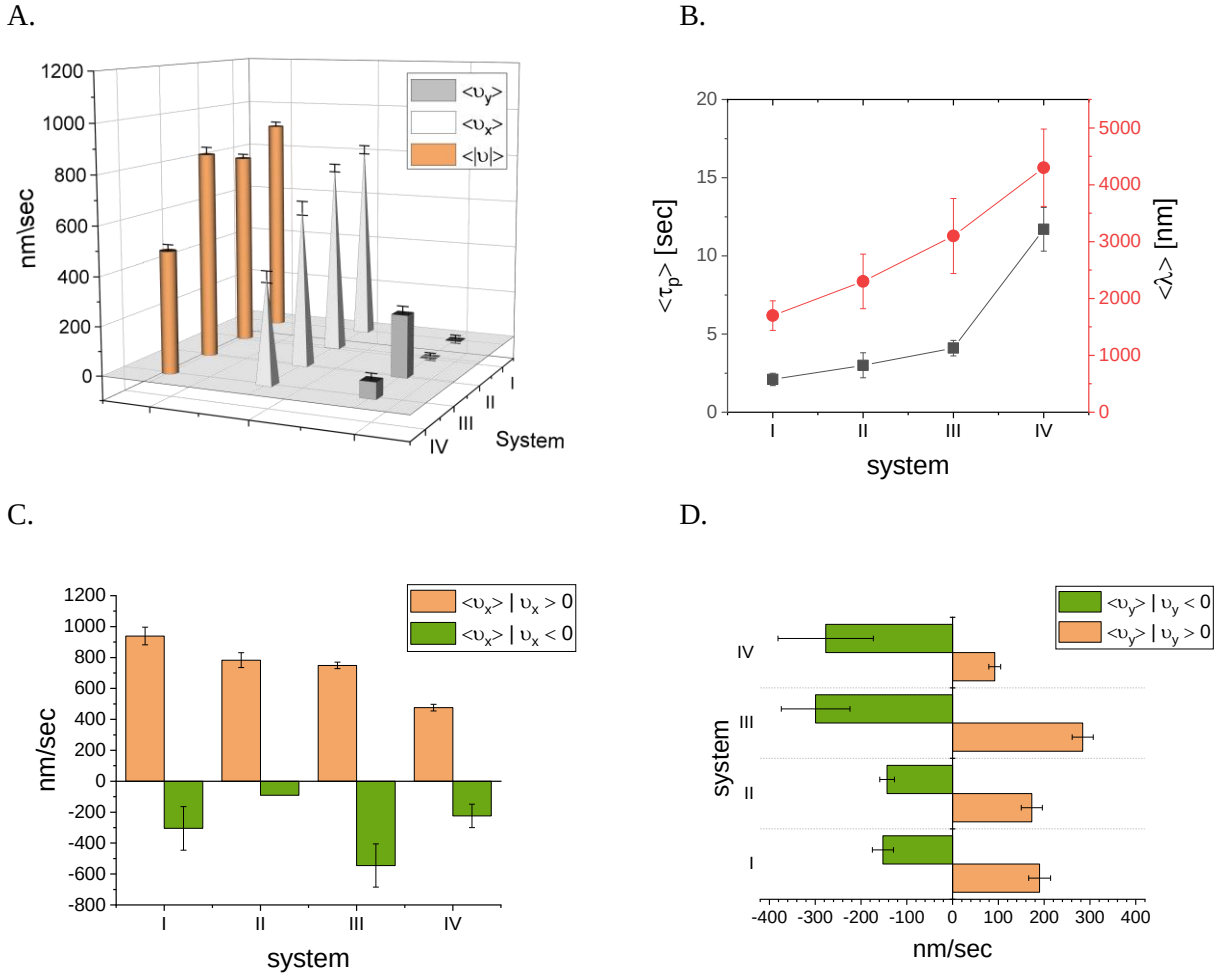

Figure 4 – **NPs experimental mean velocities, run-times, and run-lengths for systems I to IV. (A)** Mean longitudinal, $\langle v_x \rangle$, transverse, $\langle v_y \rangle$, and magnitude (absolute vector value), $\langle v \rangle = \langle \sqrt{(v_x^2 + v_y^2)} \rangle$, velocities. A minus-end directed (anterograde) motion corresponds to $v_x > 0$, and a right-handed motion corresponds to $v_y > 0$ (see Fig. 1C for spatial orientation). **(B)** Run-times and run-lengths; the run-time is measured from the time the NP binds to the MT until the time it unbinds from it; the run-length is the accumulated distance traveled along the MT symmetry axis; $v_x > 0$ defines anterograde motion, and $v_x < 0$ defines retrograde motion. **(C)** Mean longitudinal velocity evaluated separately for anterograde and retrograde motions. **(D)** Mean transverse velocity evaluated separately for right-handed and left-handed motions. The NPs mean diameter is 45 nm.

Fig. 5

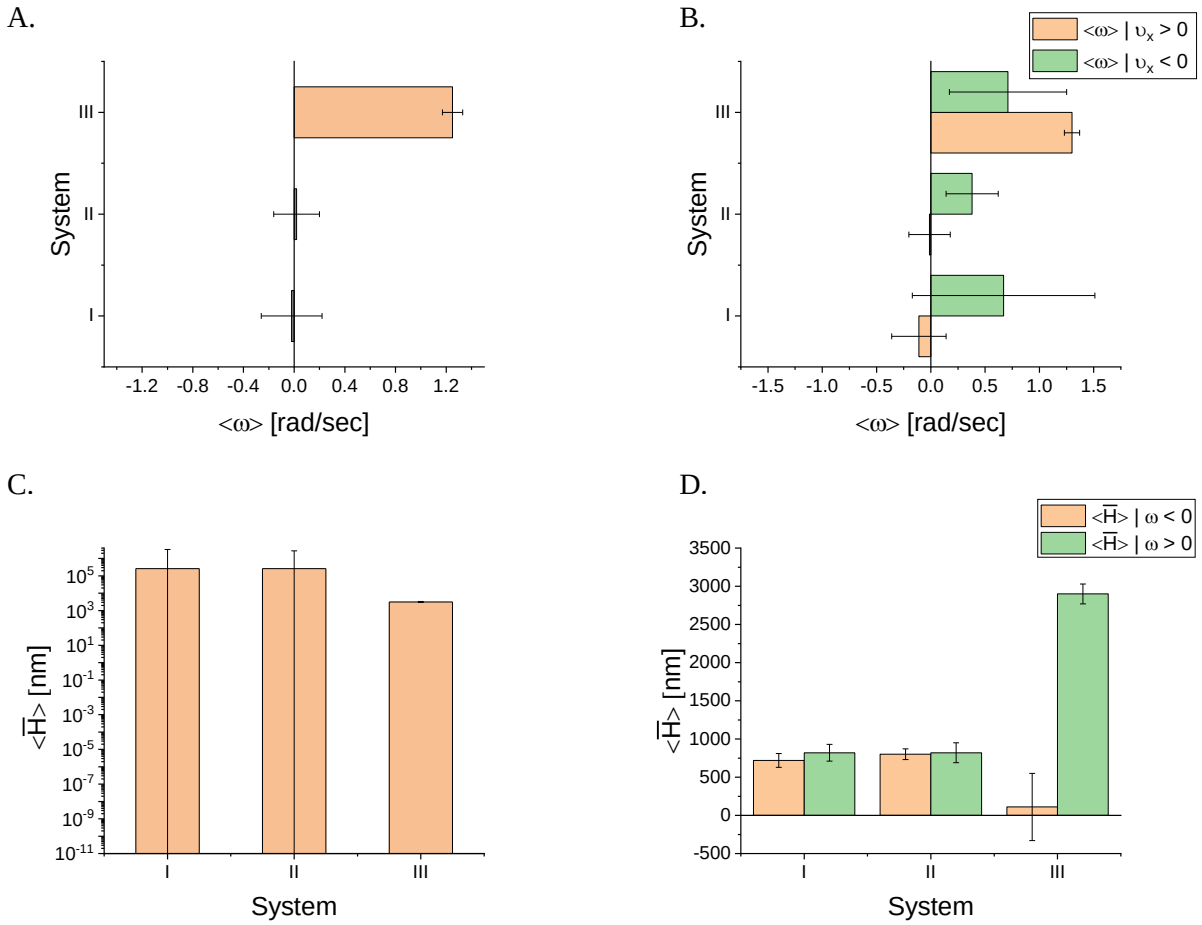

Figure. 5 – **Angular velocity, $\boldsymbol{\omega}$, and estimated helical pitch size, $\langle \bar{H} \rangle$, for systems I, II, and III**. **(A)** Mean angular velocity, $\langle \omega \rangle$. **(B)** Mean conditional angular velocity evaluated separately for anterograde ($v_x > 0$) and retrograde ($v_x < 0$) longitudinal motions. **(C)** Estimated helical pitch size, $\langle \bar{H} \rangle = \frac{2\pi}{|\langle \omega \rangle|} |\langle v_x \rangle|$ **(D)** Estimated conditional helical pitch size, $\langle \bar{H} \rangle$, evaluated separately for right-handed ($\omega > 0$) and left-handed ($\omega < 0$) angular motions. The NPs mean diameter is 45 nm. For further details see SI 3

Fig. 6

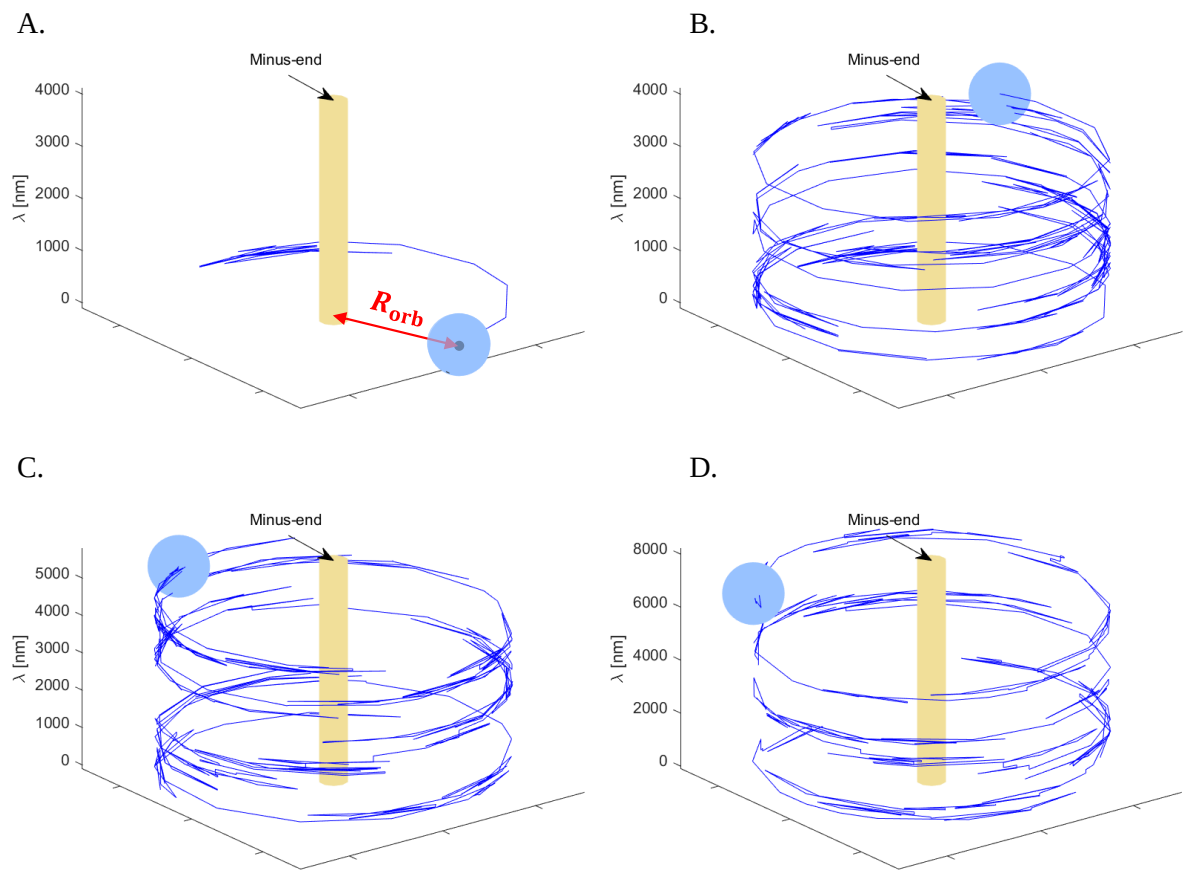

Figure. 6 – **Traces of selected simulated trajectories.** The light-blue sphere represents the NP (R=20 nm); the blue trailing lines represent the trajectory, and the yellow cylinder in the middle represents the MT. Note that while the MT and NP radii are drawn to scale, the MT length is not. **(A)** Initial trace of a single motor trajectory. The red arrow marks the distance between the MT and NP centers, R_{orb}. **(B-D)** Traces of selected trajectories of an NP having $N_m = 1, 3, 13$ motors, respectively (corresponding to S.Movie 1,2 and 4).

Fig. 7

A.

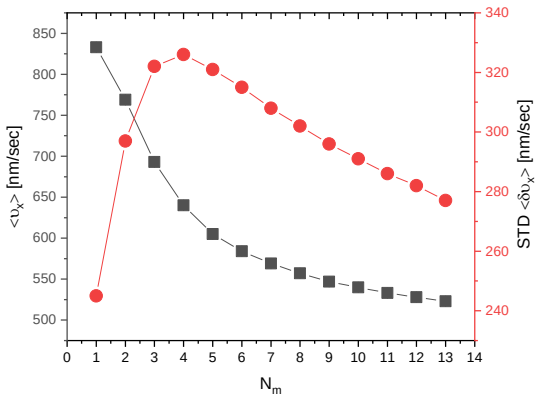

B.

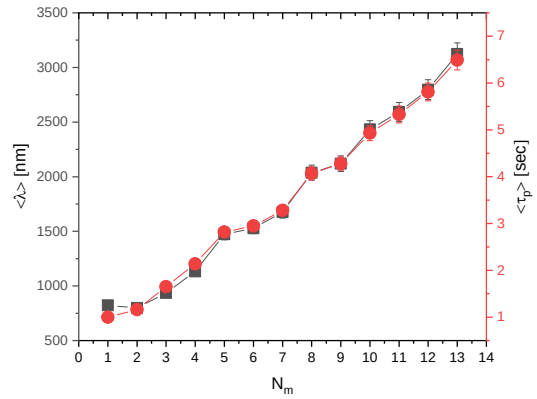

Figure. 7 – **Simulation results for the longitudinal velocity, $\langle v_x \rangle$, run-length, $\langle \lambda \rangle$, and run-time, $\langle \tau_p \rangle$ for NPs of size $R = 20$ against the number of NP-bound motors N_m. (A)** Mean longitudinal velocity and STD for time interval $\Delta t = 0.27\ sec$. **(B)** Run-length and run-time.

Fig. 8

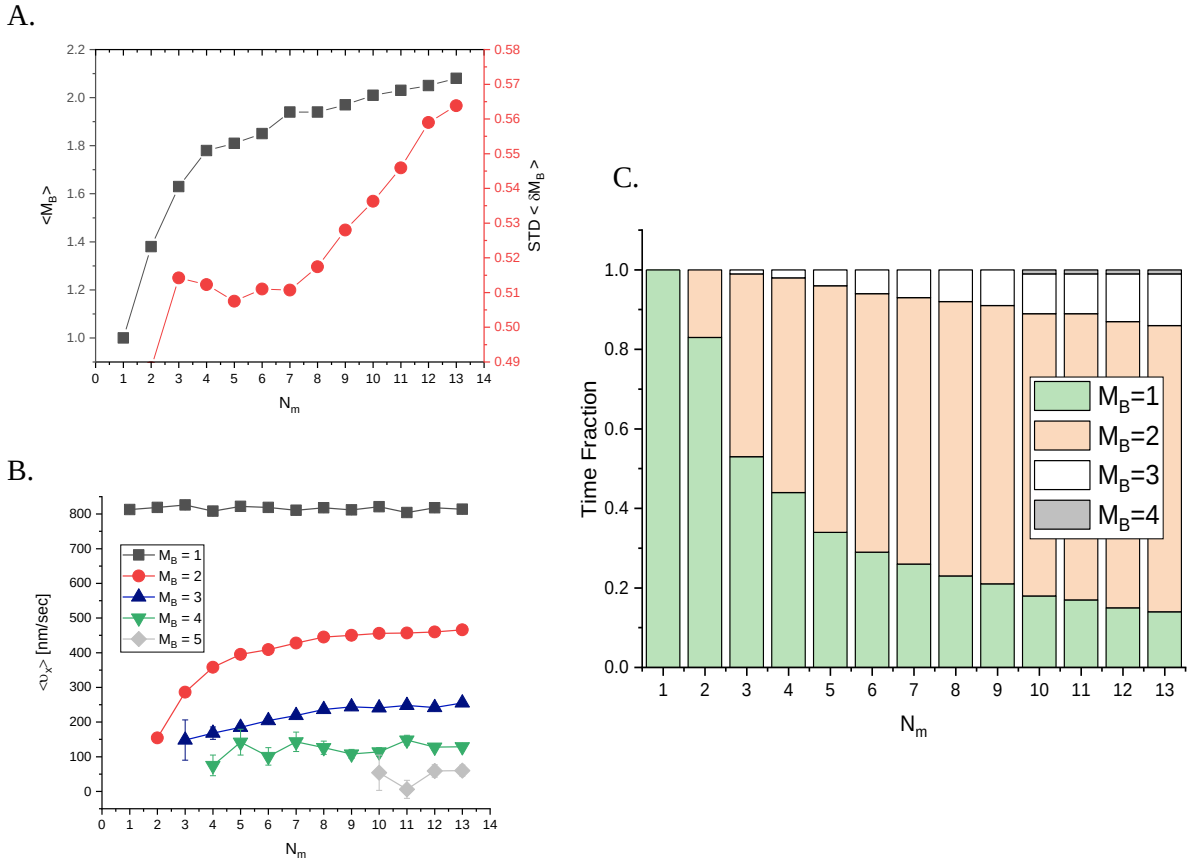

Figure. 8 – **Transiently participating (MT-bound) motors from simulations, $R = 20$ nm, for time interval Δt = MC-step time. (A)** Mean number of participating motors $\langle M_B \rangle$ against the number NP-bound motors N_m. **(B)** Mean velocities of the different M_B-states for different values of N_m. **(C)** Fraction of time the NPs spend in each of the M_B-states, for different values of N_m. Note that states of $M_B \geq 5$ are extremely rare for $N_m \leq 13$; therefore in (B) the state $M_B = 5$ appears only for $N_m \geq 10$, and is not shown at all in (C).

Fig. 9

A. B.

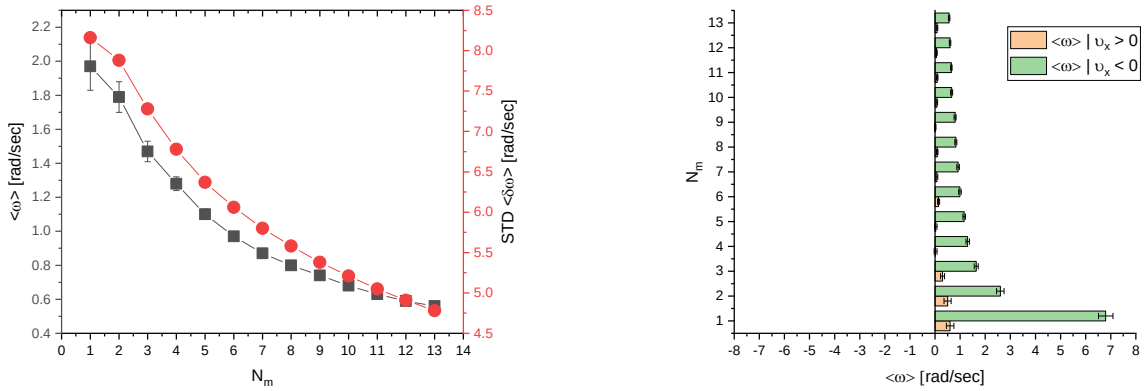

Figure. 9 – **Angular velocity, ω, for different number of NP-bound motors N_m (from simulations) , $R = 20$ nm. (A)** Mean angular velocity, $\langle\omega\rangle$, and the corresponding STD, against N_m, for time interval $\Delta t = 0.27\ sec$ (the values of the mean velocities are presented in Table S10.3) **(B)** Mean conditional angular velocity calculated separately for anterograde motion, $\langle\omega\rangle \mid \upsilon_x > 0$, (orange bars) and retrograde motion, $\langle\omega\rangle \mid \upsilon_x < 0$, (green bars), against the number of NP-bound motors N_m, for the time interval $\Delta t =$ MC-step time.

Fig. 10

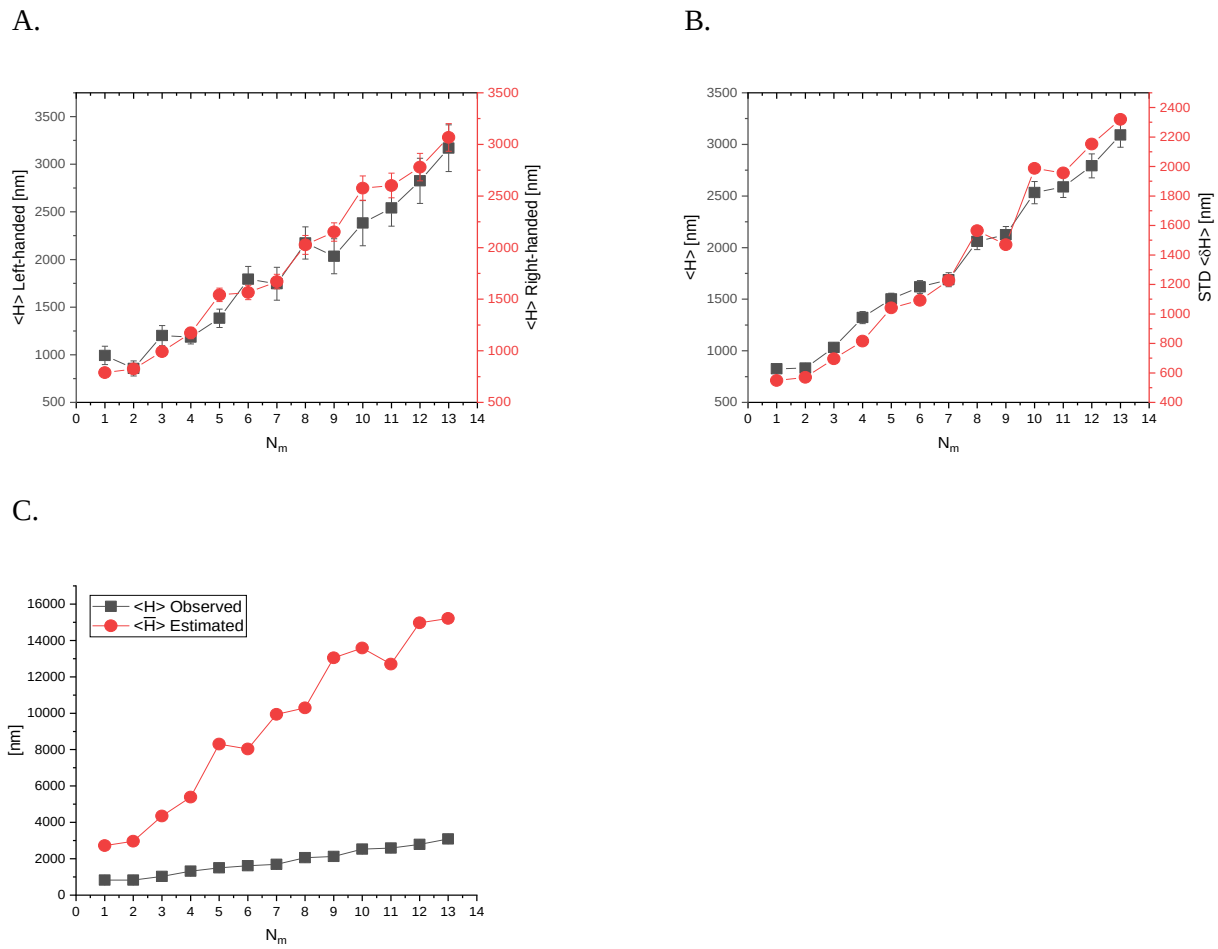

Figure. 10 – **Analysis of the actual NP helical motion from observed trajectories.** (A) Mean helical pitch size, $\langle H \rangle$, evaluated separately for left- and right- handed helical vorticity. (B) Mean and STD of the helical pitch size, regardless of the helical vorticity. (C) Comparison between the actual helical pitch size (from the observed simulated trajectories) and the helical pitch size estimated using the mean values of angular and longitudinal velocities, $\langle \bar{H} \rangle = \frac{2\pi}{|\langle \omega \rangle|} \left| \langle \upsilon_x \rangle \right|$.

PNAS
www.pnas.org

Supplementary Information for

Nano-particles carried by multiple dynein motors: A Self-Regulating Nano-Machine

Fayer, I.[a] & Halbi, G.[b], Aranovich, D.[b], Gat, S.[b], Bar, S.[b], Erukhimovitch, V.[b], Rony Granek[a,c,*], Anne Bernheim-Groswasser[b,c,*]

[a] The Stella and Avram Goren-Goldstein Department of Biotechnology Engineering, Ben-Gurion University of the Negev, Beer Sheva 84105, Israel.

[b] The Department of Chemical Engineering, Ben-Gurion University of the Negev, Beer Sheva 84105, Israel.

[c] The Ilse Katz Institute for Meso and Nanoscale Science and Technology, Ben-Gurion University of the Negev, Beer Sheva 84105, Israel.

* Corresponding authors: Rony Granek & Anne Bernheim-Groswasser

E-mails: rgranek@bgu.ac.il, bernheim@bgu.ac.il

This PDF file includes:

Supplementary text

Figures S1.1 to S12.2

Tables S4.1 to S11.15

SI References

SI. 1 NP Creation and Characterization

The NP synthesis process entails several consecutive steps, where at each step, a single component is added (see Fig. 1A, main text). Bare NPs saturated with NeutrAvidin were conjugated with Biotin-PEG spacers, then incubated for a short time in a solution containing SV40 T large antigen NLS peptides at variable concentrations; see Materials and Methods section. The resulting NPs were characterized using Cryo-TEM, dynamic light scattering (DLS), and zeta potential. In addition, adsorption isotherms from UVVis experiments yield the surface density and the mean number of grafted Biotin-PEG-SHs that are end-conjugated by NLS (PEG-NLS), $\langle N \rangle$. The latter is transformed into a mean anchoring distance between neighboring PEG-NLSs, ξ^* (Fig. 1B, main text). Next, the NPs were incubated in (Hela) cell extract, allowing the recruitments of α- and β-importins, followed by mammalian dynein association; the recruitment of the importins and dynein is verified *via* Western Blot (Fig. 1C, main text). The particles are washed from the excess cell extract, incubated in an ATP solution, and then injected into a flow cell in which MTs are adsorbed and immobilized on a glass surface.

Several measurements were carried out to verify the NPs integrity and to study the various components effect on the NP characteristics, i.e., the complete integration of the -NP and the different components. First, to study the effect of the grafted Biotin-PEG-SH, we examined the distances between adjacent NPs using Cryo-TEM (1). We compared cryo-TEM microscopy images of a control group without grafted PEGs (Fig. S1.1A) and NPs with grafted PEG molecules (Fig. S1.1B). The images show an NPs in which inter-particle distances depend on the absence or presence of grafted PEG molecules. Without PEG, the mean spacing between the NPs is 10.5 ± 7 nm (mean $\pm$ STD), typically twice the diameter of a NeutrAvidin molecule (2), and with an Mw $=$ 5kDa PEG, it is 26 ± 5 nm (mean $\pm$ STD), which is much larger than the theoretical value of the (free polymer) gyration radius: R_g = 2.27 nm (see SI.2 below). This is consistent with weak attractive entropic forces (e.g., depletion attraction) working against the entropic repulsion resulting from the anchored chains (3). Note that the black dots on the particle's surface are the NeutrAvidin molecules (Fig. S1.1). Since NeutrAvidin diameter is about 5nm (2), and since the NeutrAvidins are closely packed on the NP surface, we conclude that the anchored PEG molecules are effectively in the so-called "mushroom regime" (4).

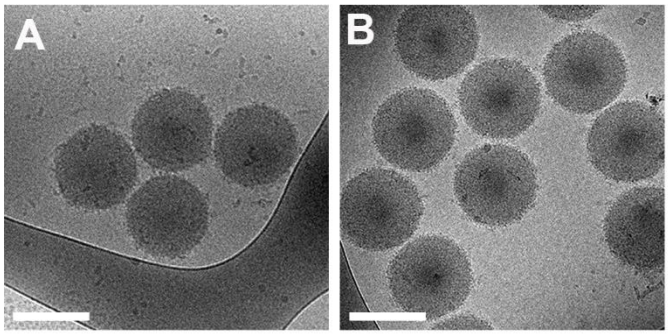

Fig. S1.1 – Cryo-TEM microscopy images of NeutrAvidin-coated NPs without (A) and with (B) grafted PEG (5kDa). Mean bare NPs diameters is 196nm. Bars are 200nm.

To follow the NP decoration during the various stages, we performed dynamic light scattering (DLS) experiments. The data show a significant increase in the NP hydrodynamic diameter (D_h) during the first two decoration steps: 245 ± 10 nm (Stage I) and 410 ± 4 nm (Stage II) compared to the bare NPs, which have $D_h = 198 \pm 3$ nm (all values correspond to $\text{mean} \pm \text{STD}$). At the third step (NLS binding), a slight decrease is detected, confirming the Biotin-PEG-SH binding to the NP.

Next, to conclude on the NP charge at the various decoration steps, we examined the zeta potential (5) (see Materials and Methods section). The zeta potential is highly negative for the bare NPs and has a value of -41.4 ± 1 mV ($\text{mean} \pm \text{STD}$) (i.e., the bare NPs are negatively charged), and it remains negative, but gradually decays (in absolute values) as NP decoration advances. Regarding stages I and III, this trend is consistent with the assumption that both the NeutrAvidin and NLS are positively charged; thus, a reduction of the (absolute value of) the zeta potential is expected after their binding. At the end of stage III (NLS binding), the zeta potential equals -9.6 ± 0.5 mV ($\text{mean} \pm \text{STD}$).

Finally, to determine the mean number of bound PEG-NLS molecules per NP, $\langle N \rangle$, and the mean anchoring distance between adjacent PEG-NLS molecules, ξ^*, we carried out UVVis absorption experiments using fluorescently labeled NLS, TAMRA-NLS (see Materials and Methods section). We incubated PEG-grafted NPs (bare NPs have a mean diameter of 45nm) with increasing amounts of TAMRA-NLS and measured the adsorption of the remaining TAMRA-NLS molecules that *did not* absorb to the NPs (i.e., supernatant). From the absorbance, we deduced the number of TAMRA-NLS molecules that *did* absorb to the NPs,

$$\sum N = 6.02 \cdot 10^{23} \times V \times \left([NLS] - [NLS]_{\text{supernatant}}\right)$$

from which we can deduce the mean number of bound PEG-NLS molecules per NP:

$$\langle \mathrm{N} \rangle = \frac{\sum N}{N_{NP}} \qquad \text{(eq. 1.1)}$$

Where V is solution volume, $[NLS]$ is the concentration of TAMRA-NLS in the incubation solution, $[NLS]_{\text{supernatant}}$ is the concentration of TAMRA-NLS that remained in the bulk and did not absorb to the NPs, $6.02 \cdot 10^{23}$ is the Avogadro number, $\sum N$ is the total number of TAMRA-NLS molecules that were absorbed to the NPs surface, N_{NP} is the total number of NPs - the bare NPs diameter is 45nm.

The dependence of ⟨N⟩ on the concentration of TAMRA-NLS (NLS in Fig. S1.2) follows a Langmuir-like isotherm. We used the parameters extracted from the fit to estimate the mean number of bound motors per NP for $[NLS]$ of 0.05 and 0.025 μM, which are below the detection limit of our UVVis set-up (grey dot in Fig. S1.2). Our motility assays are performed with $[NLS]$ varying between 0.025 and 0.3 μM, implying that $\langle N \rangle$ varies between 5 and 37.

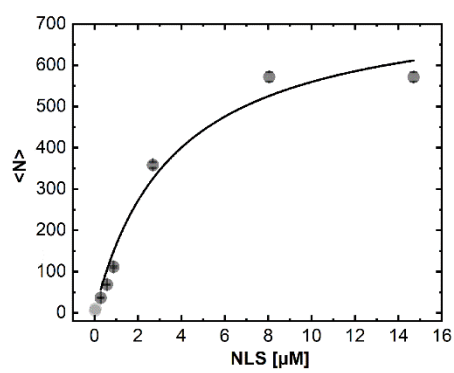

Fig. S1.2 – The dependence of ⟨N⟩ against the concentration of TAMRA-NLS follows a Langmuir-like isotherm (line - fit to the experimental data; $R^2 = 0.96$). The bright grey dots correspond to extrapolated values of ⟨N⟩ calculated using the fit, for $[NLS]$ of 0.025 and 0.05 μM. Error bars indicate the standard deviations for 3 experiments.

Finally, we deduce the mean anchoring distance between adjacent PEG-NLS molecules, ξ^*, from $\langle N \rangle$ assuming that each PEG-NLS molecule occupies a square lattice ξ^{*2},

$$\xi^* = \sqrt{\frac{4\pi R^2}{\langle N \rangle}} \qquad \text{(eq. 1.2)}$$

where $R = 27.5nm$ is the mean radius of NeutrAvidin-coated NPs. The bare NP radius is $22.5nm$. The dependence of ξ^* on [NLS] is depicted in Figure 1B in the main text.

As a final step, we used Western-Blot (WB) to confirm the recruitment of importins and dyneins by the PEG-NLS coated NPs (see Fig. 1C, main text). These results confirm that in the absence of NLS, the dynein machinery is not recruited to the NP surface.

SI. 2 Estimation of the PEG Radius of Gyration, R_g

In our motility experiments, we use biotin polyethylene glycol thiol (Biotin-PEG-SH) with a molecular weight of 5kDa. The molar mass of each ethylene glycol subunit, the building block of the PEG polymer spacer (marked by the red rectangle, Fig. S1.2), is 44.05 g/mol. The number of repeating ethylene glycol subunits, *n*, for a 5kDa PEG, is $n = \frac{5000}{44} = 114$.

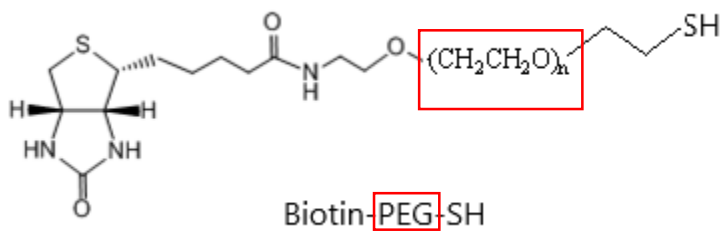

Fig. S1.2 – Molecular structure of the biotin polyethylene glycol thiol (Biotin-PEG-SH) being used. n refers to the number of ethylene glycol units per PEG polymer.

To estimate the radius of gyration, R_g, of the Biotin-PEG-SH, we use the length of an ethylene glycol subunit d_{EG} (6) and the number of ethylene glycol subunits, *n*, as follows (7-9):

$$C_L = d_{EG} \times n \qquad \text{(eq. 2.1)}$$

$$C_L = N_a \times a = d_{EG} \times n \qquad \text{(eq. 2.2)}$$

$$N_a = \frac{d_{EG} \times n}{a} \qquad \text{(eq. 2.3)}$$

$$R_0 = \sqrt{N_a} a \qquad \text{(eq. 2.4)}$$

$$R_g \cong \frac{R_0}{\sqrt{6}} = \frac{\sqrt{N_a} a}{\sqrt{6}} = \frac{\sqrt{d_{EG} \times n \times a}}{\sqrt{6}} \qquad \text{(eq. 2.5)}$$

Where R_g is the polymer gyration radius, R_0 is the polymer end-to-end distance (assuming that PEG polymer behaves like a Gaussian chain (10, 11)), $a = 0.76\text{nm}$ is the PEG Kuhn length (10, 12), N_a is the number of Kuhn length segments, $d_{EG} = 0.358\text{nm}$ (6, 10), and C_L is the PEG polymer contour length.

SI. 3 Particle tracking algorithm for NP motion quantification

We use the IDL multi-particle tracking method (13) implemented for MATLAB to automatically detect distinct NP trajectories. Using this method, we extract the 2D center-of-mass coordinates $(X(t), Y(t))$ per time point t (frame) of the individual NPs, from which we determine the individual NP trajectory over time/frame, $NP(X,Y)_t$. We carry out an initial (automatic) filtering where we select trajectories that **(i)** include at least 6 motion steps (which is equivalent to a trajectory with a minimum length of 7 frames) and **(ii)** have a unidirectional travel distance of at least 6 pixels (pixel $\cong 230\text{nm}$). Next, we to perform a more delicate (manual) filtering where we exclude NPs, or NP trajectories, that fall under one or more of the following categories: (i) The NP shape is not symmetric or too large, which implies NPs aggregation, (ii) the NP is moving in a region where the density of MTs is too dense, and thus, it is impossible to discern between individual MT tracks, and (iii) the NP moves only for a short period and then get stuck along the MT track for a long period of time. Note that there are cases where the NPs are moving continuously between crossing MTs tracks. In that case, we extract the trajectory on each of the MT tracks separately. The overall run time and run length are calculated from the accumulated traveled time/distance.

The NP velocity v was calculated by taking the NP's center-of-mass position at times t, $\left(X(t), Y(t)\right)_{\text{NP}}$ and $t + \Delta t$ $\left(X(t+\Delta t), Y(t+\Delta t)\right)_{\text{NP}}$, and dividing by Δt, that is $v = \frac{\Delta \boldsymbol{r}_{\text{NP}}}{\Delta t} = \frac{(X(t+\Delta t)-X(t), Y(t+\Delta t)-Y(t))_{\text{NP}}}{\Delta t}$, where X and Y refer to lab frame Cartesian coordinates. The longitudinal velocity, v_x, was calculated by projecting the NP velocity v onto the MT direction (By definition, positive direction points towards the MT minus end), i.e., the unit vector of the MT (along its long axis), $\hat{u}_{MT} = \frac{\Delta \boldsymbol{r}_{\text{MT}}}{|\Delta \boldsymbol{r}_{\text{MT}}|}$, where $\Delta \boldsymbol{r}_{\text{MT}} = (X_f - X_i, Y_f - Y_i)_{\text{MT}}$. The indexes i and f, are the NP trajectory initial and final time points, and $(X_i, Y_i)_{\text{MT}}$ and $\left(X_f, Y_f\right)_{\text{MT}}$ are the corresponding

MT center-of-mass coordinates. Thus, the longitudinal velocity $v_{\mathrm{x}} = v \cdot \hat{u}_{MT} = \frac{(X(t+\Delta t)-X(t),Y(t+\Delta t)-Y(t))_{\mathrm{NP}}}{\Delta t} \cdot \frac{(X_f-X_i,Y_f-Y_i)_{\mathrm{MT}}}{|\Delta \boldsymbol{r}_{\mathbf{MT}}|}$, where $|\Delta \boldsymbol{r}_{\mathbf{MT}}| = \sqrt{(X_f - X_i)^2 + (Y_f - Y_i)^2}$. Positive v_{x} corresponds to NP motion in the direction of the MT minus end (anterograde), whereas negative values of v_{x} refers to NP motion towards the MT plus end (retrograde).

Similarly, the transverse motion, v_y, was determined by projecting the NP velocity v onto the normal unit vector of the MT, $\hat{n}_{MT}$. Thus, the transverse velocity $v_{\mathrm{y}} = v \cdot \hat{n}_{MT}$ and the corresponding transverse step is given by $\Delta y = v_{\mathrm{y}} \Delta t$. Note, that for each MT, or MT unit vectors $\hat{u}_{MT}$, there are two opposite normal unit vectors that can be assigned, $\hat{n}_{1,MT}$ and $\hat{n}_{2,MT}$, that account for positive and negative NP transverse motions, respectively (Fig. S3.1). In this paper, we have defined right-handed transverse motion as positive and left-handed transverse motion as negative (see Fig. 2B in the main text for spatial orientation).

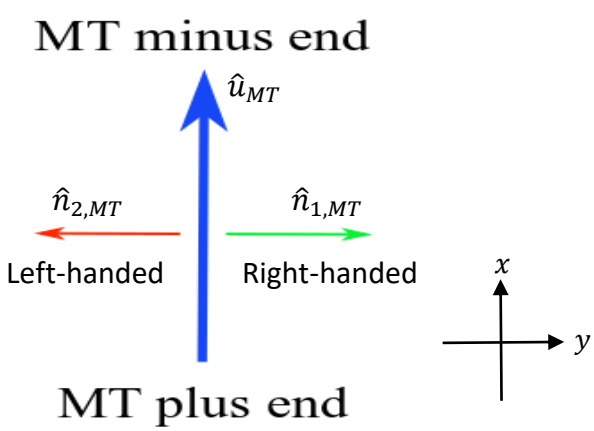

Fig. S3.1 – Illustration of the $\hat{u}_{MT}$ vector (blue arrows) and of the two $\hat{n}_{MT}$ vectors (green and red arrows).

Next, we filter Δy and Δx as follows: we use the known step-time interval of each experimental setup to calculate the instantaneous longitudinal, v_x, transverse, v_y, and absolute, $v = \sqrt{v_x^2 + v_y^2}$, velocities. We then set a maximum absolute value for the absolute velocity: 4000 nm, which represents to the very rare – and somewhat not plausible – case where the dynein steps 100 consecutive 40 nm sized steps. If the absolute velocity of a step exceeds this maximum value, the step is not taken into account. In addition, for the angular velocity and helical pitch calculations, we examine the transverse step size of the different NPs. We assume that the maximum size of a

transverse step ($\Delta y = 2 \times R_{\mathrm{orb}} = 2 \times 153$ nm – see below), which corresponds to the scenario where the NP moves half a circle along the MT perimeter, from left to right, or *vice versa*. Therefore, any motion that involves a transverse step that is larger than the said limit is omitted.

Following the Δy calculation and filtration, we use the mean value of transverse steps, $\langle \Delta y \rangle$, to extract the mean angular velocity, $\langle \omega \rangle$, and its error, ω_e, as follows:

$$\langle \omega \rangle \pm \omega_e = \frac{1}{\Delta \mathrm{t}} \arcsin\left(\frac{\langle \Delta y \rangle}{\mathrm{R_{orb}}}\right) \pm \frac{1}{\Delta \mathrm{t}} \left(\frac{\langle \Delta y \rangle}{\mathrm{R_{orb}}} \times \frac{1}{\sqrt{1-\left(\frac{\mathrm{SEM}(\Delta y)}{\mathrm{R_{orb}}}\right)^2}} \right) \qquad \text{(eq. 3.1)}$$

Where $\mathrm{SEM}(\Delta y)$ is the standard error of the mean (SEM) value of Δy, and R_{orb} is the approximated distance between the MT and NP centers (see Figs. 2B and 6A in the main text) which reads:

$$R_{\mathrm{orb}} = R_{MT} + \max(\mathrm{R_{N-NP}}) + a + d_{\mathrm{dynein}} + d_{\mathrm{Importins}} \cong 153 \text{ nm} \qquad \text{(eq. 3.2)}$$

Where R_{MT} ($= 12.5$nm) is the MT radius, $\mathrm{R_{N-NP}}(= 27.5\text{nm } to\ 40\text{nm})$ is the NeutrAvidin-coated NP radius, a ($= 40.68$ nm) is the PEG polymer contour length, $\mathrm{d_{dynein}}$ ($= 45\text{nm}^*$) is the dynein characteristic dimension, and $d_{\mathrm{Importins}}$ is the α and β importin complex dimension ($= 15\text{nm}^{**}$).

Next, we estimate the mean helical pitch, $\langle \bar{\mathrm{H}} \rangle$, and its corresponding error, H_e, by

$$\langle \bar{\mathrm{H}} \rangle \pm \bar{H}_e = \frac{2\pi}{|\langle \omega \rangle|} |\langle v_x \rangle| \pm \sqrt{\left(\frac{2\pi}{\langle \omega \rangle} \times SEM(v_x)\right)^2 + \left(\frac{2\pi \times \langle v_x \rangle}{\langle \omega \rangle^2} \times \omega_e\right)^2} \qquad \text{(eq. 3.3)}$$

where $SEM(v_x)$ is the SEM value of Δv_x.

* d_{dynein} is estimated as follows: The dynein structure, without the tail domain, can be said to consist of three major domains: MTBD, stalk, and AAA+ ring, with the approximated dimensions of 4, 15, and 10 nm, respectively – a total of 30 nm (14, 15). The length of the dynein ($\mathrm{d_{dyn}}$), more or less, equals to the length of the dynein heavy chain. It is known (16) that two-thirds of the chain (C-terminal) spans from the MTBD to the AAA+ ring, and the remaining portion is the "tail" domain backbone (N-terminal). Therefore, a simple calculation leads to a total length, $\mathrm{d_{dyn}}$, of about 45 nm.

** $d_{Importins}$ is taken as 15nm. However, it is a rough estimation obtained by using Chimera that lies between two conformations: dense and relaxed (17, 18)

SI. 4 Experimental Raw Data for Unidirectional Motion

	I	II	III	IV	V
[NLS] [μM]	0.025	0.05	0.05	0.3	0.3
$\langle \boldsymbol{N} \rangle$	5.2	10.4	10.4	36.6	36.6
[CE] [μM]	3.4	3.4	3.4	3.4	6.8
#steps	80	62	362	134	536
$\langle \lvert \boldsymbol{v} \rvert \rangle$ [nm/sec]	905±18	793 ± 16	842 ± 28	493 ± 23	320 ± 20
$\langle \boldsymbol{v_x} \rangle$ [nm/sec]	815±68	769 ± 49	642 ± 29	422 ± 26	72 ± 22
$\langle \boldsymbol{v_x} \rangle \mid \boldsymbol{v_x} > \mathbf{0}$ [nm/sec]	939±57	783 ± 48	749 ± 21	476 ± 22	253 ± 20
$\langle \boldsymbol{v_x} \rangle \mid \boldsymbol{v_x} < \mathbf{0}$ [nm/sec]	-305±141	-91 ± 0	-545 ± 140	-224 ± 76	-319 ± 43
$\langle \boldsymbol{v_y} \rangle$ [nm/sec]	1.7 ± 25	-0.07 ± 24	252 ± 23	67 ± 16	39 ± 10
$\langle \boldsymbol{v_y} \rangle \mid \boldsymbol{v_y} > \mathbf{0}$ [nm/sec]	190±24	173 ± 23	284 ± 23	92 ± 13	132 ± 9
$\langle \boldsymbol{v_y} \rangle \mid \boldsymbol{v_y} < \mathbf{0}$ [nm/sec]	-152±23	-143 ± 16	-299 ± 75	-277 ± 104	-162 ± 18
$\langle \boldsymbol{\tau_p} \rangle$ [sec]	2.1±0.4	3.0 ± 0.8	4.1 ± 0.5	11.7 ± 1.4	23.3 ± 4.1
$\langle \boldsymbol{\lambda}^* \rangle$ [nm]	2200±300	2600 ± 540	4100 ± 820	4900 ± 750	7700 ± 1100
$\langle \boldsymbol{\lambda} \rangle$ [nm]	1700±260	2300 ± 480	3100 ± 660	4300 ± 680	1700 ± 600
Fractions of forward & backward steps	0.9 f | 0.1 b	*0.98 f | 0.02 b*	0.92 f | 0.08 b	0.92 f | 0.08 b	0.67 f | 0.33 b
Fraction of Right- & Left-handed steps	0.45 r | 0.55 l	0.45 r | 0.55 l	0.94 r | 0.06 l	0.93 r | 0.07 l	0.67 r | 0.33 l

Table S4.1 – NPs experimental mean velocities, run-times, and run-lengths for the unidirectional motion of systems I to V (mean $\pm$ SEM). υ is the absolute velocity, υ_x is the longitudinal velocity, υ_y is the transverse velocity, τ_p is the processivity time, λ^* is the absolute and total distance that the NP covered regardless of the motion direction, and λ is the total longitudinal run length in the direction of the MT minus-end. Note that for system II, there is only a single NP step towards the MT plus-end. Thus, the corresponding statistics are not reliable (italic). An identical cell extract was used in systems III, IV, and V, and another extract was used in systems I and II. The NPs mean diameter is 45 nm.

	I	II	III	IV	V
[NLS] [μM]	0.05	0.05	0.05	0.3	0.3
[CE] [μM]	3.4	3.4	3.4	3.4	6.8
#steps	80	62	378	154	573
$\langle \boldsymbol{\delta\lvert v\rvert} \rangle$ [nm/sec]	168	126	542	288	477
$\langle \boldsymbol{\delta v_x} \rangle$ [nm/sec]	605	386	567	326	518
$\langle \boldsymbol{\delta v_y} \rangle$ [nm/sec]	226	192	454	193	234
$\langle \boldsymbol{\delta \tau_p} \rangle$ [sec]	1.61	2.13	2.82	6.95	16.24
$\langle \boldsymbol{\delta \lambda^*} \rangle$ [nm]	1055	1436	4250	3610	4340
$\langle \boldsymbol{\delta \lambda} \rangle$ [nm]	932	1277	3450	3750	2390

Table S4.2 – NPs experimental velocity, run-time, and run-length STDs for the unidirectional motion of systems I to V**.** υ is the absolute velocity, υ_x is the longitudinal velocity, υ_y is the transverse velocity, τ_p is the processivity time, λ^* is the absolute and total distance that the NP covered regardless of the direction, and λ is the total longitudinal run length in the direction of the MT minus-end. An identical cell extract was used in systems III, IV, and V, and another extract was used in systems I and II. The NPs mean diameter is 45 nm.

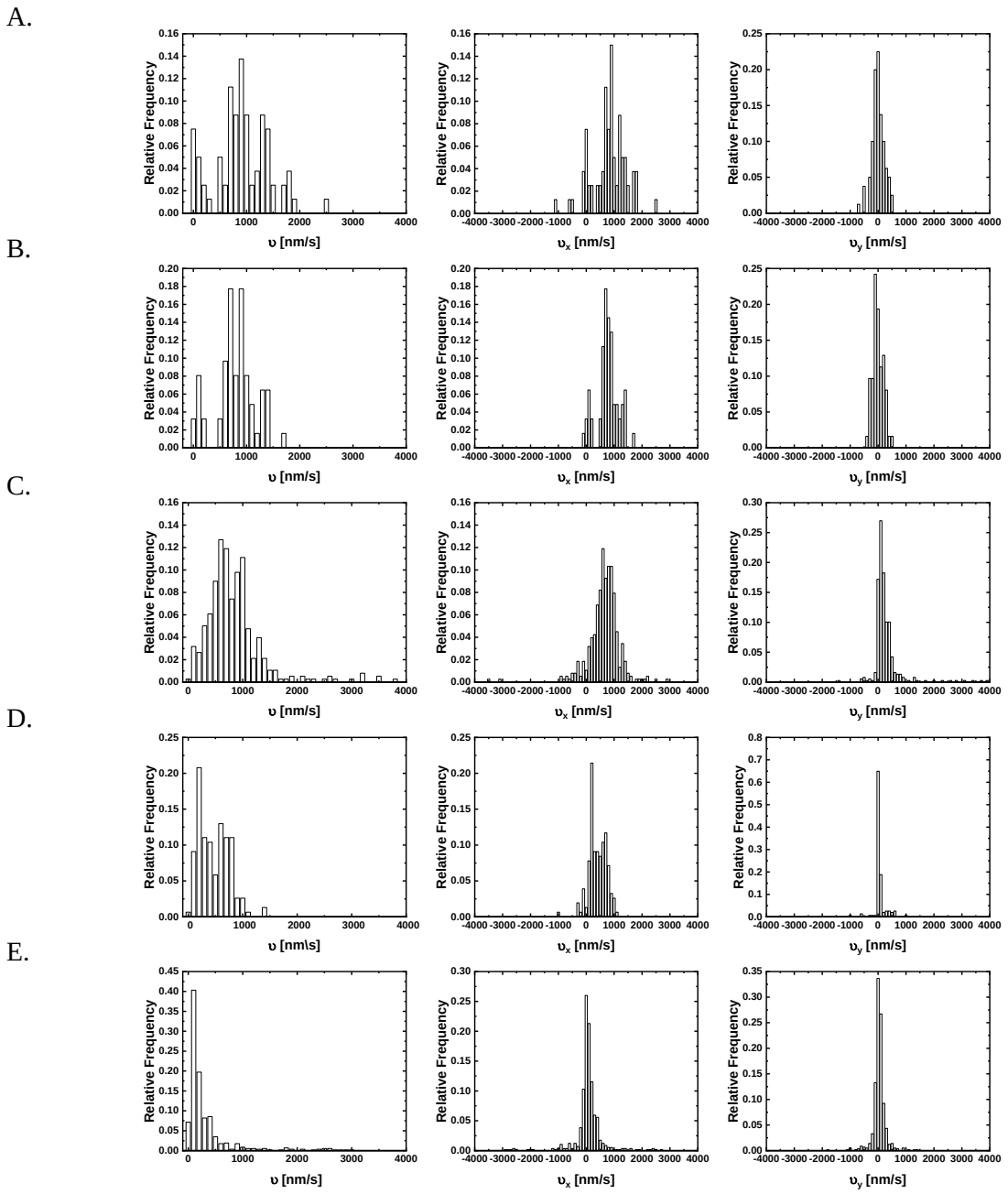

Fig. S4.1 – Histogram of the experimental velocities for systems I to V (rows A-E respectively), where υ is the absolute velocity, υ_x is the longitudinal velocity, and υ_y is the transverse velocity. The NPs mean diameter is 45 nm.

SI. 5 Experimental Raw Data for Bidirectional Motion

	III	IV
[NLS] [μM]	0.05	0.3
$\langle \boldsymbol{N} \rangle$	10.4	36.6
[CE] [μM]	3.4	3.4
#steps	68	74
$\langle \lvert \boldsymbol{v} \rvert \rangle$ [nm/sec]	597 ± 58	106 ± 14
$\langle \boldsymbol{v_x} \rangle$ [nm/sec]	-149 ± 60	-2 ± 18
$\langle \boldsymbol{v_x} \rangle \mid \boldsymbol{v_x} > \boldsymbol{0}$ [nm/sec]	307 ± 55	96 ± 20
$\langle \boldsymbol{v_x} \rangle \mid \boldsymbol{v_x} < \boldsymbol{0}$ [nm/sec]	-431 ± 58	-94 ± 20
$\langle \boldsymbol{v_y} \rangle$ [nm/sec]	-89 ± 68	-15 ± 6
$\langle \boldsymbol{v_y} \rangle \mid \boldsymbol{v_y} > \boldsymbol{0}$ [nm/sec]	387 ± 94	21 ± 5
$\langle \boldsymbol{v_y} \rangle \mid \boldsymbol{v_y} < \boldsymbol{0}$ [nm/sec]	-403 ± 52	-47 ± 6
$\langle \boldsymbol{\tau_p} \rangle$ [sec]	6 ± 2	121
$\langle \boldsymbol{\lambda^*} \rangle$ [nm]	5140 ± 970	1257
$\langle \boldsymbol{\lambda} \rangle$ [nm]	-950 ± 560	-205
Fractions of forward & backward steps	0.38 f | 0.62 b	0.49 f | 0.51 b
Fraction of Right- & Left-handed steps	0.39 r | 0.61 l	0.46 r | 0.54 l

Table S5.1 – NPs experimental mean velocities, run-times, and run-lengths for the bidirectional motion of systems III and IV (mean $\pm$ SEM). υ is the absolute vectorial velocity, υ_x is the longitudinal velocity, υ_y is the transverse velocity, τ_p is the processivity time, λ^* is the absolute and total distance that the NP covered regardless of the direction, and λ is the total longitudinal run length in the direction of the MT minus-end. The NPs mean diameter is 45 nm.

SI. 6 Experimental angular velocity $\boldsymbol{\omega}$ and helical pitch $\bar{H}$ estimations

System	**[NLS]** [μM]	**[CE]** [μM]	$\boldsymbol{\omega}$ [rad/sec]	$\boldsymbol{\omega}\vert\boldsymbol{v_x} > \mathbf{0}$ [rad/sec]	$\boldsymbol{\omega}\vert\boldsymbol{v_x} < \mathbf{0}$ [rad/sec]	$\langle\bar{\boldsymbol{H}}\rangle$ [nm]
I	0.025	3.4	-0.02 ± 0.24	-0.11 ± 0.25	0.67 ± 0.84	$2.6 \times 10^5 \pm 3.1 \times 10^6$
II	0.05	3.4	0.019 ± 0.18	-0.012 ± 0.19	0.38 ± 0.24	$2.6 \times 10^5 \pm 2.5 \times 10^6$
III	0.05	3.4	1.25 ± 0.08	1.30 ± 0.07	0.71 ± 0.54	3150 ± 243
System	**[NLS]** [μM]	**[CE]** [μM]	$\langle\boldsymbol{H}\rangle\vert\boldsymbol{v_y} > \mathbf{0}$ [nm]	$\langle\boldsymbol{H}\rangle\vert\boldsymbol{v_y} < \mathbf{0}$ [nm]		
I	0.05	3.4	820 ± 110	720 ± 90		
II	0.025	3.4	820 ± 130	800 ± 70		
III	0.05	3.4	2900 ± 130	110 ± 440		

Table. S6.1 – Angular velocity, ω, and estimated helical pitch size, $\langle\bar{H}\rangle$, for systems I, II, and III (mean $\pm$ error). An identical cell extract was used in system III, and another extract was used in systems I and II. The NPs mean diameter is 45 nm.

SI. 7 Stepping Model for Mammalian Cytoplasmic Dynein

In a previous publication (19), we presented a stochastic model for the 2D stepping of single cytoplasmic yeast dynein, which shows an excellent agreement with experimental results. Here, we use a similar model for single mammalian dynein. Although these two motor proteins differ in several aspects, the conversion of our yeast dynein stepping model to the mammalian case can be achieved using a few assumptions and additional experimental data.

The main assumptions concerning single dynein stepping are: **(i)** We assume that both yeast and mammalian dynein microtubule-binding domains (MTBDs) bind to the same binding sites on the MT surface. **(ii)** We assume that all the required biological factors, such as bicaudal-D-homolog-2 (BICD2) and dynactin, are at optimal concentrations, allowing us to neglect their binding-unbinding kinetics. **(iii)** Our model, for both dynein types, regards the stepping vector probability distribution, $P(\vec{L})$, as a product of two functions: $P(\vec{L}) = A\, W(\vec{L})\, G(\vec{L})$, where $\vec{L}$ is the dynein step vector (with longitudinal and transverse components L_x and L_y respectively), and A is a normalization factor. $W(\vec{L})$ is a motor-specific function that accounts for the stepping model rules (19) and is an asymmetric function (i.e., invariant under the transformation $\vec{L} \to -\vec{L}$); thus, its projection along L_y, i.e., $w(L_y) = \int_{-\infty}^{\infty} dL_x W(\vec{L})$, is also a symmetric function of its variable. $G(\vec{L})$ is a force exertion function. It includes the internal, longitudinal, motor force, equal in magnitude to the so-called stalling force F_s, thus breaking the symmetry between forward (anterograde) and backward (retrograde) steps. It also may include any external potential $U(\vec{L})$ (with the definition $U(0) = 0$). It is given by

$$G(\vec{L}) = \frac{1}{1+exp[-\frac{L_x F_S - U(\vec{L})}{k_B T_{\text{eff}}}]} \qquad \text{(eq. 7.1)}$$

where T_{eff} is an effective temperature fit parameter. In particular, as considered in previous works(19, 20), for a longitudinal backward pulling force (taking F>0) $U(\vec{L}) = FL_x$ and

$$G(\vec{L}) = \frac{1}{1+exp[-\frac{L_x(F_S - F)}{k_B T_{\text{eff}}}]} \qquad \text{(eq. 7.2)}$$

The above assumptions are not sufficient for the model adjustment, i.e., to obtain $W(\vec{L})$, as done for the yeast case. For example, to the best of our knowledge, for the mammalian case, no

data is published on the inter-MTBD stretching distance distribution and/or its angular distribution. Therefore, to complete the model, we use here the very recent single-molecule results on mammalian dynein stepping statistics of Canty and Yildiz (21). To do so, we consider only the experimental data regarding the BICD2 adapter, as this was shown to bind mainly just single dynein (~85%)(22). Specifically, we use the experimental data for the dynein pivot longitudinal step size distribution under stalling conditions $F = F_s$, in Eq. 2. Under such conditions, our model reads $P(\vec{L}) = \frac{1}{2} A\, W(\vec{L})$. Yet, the provided data only entails the distribution of the longitudinal component L_x. Thus, to obtain $W(\vec{L})$, we build on the assumption (i) of the previous paragraph, which implies that the one-to-one correspondence, between longitudinal and transverse step components (L_x and L_y, respectively) is identical for both yeast and mammalian dynein motors. Using this correspondence, we can infer the distribution of the mammalian L_y from its L_x distribution and, in turn, its $\vec{L}$ distribution. In addition, to artificially reach adequate step sampling, we build on the symmetry discussed above for $W(\vec{L})$, which implies that ideally the raw data(21) should be composed of pairs of $(\vec{L}, -\vec{L})$ abundance. We observed that in the raw data some pairs are not completed (obviously due to the statistical error associated with finite-size sampling, and not due to experimental issues). Thus, we have forced the symmetry over the given data by completing the lacking pairs.

Next, we obtained the fit parameter T_{eff} by adjusting its value such that under no external force, $F = 0$, the retrograde and anterograde steps fractions are consistent with the empirical values: 23% and 77%, respectively, leading to $T_{\text{eff}} = 1900$ K. To further validate the said adjustments, we compared our predictions with the data(21) for different F values, see Table. S7.1. Note that all experimental data, except the one at vanishing load ($F = 0$), is consistent with our single cytoplasmic mammalian dynein model predictions (within theoretical and experimental errors).

F [pN]	Experimental	Theoretical
0	11.4$\pm$1.1 nm	9.1 nm
1.5	5.4$\pm$1.5 nm	6.9 nm
2.3	4.3$\pm$1.5 nm	5.2 nm
2.9	2.5$\pm$1.5 nm	3.3 nm
3.6	-0.5$\pm$1.5 nm	0.3 nm

Table S7.1 – Comparison between experimental and theoretical stepping of a single dynein (mammalian-type). Since the experimental results are affected by the FIONA method resolution of $\pm 1\ nm$, the error in the experimental results is estimated as $\pm\sqrt{1 + SEM^2}$. We believe that the small mismatch between model and experiment at $F = 0$ is likely due to an experimental error at vanishing laser trapping forces[1].

[1] In any case, it should have only a relatively small effect on the motion of the NP. First, during the periods with simultaneous binding of more than one motor, it is very rare to find a motor at zero load. Second, during the periods of single motor binding, the only effect of the above mismatch is on the temporal velocity, which we adjust to the known value by fitting the step time to 0.0108 sec.

SI. 8 Simulation and Algorithm

Our simulations are based on the well-known Monte-Carlo (MC) method, which simulates the processes that occur on timescales much longer than both and the polymer Zimm relaxation time, and the NP rotational and translational timescales – both associated with thermal diffusion, controlling fluctuations, and with relaxation times for reaching mechanical equilibrium. These times are estimated in SI Sec.9 for completeness.

We simulate the motion of a 20 nm radius nano-particle (NP) that is coated with a fixed number of polymers grafted to its surface, each ending with a dynein motor protein. The number of grafted polymers per NP, N_m, is related to the particle radius R and anchoring spacing, ξ, as $N_m = 4\pi R^2/\xi^2$. To coincide with the experimental setup, we distribute the polymers randomly over the NP surface. We emphasize that we do not consider the actual dynein dimensions. Instead, we treat it as a simple cylindrical-like body, with a radius of 10 nm and a height of 60 nm. The height is an approximation that is built from the accumulated dimensions of the dynein components and the $\alpha\beta$ importin complex (SI. Sec.3). The reasoning behind the 10 nm radius is explained below.

The microtubule (MT) surface, which the motors step over, is modeled as a cylinder with a 12.5 nm radius. The MT surface is covered with binding sites for the dynein microtubule-binding domain (MTBD). As our simulation does not take into consideration the dynein detailed structure (to reduce computation time), we used the MT-MTBD binding site lattice (as presented in our previous work(19)) to create an artificial MT-dynein (i.e., dynein pivot) binding site grid. We did it by sampling all the possible configurations of an MTBD pair, and for each of the configurations, we calculated the corresponding location of the dynein pivot.

The simulation algorithm, which describes a single NP trajectory, includes a sequence of events, beginning with the attachment of a single motor to the MT, and ending when the last motor detaches (henceforth, we use the term "motor" to refer to the dynein-polymer complex). Each simulation iteration (MC-step) involves one of the following competing events that is allowed for each of the motors: (i) motor binding (for unbound motors), (ii) unbinding (for the bound motors), or (iii) stepping (for the bound motors); the latter might lead to a jamming event as discussed below. The probability of each event i is proportional to its rate, k_i. To avoid a non-vanishing probability for no occurrence of any of the three events, we choose all event probabilities to sum up to unity (at each MC-step), such that the probability of an event j is given by $P_j = \frac{k_j}{\sum_i k_i}$. With

this choice, the physical time of an MC step is $\delta t = \frac{1}{\sum_i k_i}$, implying that this time increment varies between different MC steps. For convenience, we separate the events to the above three groups such that the rate for an event class is $K_\alpha = \sum_{i \in \alpha} k_i$, with α=(binding, unbinding, and stepping), such that the sum on $i \in \alpha$ runs over the different participating motors; the corresponding probability for each event class α is $P_\alpha = \frac{K_\alpha}{\sum_\beta K_\beta}$. Thus, after an event group has been randomly selected, a second random selection is performed for the actual event. For instance, a random selection of a "binding" process (out of the three processes) is followed by the selection of the motor identity out of the unbound motors. After each such MC-step, the NP is balanced mechanically by minimizing the free-energy, mimicking processes that are orders of magnitude faster than the MC physical timescale (see estimated time scales in SI Sec.9).

In the following sections, we shall discuss the free-energy calculations, rate calculations, and the NP stepping algorithm.

Stepping model application to the NP

The single motor stepping model described in the previous chapter can be readily applied to any of the NP motors that are attached to MT and attempt to step. In Eq. 1, we identify the "external potential" as the Helmholtz free-energy change of the NP upon making this step and (instantaneous) mechanical balance as described above, $U(\vec{L}) \equiv \Delta U_{NP}(\vec{L})$.

Motor free-energy

We assume that the anchoring density is in the so-called "mushroom regime" (4) (consistent with the experimental densities) such that $\xi > R_g$. Hence, polymer-polymer excluded volume interaction should not be accounted for, and for the free-energies calculation, we can consider a single polymer.

We choose a planar surface that is tangent to the spherical NP surface at the polymer anchoring position, see Fig. S8.1. When the dynein at the polymer free-end (henceforth "dynein-polymer-end") binds to a site at MT surface, the polymer-end can be regarded as fixed in space, with position dictated by the dynein and importins dimensions (see SI Sec.3). Thus, dynein-polymer-end position is always residing on a virtual cylindrical surface whose cross-section radius is the sum of the MT radius, the total dynein length, and the two importin protein sizes (SI Sec.3).

To describe the free-energy change upon this binding event, we use a function that accounts for the entropy loss of a polymer upon binding, and the dynein binding energy gain, $\epsilon > 0$. Using cylindrical coordinates $(\vec{\rho}, z)$ associated with this tangent surface, the polymer anchoring position is set at the origin (0,0), and the polymer another end, which is not anchored to the surface, is fixed at $(\vec{\rho}, Z)$ (Fig S8.1).

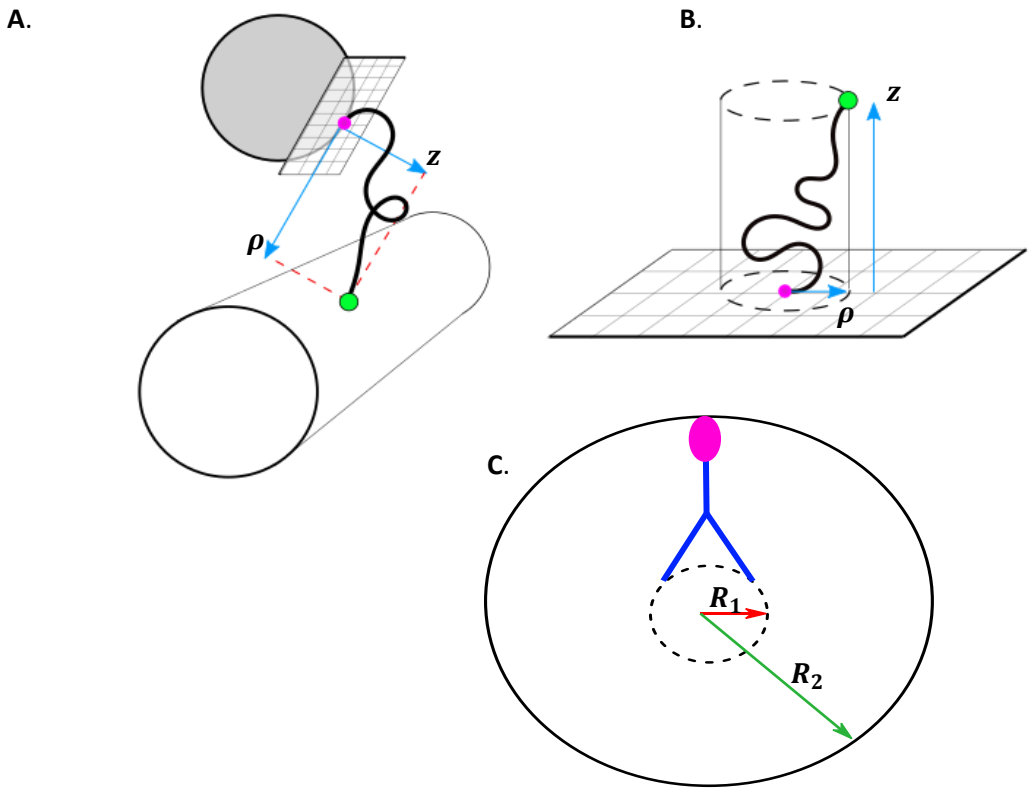

Fig S8.1 – Illustration of the cylindrical coordinates $(\vec{\rho}, z)$. **(A)** illustration of the coordinates for the case of a polymer that connects between a NP (gray circle) and the $\alpha\beta - importin - complex$ that in turn, is connected to the dynein tail domain (green dot). **(B)** Illustration of the coordinates for the general case. **(C)** Illustration of the cylinder from (A). Note that the effective radius of the cylinder, R_2 (green arrow) entails the MT radius, R_1 (red Arrow), the vertical length of the dynein (blue lines), and the vertical length of the $\alpha\beta - importin - complex$ $(pink\ elipse)$. Therefore, the value of R_2 is taken as 60 [nm] (the length estimation is discussed in detail in SI Sec.3)

This leads to the following equation for the change in the free-energy, ΔU, between a fixed and free-end polymer(23, 24) :

$$\Delta U_{\text{motor}} = -\epsilon - k_B T \times \left[ln\left(\frac{9Za^3}{2\pi R_0^2}\right) - \frac{3}{2}\left(\frac{\rho^2+Z^2}{R_0^2}\right)\right] \qquad \text{(eq. 8.1)}$$

where a is the polymer Kuhn length (~0.76 nm for PEG(10, 11)) $R_0 = \sqrt{N_a}\, a$ is the free-polymer end-to-end distance (N_a is the number of Kuhn segments). We approximate ϵ to be $8k_BT$ (25).

Note that this free-energy approximately accounts for the excluded volume interaction between the whole polymer and the NP rigid surface (assuming $R_g \ll R$). It does not account for the excluded-volume interaction between the polymer and the MT surface. However, since the contour length of the PEG is about 30 nm, it is evident that no monomer can ever reach the MT itself. The excluded-volume interaction between the polymer and the body of the dynein-$\alpha\beta$ complex is neglected since – for similar considerations – the only domains where it could be relevant are the dynein tail and the two importins whose physical dimensions are relatively small.

<u>Coordinate Transformation:</u> As each polymer in anchored at a different position on the NP surface, its anchoring tangent plane is orientated differently with respect to the MT surface. Thus, we perform a coordinate transformation for each polymer to obtain its specific ΔU_{motor}.

In Eq. 3, $\rho^2 + Z^2$ stands for the square of the (actual) end-to-end vector $\Delta\vec{r} = \vec{r}_f - \vec{r}_i$ (Fig. S8.1). Redefining the origin at the NP center, the grafting position (pink dot) is taken at $\vec{r}_i = (x_1, y_1, w_1)$, and dynein-polymer-end coordinates (green dot) are taken at $\vec{r}_f = (x_2, y_2, w_2)$. Using these coordinates,

$$(\Delta\vec{r})^2 = \rho^2 + Z^2 = (x_2 - x_1)^2 + (y_2 - y_1)^2 + (w_2 - w_1)^2 \qquad \text{(eq. 8.2)}$$

The unit normal vector to the NP surface at the anchoring position is parallel to $\vec{r}_i$ and is therefore

$\hat{n} = \frac{(x_1, y_1, w_1)}{\sqrt{x_1^2+y_1^2+w_1^2}}$. Since $Z = |\Delta\vec{r}|\ cos\gamma$, where γ is the sharp angle between $\hat{n}$ and $\Delta\vec{r}$, it follows

$$Z = \hat{n} \cdot \Delta\vec{r} = \frac{x_1(x_2-x_1)+y_1(y_2-y_1)+w_1(w_2-w_1)}{\sqrt{x_1^2+y_1^2+w_1^2}} \qquad \text{(eq. 8.3)}$$

Motor Stepping rate

For a single motor, the mean stepping rate, k_{step}, can be obtained from $k_{\text{step}} = \langle \upsilon_x \rangle / \langle L_x \rangle$, where υ_x is the longitudinal velocity [nm/sec], and L_x is the longitudinal step size [nm]. For mammalian cytoplasmic dynein, we set $\langle \upsilon_x \rangle$ to be the well-established 800 nm/sec, and $\langle L_x \rangle$ to be about 9 nm. We assume constant k_{step} for all steps, irrespective of their size, even though each step size might be associated with a different rate. Note that k_{step} includes the dwell time.

Motor Binding/Unbinding rates

As described in Cohen and Granek work(26), we assume that the binding-unbinding rates of the different motors obey detailed balance relations. Therefore, the probability of finding the NP in a state i, having a free-energy F_{i} (playing the role of energy) is $\text{P}_{\text{i}} \propto \exp(-\frac{F_{\text{i}}}{\text{k}_{\text{B}}\text{T}})$. Using the well-known detailed balance condition for the rates considered, k_+ (binding) and k_- (unbinding), $\frac{k_+}{k_-} = \exp\left[-\frac{F_+ - F_-}{k_B T}\right]$, where F_+ and F_- are the free-energies of binding and unbinding states respectively, together with two extra conditions: (i) $k_+ + k_- = \tau^{-1}$, and (ii) $k_{-,\text{single}} = k_0 = 1$ Hz, where k_0 is the unbinding rate of a single motor (20) , leads to the following rate expressions:

$$k_- = \tau^{-1} \frac{1}{1+exp\left(-\frac{\Delta U_{NP}}{k_B T}\right)} \qquad \text{(eq. 8.4)}$$

$$k_+ = \tau^{-1} \frac{exp\left(-\frac{\Delta U_{NP}}{k_B T}\right)}{1+exp\left(-\frac{\Delta U_{NP}}{k_B T}\right)} \qquad \text{(eq. 8.5)}$$

$$\tau^{-1} = k_0 \left(1 + exp\left(-\frac{\Delta U_0}{k_B T}\right)\right) \qquad \text{(eq. 8.6)}$$

where $\Delta\text{U}_{\text{NP}} = F_- - F_+$ is NP free-energy difference between a (single motor) binding and unbinding states, and ΔU_0 is associated with the special case where the NP entails only a single

motor. Note ΔU_{NP} accounts for the free-energy change of the whole NP upon a single unbinding event of one of the motors, $\Delta U_{NP} = \sum_i \Delta U_{\text{motor},i}$.

Excluded volume estimation and interactions

When a motor attempts to step into a binding site that is not accessible due to the "excluded volume interaction" between the attempting motor and the neighboring bound motors, a "jamming event" occurs – and the motor rests still, meaning that if an excluded-volume interaction occurs, the longitudinal and angular velocities (v_x and ω) both equal to zero. We determine the motor-motor excluded volume interaction using the following approach. First, the volume occupied by a single MTBD is described as a 4nm radius sphere (14), which allows determining the excluded volume created when two MTBDs meet in the conventional way (i.e., the volume of a sphere of the MTBD diameter). Note that the MTBD measured dimensions are likely smaller than those we use (4 > 3.6 nm); this practice ensures that we do not underestimate the volume occupied by the MTBD.

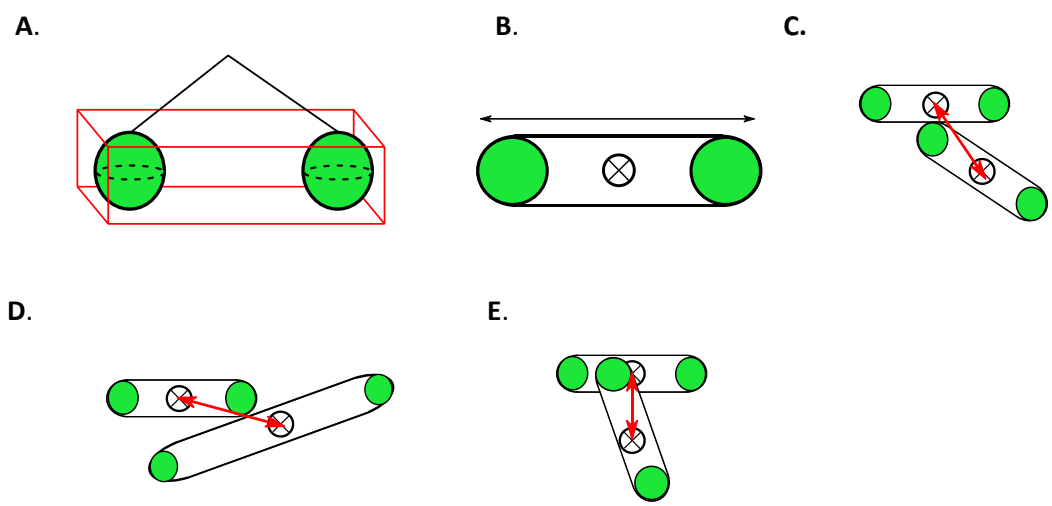

Fig. 0.1 – Illustration of the excluded volume and possible configurations of two MTBD pairs. MTBDs are represented by green circles and spheres. The dynein pivots are represented by ⊗, and the distance between two dynein pivots (d_{jam}) is represented by red arrows. **(A)** an illustration of the volume that is occupied by an MTBD pair and the space between the pair's MTBDs (red square). **(B)** an illustration of the projection of (A). **(C-D)** an example of two adjacent MTBD pairs. **(E)** an example of two MTBD pairs in "crossing" configuration.

Second, let us define $V_{\text{pair},i}$ as the volume occupied by the $\langle ij \rangle$ MTBD pair, where the space between the MTBDs is also taken into account (Fig. S8.2). An excluded volume jamming event is defined as any occurrence where $V_{\text{pair},\langle ij \rangle}$ and $V_{\text{pair},\langle k\ell \rangle}$ ($\langle ij \rangle \neq \langle k\ell \rangle$) overlap. However, since our model does not consider the actual dynein structure, we determined the average distance between two motors that leads to a jamming event (d_{jam}). We represent each V_{pair} as a projection on a 2D surface, or in other words, as a hemispherical capped ribbon with length, L (Fig. S8.2).

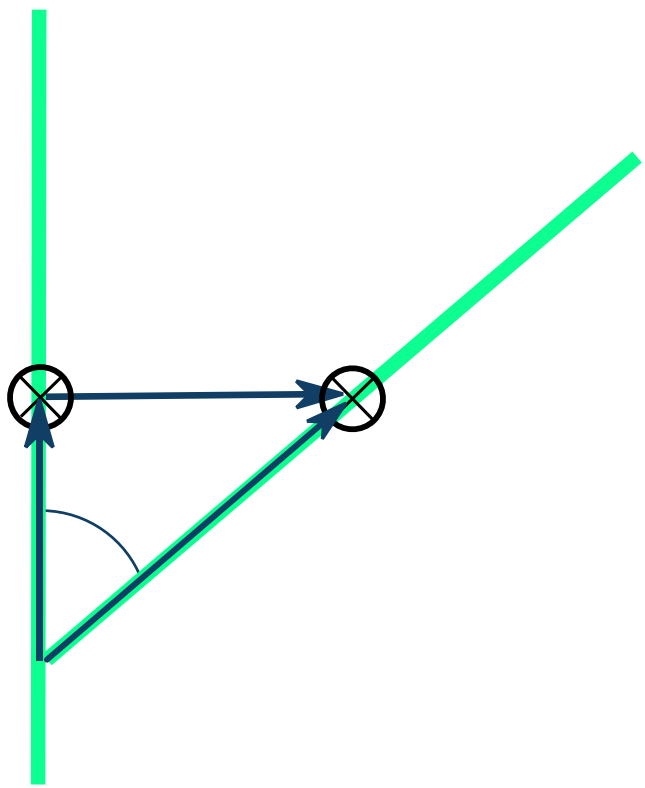

Fig. S8.2 – schematic illustration of a possible configuration of two MTBD pairs. MTBDs pairs are represented by green lines (with a length of L), and the dynein pivots are represented by ⊗**.**

Next, by integration, we approximate $\langle d_{\text{jam}} \rangle$ using the following calculation: we consider two such ribbons at contact (Fig. S8.3; see additional graphic examples in Fig. S8.2), making an angle α between them. Using the following geometrical relations for the vector positions of the two ribbon centers

$$|\vec{r_1}| = \frac{L}{2} - x \qquad \text{(eq. 8.7)}$$

$\vec{u}$

$$|\overrightarrow{r_2}| = \frac{L}{2} \qquad \text{(eq. 8.8)}$$

The vector connecting the two ribbon centers is

$$\vec{u} = \overrightarrow{r_2} - \overrightarrow{r_1} \qquad \text{(eq. 8.9)}$$

Thereby

$$u^2 = r_2^2 + r_1^2 - 2r_2 r_1 cos\alpha \qquad \text{(eq. 8.10)}$$

or

$$u_{x,\theta}^2 = \left(\frac{L}{2}\right)^2 + \left(\frac{L}{2} - x\right)^2 - 2\left(\frac{L}{2}\right)\left(\frac{L}{2} - x\right) cos\alpha \qquad \text{(eq. 8.11)}$$

The configurational average of this distance is

$$\langle u \rangle_{\text{config}} = \frac{1}{\frac{\pi}{2}} \int_0^{\frac{\pi}{2}} d\alpha \frac{1}{L} \int_0^L dx\, u(x, \alpha) \qquad \text{(eq. 8.12)}$$

which can be evaluated numerically to give

$$\langle u \rangle_{\text{config}} \cong 0.543\, L \qquad \text{(eq. 8.13)}$$

As the values of L vary, we use its mean, namely

$$d_{jam} = \langle \langle u \rangle_{\text{config}} \rangle_L = 0.543\, \langle L \rangle = 12 \text{ nm} \qquad \text{(eq. 8.14)}$$

Note that this approximation does not account for crossed configurations (Fig. S8.2). Thus, $d_{\text{jam}} = 12$ nm can only be taken as an upper boundary value, $\max(d_{\text{jam}})$. Therefore, to estimate $\min(d_{\text{jam}})$, the lower boundary value, we need to take into account the crossed configurations. However, as far as we know, there is no data concerning dynein-dynein crossing configurations, so we only examine a simple crossing case in which the likelihood for steric interferences is relatively low; we only consider the case where one MTBD resides between another pair of an MTBDs belonging to a neighboring motor (Fig. S8.2). To derive $\min(d_{\text{jam}})$, we use the same method as before, but do not account for the MTBDs dimension, resulting in shorter ribbon length, $L^* = L - 2d_{\text{MTBD}}$ (where $d_{\text{MTBD}} = 4$ nm is the "MTBD sphere" radius) such that ${d_{\text{jam}}}^* \cong 7.7$ nm. Since the real value of d_{jam} resides between the lower and the upper limits (i.e., between

7.7 and 12 nm), we take $\langle d_{\mathrm{jam}} \rangle$ to be 10 nm. Consequently, referring to the excluded volume, our motors are modeled as cylinders with a cross-section diameter of 10 nm, while their vertical length is estimated in SI. Sec.3.

Computer Simulation Algorithm

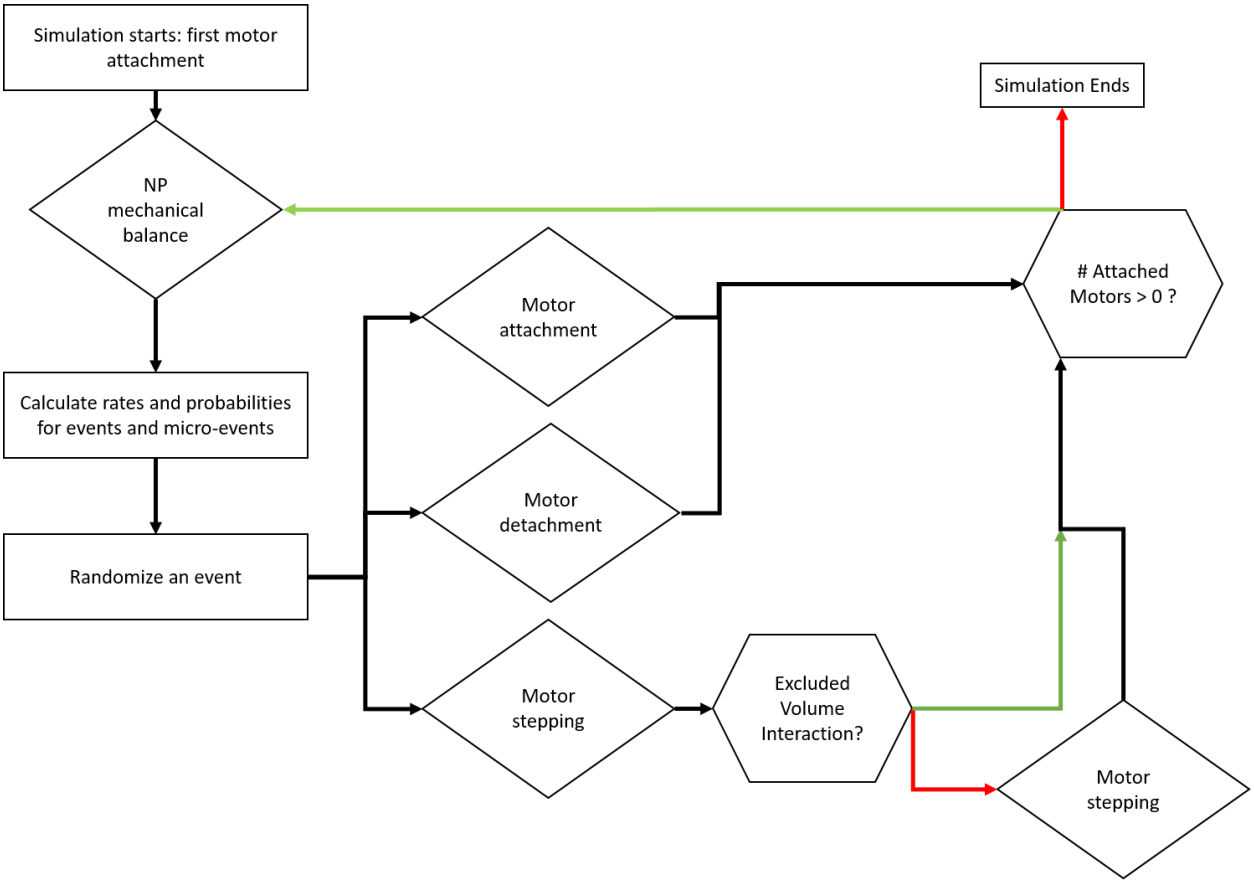

Fig. S8.3 – Scheme of the simulation algorithm. When a question block is presented (e.g., "Excluded Volume Interaction?"), green line represents positive answer, and red line represents negative answer.

SI. 9 Theoretical Time-scales Estimation

There are a few microscopic dynamical processes associated with the NP dynamics that were not accounted for explicitly in our model. As shown below, these processes are much faster than both timescales for motor stepping and motor binding-unbinding kinetics. This separation of timescales allows us to use a few model assumptions mentioned in the fourth chapter.

Consider first the Zimm relaxation time for the spacer polymer configurational fluctuations, $\tau_Z \approx \frac{\eta R_g^3}{k_B T}$, where η is the medium viscosity, and R_g is the gyration radius. More precisely, for a Gaussian chain(8), $\tau_Z = 0.325 \frac{\eta R_0^3}{k_B T} \simeq$ 12 ns, for the value of $R_0 \simeq 5.56$ nm used in this work. This is about 5 orders of magnitude shorter than the shortest MC step time in our simulations ($\tau_{MC} \sim 1$ ms). Hence, the polymer may be assumed to explore all its configurational phase space during any stepping, binding, or unbinding event (henceforth "MC-event"), which justifies the use of a polymer free-energy without accounting for the polymer dynamics explicitly.

Next, consider the NP translational and rotational motion. They are involved in the mechanical re-equilibration of the mean NP center of mass position and orientation after MC-event. They are also involved in the relaxation of thermal fluctuations around the mean position when no such events take place.

For the translational re-equilibration motion, assume that, after an MC-event, the NP requires to translate a distance r to reach translational mechanical equilibrium. This generates a (polymer) restoring force of magnitude at least $f = K_p r$, where K_p is the entropic (free-polymer) spring constant, $K_p = 3k_B T/R_0^2$. Note that – for large extensions (i.e., when $r \gg R_0$) – it is much higher. Therefore, this force can serve as an estimated lower bound. Using the NP translational Stokes drag coefficient, $\gamma_t = 6\pi\eta R$, we find an (upper bound) estimate for the translational relaxation time, $\tau_{\text{trans}} = \frac{\gamma_t}{K_p} = \frac{2\pi\eta R R_0^2}{k_B T} \simeq 8.4 \times 10^{-7}$ s (taking $R \simeq$ 20 nm). This value is about three orders of magnitude shorter than the shortest MC step time in our simulations, $\tau_{MC} \sim 1$ ms, thus allowing to assume that the translational equilibration occurs instantaneously after each MC-event.

Next, we wish to estimate the order of magnitude of the rotational equilibration time, avoiding

exhaustive details associated with the geometry. Assume that, after an MC-event, the NP requires to rotate an angle θ to reach rotational mechanical equilibrium. The torque exerted by a force f on the NP is roughly $T \sim fR \simeq K_p rR$, and the angle θ is related to the associated polymer extension by roughly $r \sim R\,\theta$ leading to a (restoring) torque $T \sim K_p R^2 \theta$. Using the rotational Stokes drag coefficient of the NP, $\gamma_\theta = 8\pi\eta R^3$, leads to the following estimate for the rotational relaxation time

$$\tau_{\text{rot}} \sim \frac{\gamma_\theta}{K_p\, R^2} \simeq \left(\frac{8\pi}{3}\right) \frac{\eta\, R\, R_0^2}{k_B T} \sim \tau_{\text{trans}} \ll \tau_{MC}\ ,$$

leading to the same conclusion.

Linear response theory suggests that the same relaxation times also govern the relaxation of thermal fluctuations near equilibrium, again suggesting that it is adequate to consider the mean center of mass position and mean orientation of the NP before and after an MC-event.

SI. 10 Theoretical raw data for $\Delta t = 0.27s$

N_m	1	2	3	4	5	6	7
$\langle v_x \rangle$	833 ± 4	769 ± 3	693 ± 2	640 ± 2	605 ± 1	584 ± 1	569 ± 1
$\langle \delta v_x \rangle$	245	297	322	326	321	315	308
N_m	8	9	10	11	12	13	
$\langle v_x \rangle$	557 ± 1	547 ± 1	540 ± 1	533 ± 1	528 ± 1	523 ± 1	
$\langle \delta v_x \rangle$	302	296	291	286	282	277	

Table S10.1 – Mean longitudinal velocity, $\langle v_x \rangle$, and STD, $\langle \delta v_x \rangle$, of the different (R, N_m) configurations for time intervals equal 0.27s. (mean $\pm$ SEM; see Fig. 8 in the manuscript).

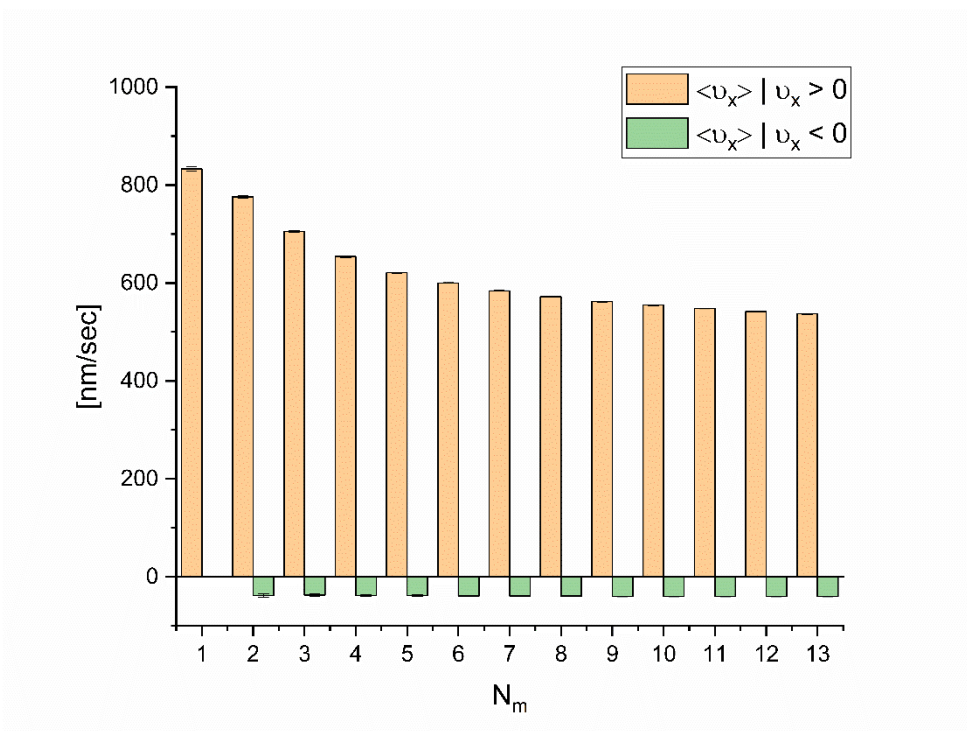

Fig. S10.1 – Mean instantaneous longitudinal velocity, $\langle v_x \rangle$, separated for anterograde, $v_x > 0$, and retrograde, $v_x < 0$, directions for the different (R, N_m) configurations for time intervals equal 0.27s.

N_m	1	2	3	4	5	6	7
$\langle v_x \rangle \mid v_x > 0$	833 ± 4	776 ± 3	705 ± 2	654 ± 2	621 ± 1	600 ± 1	584 ± 1
$\langle v_x \rangle \mid v_x < 0$	N/A	-38 ± 4	-37 ± 2	-38 ± 1	-38 ± 1	-39 ± 1	-39 ± 1
N_m	8	9	10	11	12	13	
$\langle v_x \rangle \mid v_x > 0$	572 ± 1	562 ± 1	555 ± 1	548 ± 1	542 ± 1	537 ± 1	
$\langle v_x \rangle \mid v_x < 0$	-39 ± 1	-40 ± 1	-40 ± 1	-40 ± 1	-40 ± 1	-40 ± 1	

Table S10.2 – Mean longitudinal velocity, $\langle v_x \rangle$, and STD, $\langle \delta v_x \rangle$, separated for anterograde, $v_x > 0$, and retrograde, $v_x < 0$, directions for the different (R, N_m) configurations for time intervals equal 0.27s (mean $\pm$ SEM).

N_m	1	2	3	4	5	6	7
$\langle \omega \rangle$	1.97 ± 0.14	1.79 ± 0.09	1.47 ± 0.06	1.28 ± 0.04	1.10 ± 0.03	0.97 ± 0.02	0.87 ± 0.02
$\langle \delta\omega \rangle$	8.16	7.88	7.28	6.78	6.37	6.06	5.80
N_m	8	9	10	11	12	13	
$\langle \omega \rangle$	0.80 ± 0.01	0.74 ± 0.01	0.68 ± 0.01	0.63 ± 0.01	0.59 ± 0.01	0.56 ± 0.01	
$\langle \delta\omega \rangle$	5.58	5.38	5.21	5.05	4.91	4.78	

Table S10.3 – Mean angular velocity, $\langle \omega \rangle$, and STD, $\langle \delta\omega \rangle$, of the different (R, N_m) configurations for time intervals equal 0.27s (mean $\pm$ SEM; see Fig. 11 in the manuscript).

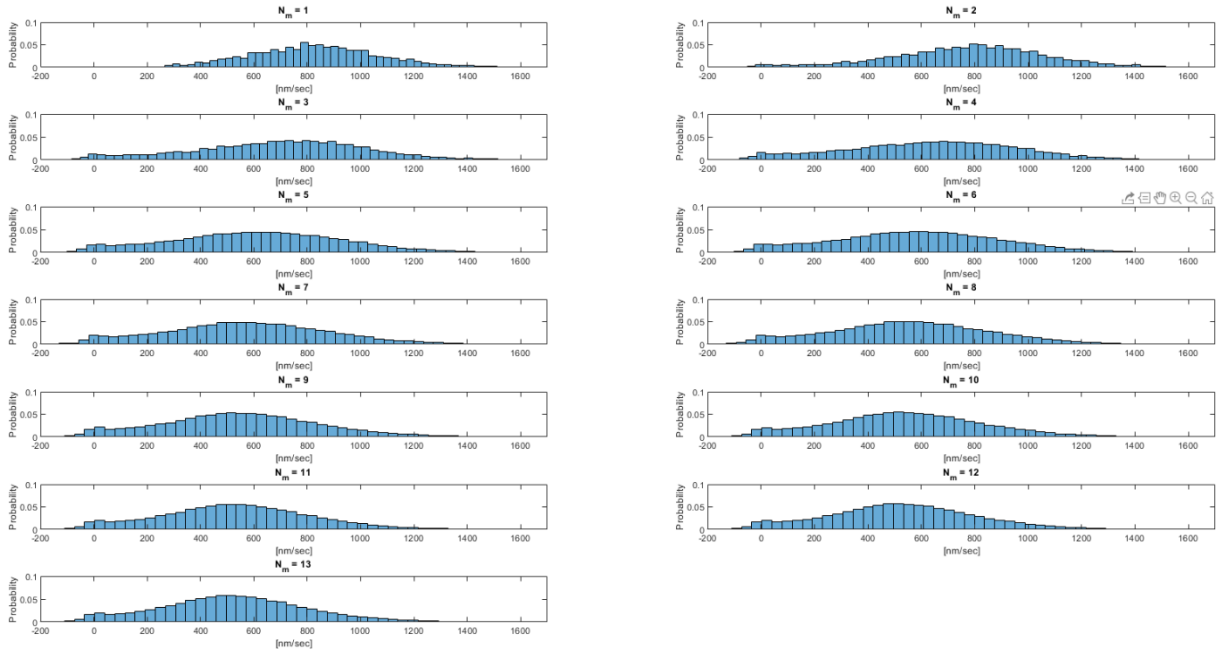

Fig. S10.2 – Distributions of the longitudinal velocity, v_x, for the different (R, N_m) configurations for time interval of 0.27s .

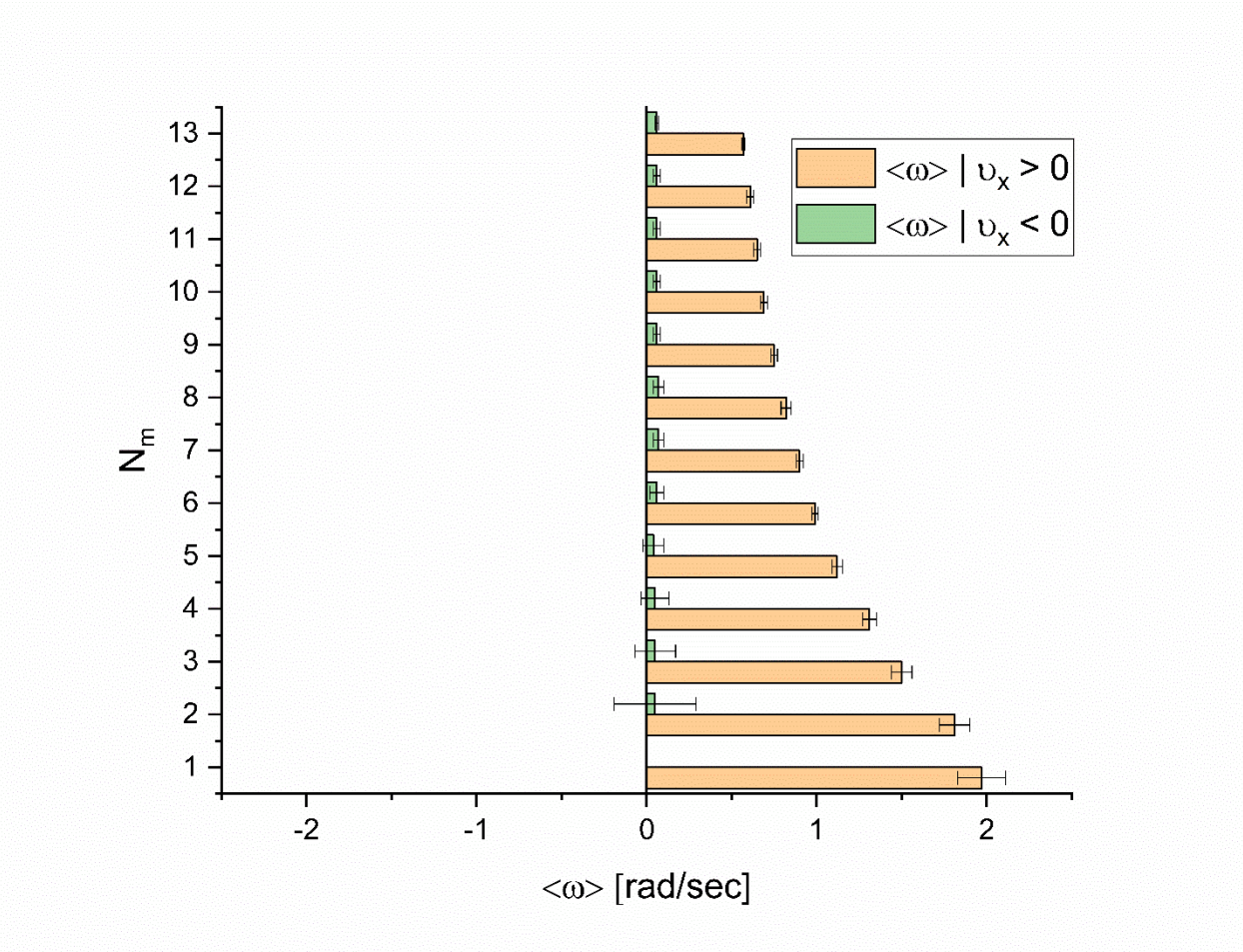

Fig. S10.3 – Mean instantaneous longitudinal velocity, $\langle v_x \rangle$, separated for anterograde, $v_x > 0$, and retrograde, $v_x < 0$, directions for the different (R, N_m) configurations for time intervals equal 0.27s.

N_m	1	2	3	4	5	6	7
$\langle\omega\rangle \mid v_x > 0$	1.97 $\pm$ 0.14	1.81 $\pm$ 0.09	1.50 $\pm$ 0.06	1.31 $\pm$ 0.04	1.12 $\pm$ 0.03	0.99 $\pm$ 0.02	0.90 $\pm$ 0.02
$\langle\omega\rangle \mid v_x < 0$	N/A	0.05 $\pm$ 0.24	0.05 $\pm$ 0.12	0.05 $\pm$ 0.08	0.04 $\pm$ 0.06	0.06 $\pm$ 0.04	0.07 $\pm$ 0.03
N_m	8	9	10	11	12	13	
$\langle\omega\rangle \mid v_x > 0$	0.82 $\pm$ 0.01	0.75 $\pm$ 0.01	0.69 $\pm$ 0.01	0.65 $\pm$ 0.01	0.61 $\pm$ 0.01	0.57 $\pm$ 0.01	
$\langle\omega\rangle \mid v_x < 0$	0.07 $\pm$ 0.03	0.06 $\pm$ 0.02	0.06 $\pm$ 0.02	0.06 $\pm$ 0.02	0.06 $\pm$ 0.02	0.06 $\pm$ 0.01	

Table. S10.4 – Mean instantaneous longitudinal velocity, $\langle v_x \rangle$, separated for anterograde, $v_x > 0$, and retrograde, $v_x < 0$, directions for the different (R, N_m) configurations for time intervals equal 0.27s ($mean \pm SEM$).

SI. 11 Theoretical raw data for Δt = MC Step Time

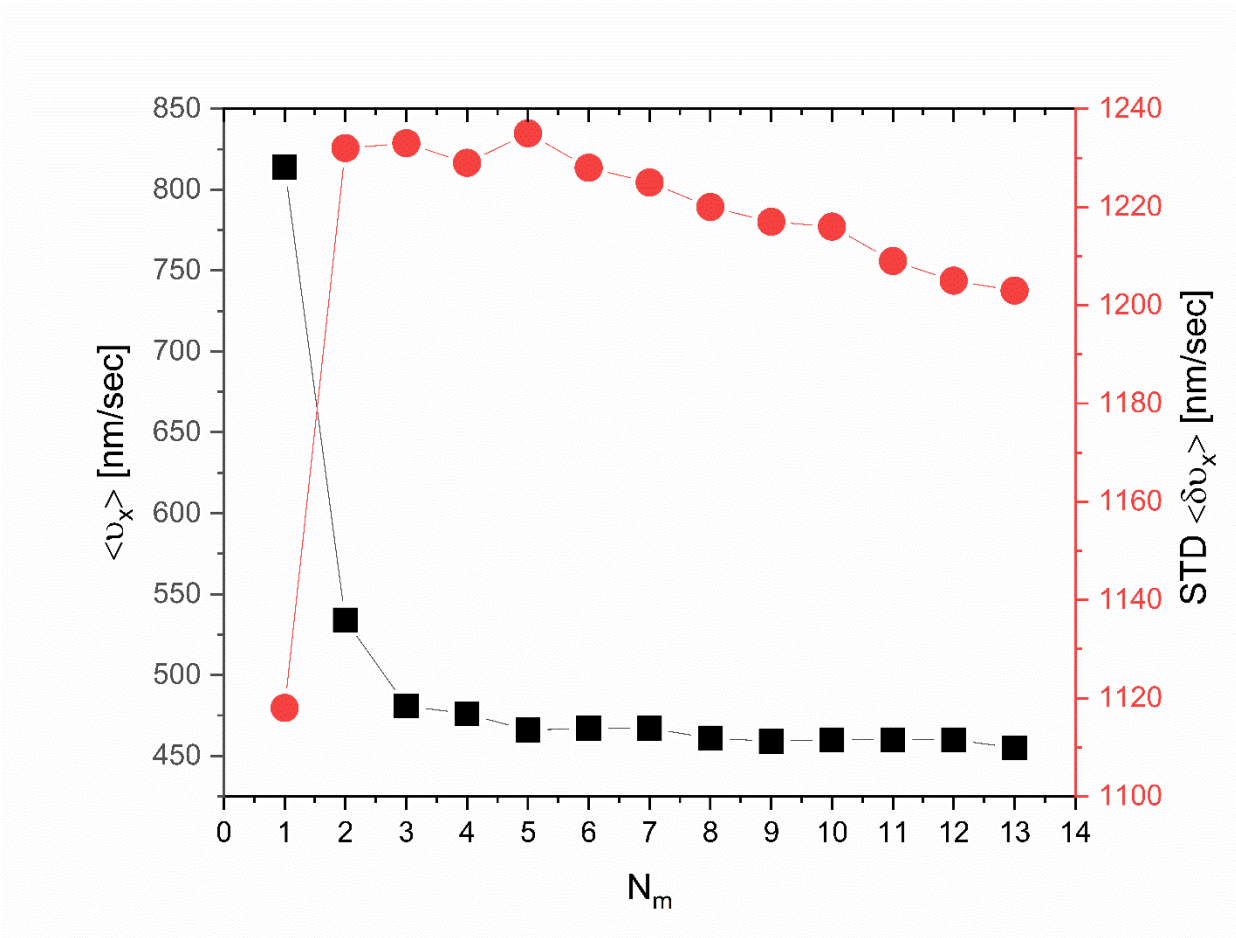

Fig. S11.1 – Mean longitudinal velocity, $\langle v_x \rangle$, and STD, $\langle \delta v_x \rangle$, of the different (R, N_m) configurations for time intervals equal to MC step times.

N_m	1	2	3	4	5	6	7
$\langle v_x \rangle$	814 ± 4	534 ± 4	481 ± 2	458 ± 2	466 ± 2	467 ± 2	467 ± 2
$\langle \delta v_x \rangle$	1188	1232	1233	1227	1235	1228	1225
N_m	8	9	10	11	12	13	
$\langle v_x \rangle$	461 ± 1	459 ± 1	460 ± 1	454 ± 2	451 ± 1	452 ± 1	
$\langle \delta v_x \rangle$	1220	1217	1216	1208	1203	1202	

Table. S11.1 – Mean longitudinal velocity, $\langle v_x \rangle$, and STD, $\langle \delta v_x \rangle$, of the different (R, N_m) configurations for time intervals equal to MC step times (mean $\pm$ SEM).

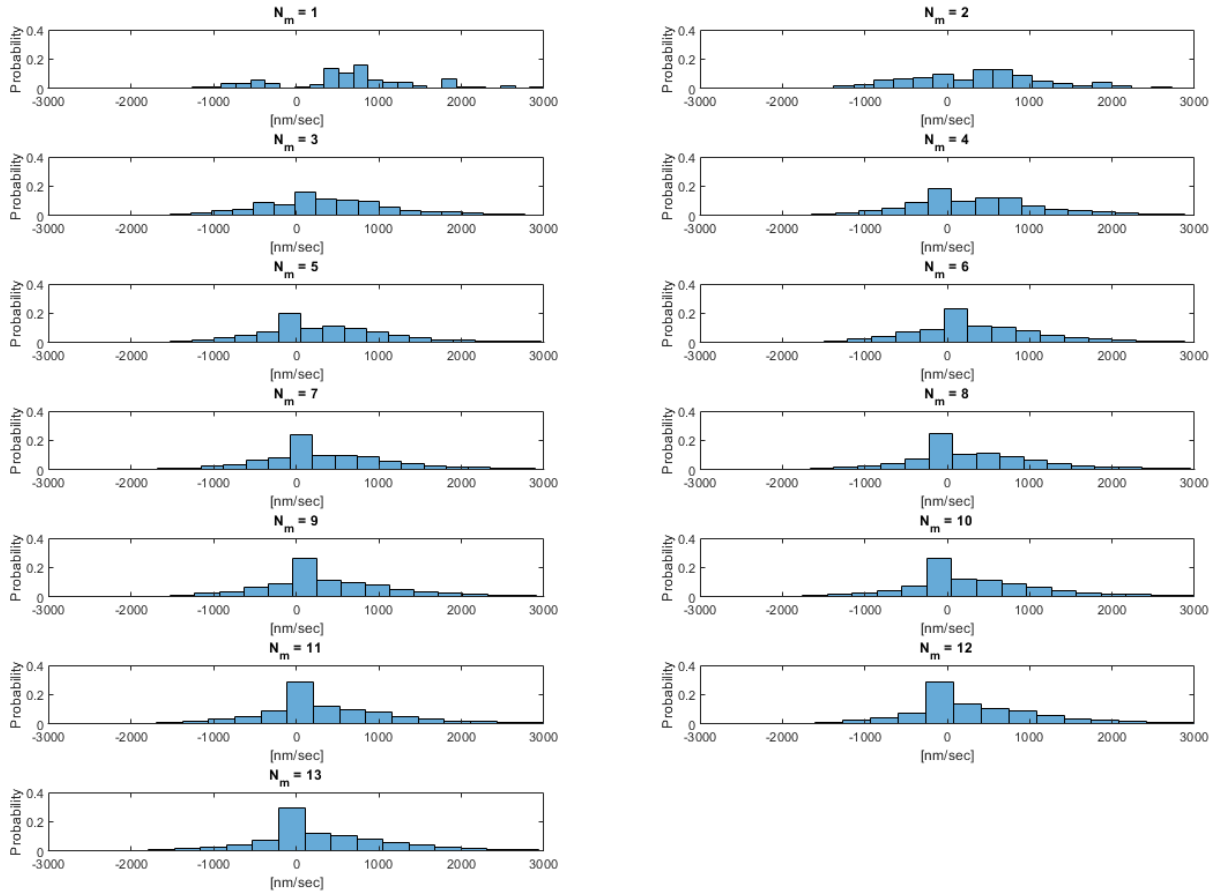

Fig. S11.2 – Distributions of the longitudinal velocity, υ_x, for the different (R, N_m) configurations for time intervals equal to MC step times. The above histograms include all velocity values, <u>including</u> cases where the NPs remain stagnant for short periods.

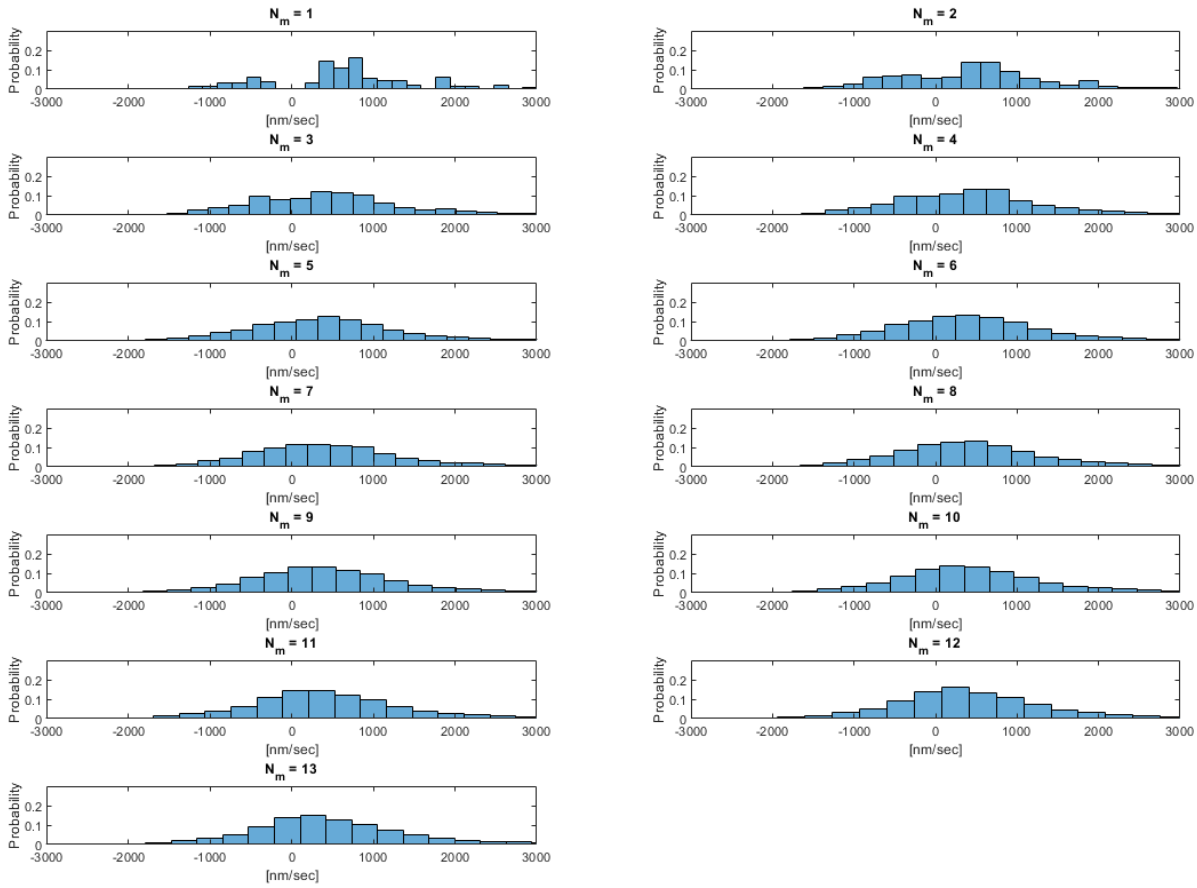

Fig. S11.3 – Distributions of the longitudinal velocity, v_x, for the different (R, N_m) configurations for time intervals equal to MC step times. The above histograms include most velocity values, <u>excluding</u> cases where the NPs remain stagnant for short periods.

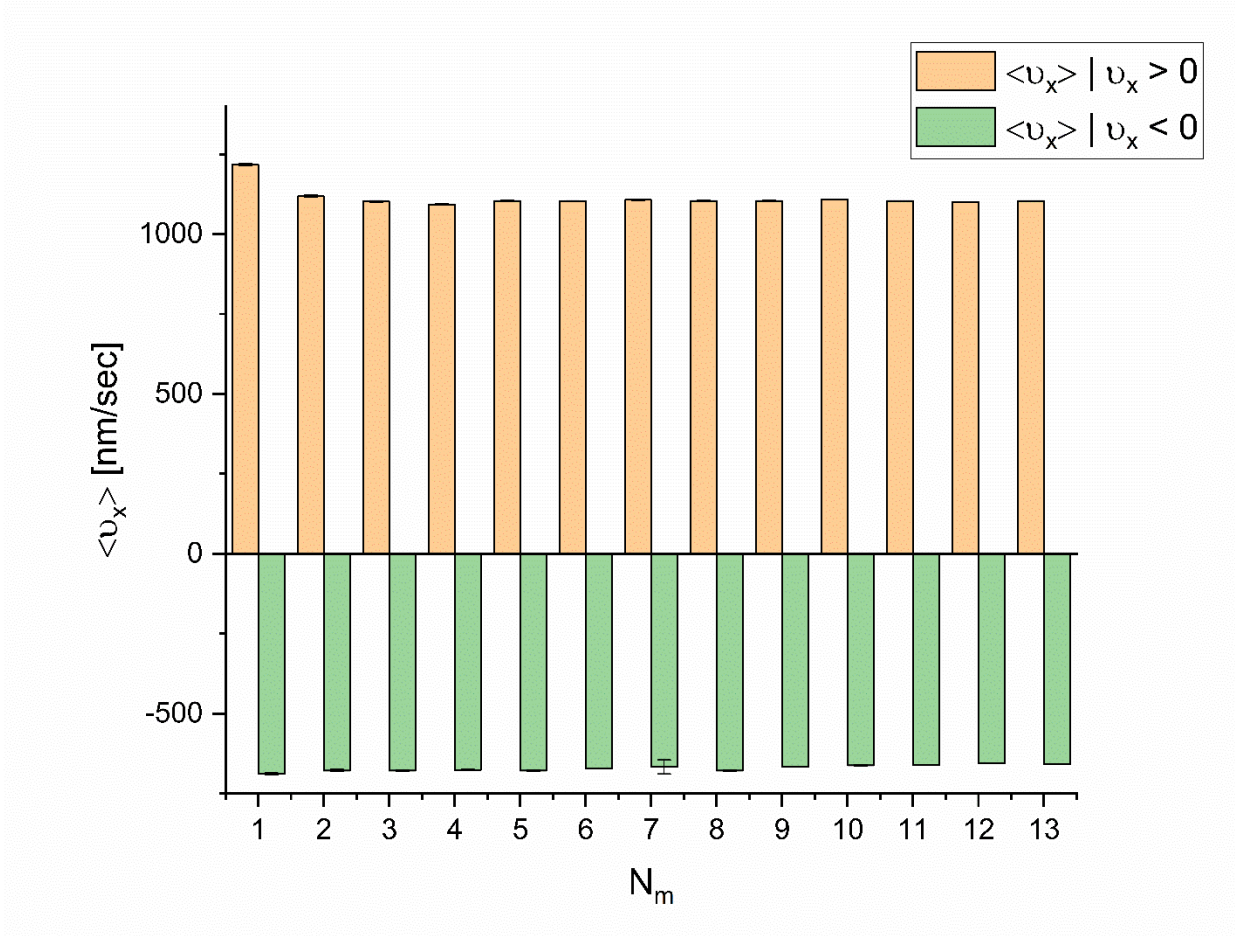

Fig. S11.4 – Mean instantaneous longitudinal velocity, $\langle v_x \rangle$, separated for anterograde, $v_x > 0$, and retrograde, $v_x < 0$, directions for the different (R, N_m) configurations for time intervals equal to MC step times.

N_m	1	2	3	4	5	6	7
$\langle v_x \rangle \mid v_x > 0$	1217 ± 4	1118 ± 4	1102 ± 3	1093 ± 2	1104 ± 2	1103 ± 2	1107 ± 2
$\langle v_x \rangle \mid v_x < 0$	-668 ± 3	-678 ± 4	-678 ± 3	-676 ± 2	-678 ± 2	-671 ± 2	-666 ± 2
N_m	8	9	10	11	12	13	
$\langle v_x \rangle \mid v_x > 0$	1104 ± 2	1104 ± 2	1108 ± 2	1104 ± 1	1101 ± 1	1104 ± 1	
$\langle v_x \rangle \mid v_x < 0$	-678 ± 2	-666 ± 2	-662 ± 2	-661 ± 1	-655+-1	-657 ± 1	

Table. 11.2 – Mean instantaneous longitudinal velocity, $\langle v_x \rangle$, separated for anterograde, $v_x > 0$, and retrograde, $v_x < 0$, directions for the different (R, N_m) configurations (mean $\pm$ SEM).

N_m	1	2	3	4	5	6	7
$\langle\lambda\rangle$	823 ± 27	798 ± 27	935 ± 33	1132 ± 40	1474 ± 52	1528 ± 50	1677 ± 56
$\langle\tau_p\rangle$	1 ± 0.03	1.16 ± 0.04	1.65 ± 0.06	2.14 ± 0.08	2.82 ± 0.1	2.95 ± 0.1	3.28 ± 0.11
N_m	8	9	10	11	12	13	
$\langle\lambda\rangle$	2037 ± 69	2119 ± 71	2434 ± 79	2592 ± 87	2797 ± 91	3123 ± 102	
$\langle\tau_p\rangle$	4.07 ± 0.14	4.28 ± 0.14	4.93 ± 0.16	5.33 ± 0.18	5.81 ± 0.19	6.49 ± 0.21	

Table. S11.3 – Mean longitudinal run-lengths (along the MT symmetry axis), $\langle\lambda\rangle$, and processivity times, $\langle\tau_p\rangle$, directions for the different (R, N_m) configurations for time intervals equal to MC step times (mean $\pm$ SEM).

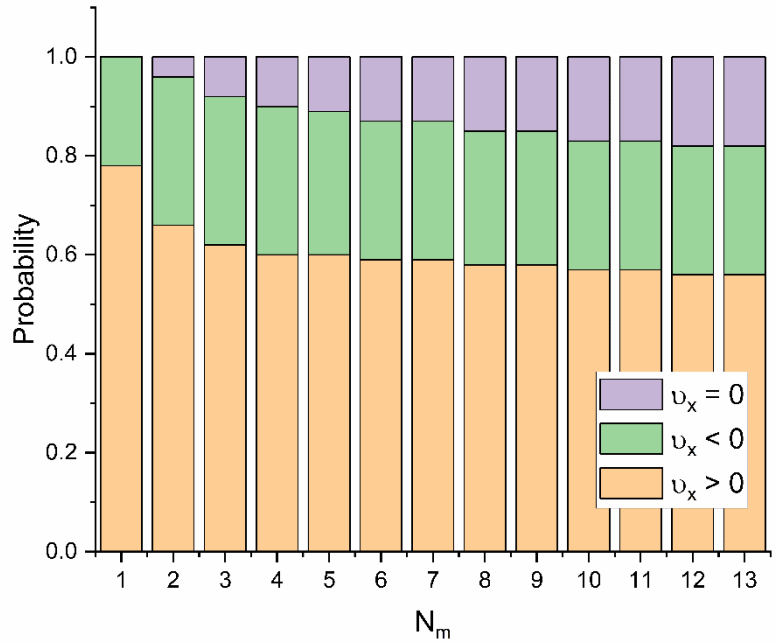

Fig. S11.5 – Fraction of anterograde ($\upsilon_x > 0$), retrograde ($\upsilon_x < 0$), and vanishing ($\upsilon_x = 0$) velocities of the (R=20 nm, N_M= 1,2…13) NP configurations for time intervals equal to MC step times. For each configuration, the velocity fractions are calculated by considering all the trajectories together as if they were combined to create a single, very long trajectory.

N_m	1	2	3	4	5	6	7
$\upsilon_x > 0$	0.78	0.66	0.62	0.60	0.60	0.59	0.59
$\upsilon_x < 0$	0.22	0.30	0.30	0.30	0.29	0.28	0.28
$\upsilon_x = 0$	0.00	0.04	0.08	0.10	0.11	0.13	0.13
N_m	8	9	10	11	12	13	
$\upsilon_x > 0$	0.58	0.58	0.57	0.57	0.56	0.56	
$\upsilon_x < 0$	0.27	0.27	0.26	0.26	0.26	0.26	
$\upsilon_x = 0$	0.15	0.15	0.16	0.17	0.18	0.18	

Table. 11.4 – Fraction of anterograde ($\upsilon_x > 0$), retrograde ($\upsilon_x < 0$), and vanishing ($\upsilon_x = 0$) velocities of the (R=20 nm, N_M= 1,2…13) NP configurations for time intervals equal to MC step times. For each configuration, the velocity fractions are calculated by considering all the trajectories together as if they were combined to create a single, very long trajectory.

N_m	1	2	3	4	5	6	7
$\langle M_B \rangle$	1	1.38	1.63	1.73	1.81	1.85	1.94
$\langle \delta M_B \rangle$	0	0.4883	0.5142	0.5123	0.5075	0.5110	0.5107
N_m	8	9	10	11	12	13	
$\langle M_B \rangle$	1.94	1.97	2.01	2.04	2.07	2.09	
$\langle \delta M_B \rangle$	0.5174	0.5280	0.5363	0.5459	0.5590	0.5638	

Table. S11.5 – Mean number and STD of transient MT-bounded motors, M_B, for the different (R, N_m) configurations for time intervals equal to MC step times (see Fig. 9A in the manuscript).

N_m	1	2	3	4	5	6	7
$\langle v_{x,M_B=1} \rangle$	813 ± 6	819 ± 9	826 ± 10	808 ± 8	822 ± 9	819 ± 9	811 ± 8
$\langle v_{x,M_B=2} \rangle$	N/A	154 ± 10	286 ± 8	358 ± 7	395 ± 6	409 ± 5	428 ± 5
$\langle v_{x,M_B=3} \rangle$	N/A	N/A	148 ± 58	168 ± 18	185 ± 9	204 ± 8	219 ± 7
$\langle v_{x,M_B=4} \rangle$	N/A	N/A	N/A	75 ± 30	142 ± 37	101 ± 25	143 ± 28
$\langle v_{x,M_B=5} \rangle$	N/A	N/A	N/A	N/A	0	0	0
N_m	8	9	10	11	12	13	
$\langle v_{x,M_B=1} \rangle$	818 ± 9	812 ± 8	821 ± 8	804 ± 7	818 ± 8	814 ± 9	
$\langle v_{x,M_B=2} \rangle$	445 ± 6	450 ± 5	456 ± 4	457 ± 4	460 ± 4	466 ± 4	
$\langle v_{x,M_B=3} \rangle$	236 ± 7	244 ± 6	241 ± 6	248 ± 5	242 ± 4	255 ± 5	
$\langle v_{x,M_B=4} \rangle$	126 ± 19	108 ± 13	114 ± 12	148 ± 14	128 ± 9	129 ± 7	
$\langle v_{x,M_B=5} \rangle$	0	-37 ± 15	54 ± 51	6 ± 26	59 ± 18	60 ± 16	

Table S11.6 – Mean longitudinal velocity of the different NP states, where a state is defined according to the number of MT bounded motors, M_B, for the different (R, N_m) configurations for time intervals equal to MC step times (mean $\pm$ SEM; see Fig. 9B in the manuscript).

N_M	1	2	3	4	5	6	7
$\langle \delta v_{x,M_B=1} \rangle$	0	296	321	251	284	252	256
$\langle \delta v_{x,M_B=2} \rangle$	N/A	163	227	205	188	169	158
$\langle \delta v_{x,M_B=3} \rangle$	N/A	N/A	487	239	206	211	201
$\langle \delta v_{x,M_B=4} \rangle$	N/A	N/A	N/A	60	150	157	255
$\langle \delta v_{x,M_B=5} \rangle$	N/A	N/A	N/A	N/A	N/A	N/A	N/A

N_M	8	9	10	11	12	13
$\langle \delta v_{x,M_B=1} \rangle$	285	247	254	234	256	293
$\langle \delta v_{x,M_B=2} \rangle$	178	144	121	123	120	121
$\langle \delta v_{x,M_B=3} \rangle$	214	179	188	145	123	157
$\langle \delta v_{x,M_B=4} \rangle$	217	198	226	189	177	169
$\langle \delta v_{x,M_B=5} \rangle$	N/A	N/A	141	58	80	96

Table S11.7 – longitudinal velocity STD of the different NP states, where a state is defined according to the number of MT bounded motors, M_B, for the different (R, N_m) configurations for time intervals equal to MC step times (see Fig. 9B in the manuscript).

N_m / State	1	2	3	4	5	6	7
$M_B = 1$	1	0.83	0.53	0.44	0.34	0.29	0.26
$M_B = 2$	0	0.17	0.46	0.54	0.62	0.65	0.67
$M_B = 3$	0	0	0.01	0.02	0.04	0.06	0.07
$M_B = 4$	0	0	0	< 0.01	< 0.01	< 0.01	< 0.01
$M_B = 5$	0	0	0	0	< 0.01	< 0.01	< 0.01
	8	9	10	11	12	13	
$M_B = 1$	0.23	0.21	0.18	0.17	0.15	0.14	
$M_B = 2$	0.69	0.70	0.71	0.72	0.72	0.72	
$M_B = 3$	0.08	0.09	0.10	0.10	0.12	0.13	
$M_B = 4$	< 0.01	< 0.01	0.01	0.01	0.01	0.01	

Table S11.8 – Time fraction of the different NP states, where a state is defined according to the number of MT bounded motors, M_B, for the different (R, N_m) configurations for time intervals equal to MC step times (see Fig. 9C in the manuscript).

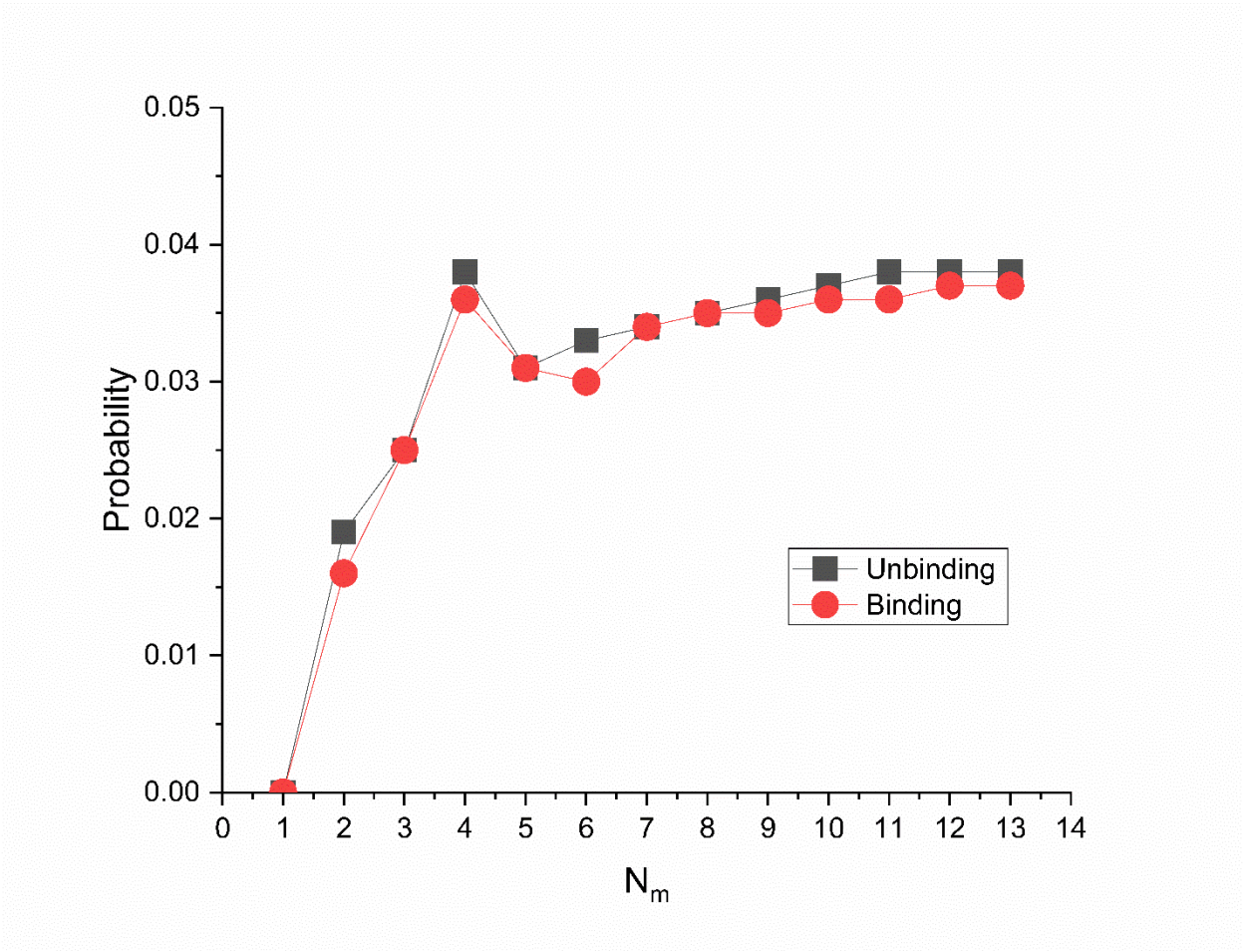

Fig. S11.6 – Fraction of binding and unbinding events out of the total possible events for the different (R, N_m) configurations for time intervals equal to MC step times.

N_m	1	2	3	4	5	6	7
$F_{\text{unbinding}}$	<0.01	0.019	0.025	0.032	0.031	0.033	0.034
F_{binding}	<0.01	0.016	0.025	0.029	0.031	0.03	0.034
N_m	8	9	10	11	12	13	
$F_{\text{unbinding}}$	0.035	0.036	0.037	0.038	0.038	0.038	
F_{binding}	0.035	0.035	0.036	0.036	0.037	0.037	

Table. S11.9 – Fraction of binding and unbinding events out of the total possible events for the different (R, N_m) configurations for time intervals equal to MC step times.

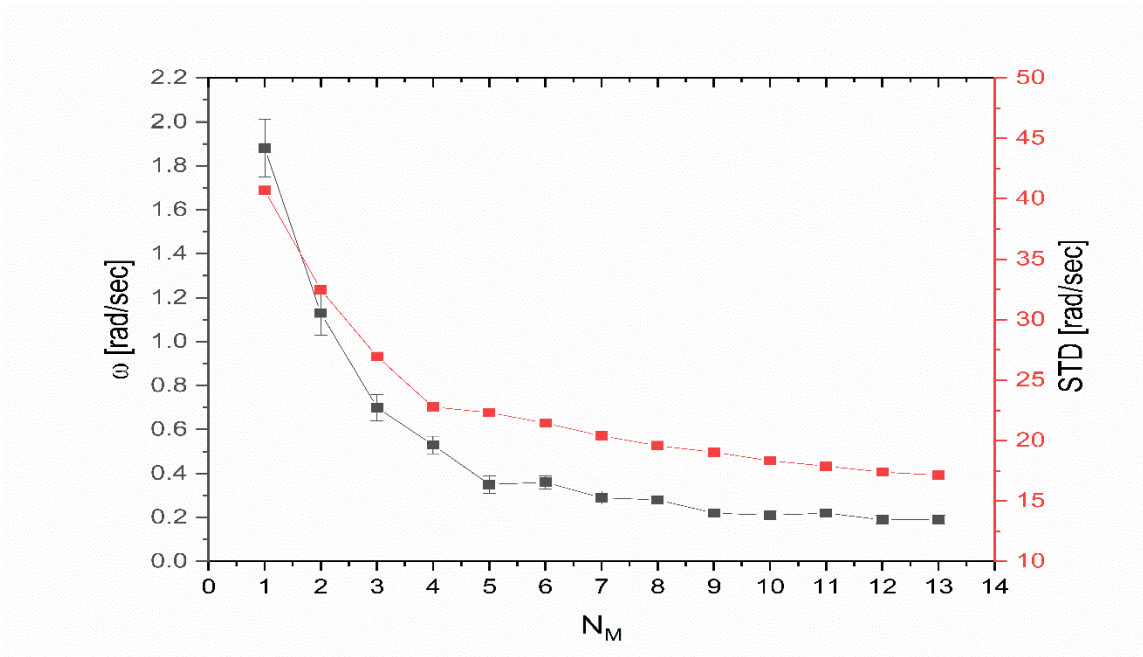

Fig. S11.7 – Mean angular velocity, $\langle\omega\rangle$, and STD, $\langle\delta\omega\rangle$, of the different (R, N_m) configurations for time intervals equal to MC step times.

N_m	1	2	3	4	5	6	7
$\langle\omega\rangle$	1.88 $\pm$ 0.13	1.13 $\pm$ 0.1	0.70 $\pm$ 0.06	0.53 $\pm$ 0.04	0.35 $\pm$ 0.04	0.36 $\pm$ 0.03	0.29 $\pm$ 0.03
$\langle\delta\omega\rangle$	40.69	32.47	26.95	22.78	22.31	21.45	20.39
N_m	8	9	10	11	12	13	
$\langle\omega\rangle$	0.28 $\pm$ 0.02	0.22 $\pm$ 0.02	0.21 $\pm$ 0.02	0.22 $\pm$ 0.02	0.19 $\pm$ 0.02	0.19 $\pm$ 0.02	
$\langle\delta\omega\rangle$	19.58	19.04	18.33	17.88	17.40	17.14	

Table. S11.10 – Mean angular velocity, $\langle\omega\rangle$, and STD, $\langle\delta\omega\rangle$, of the different (R, N_m) configurations for time intervals equal to MC step times (mean $\pm$ SEM).

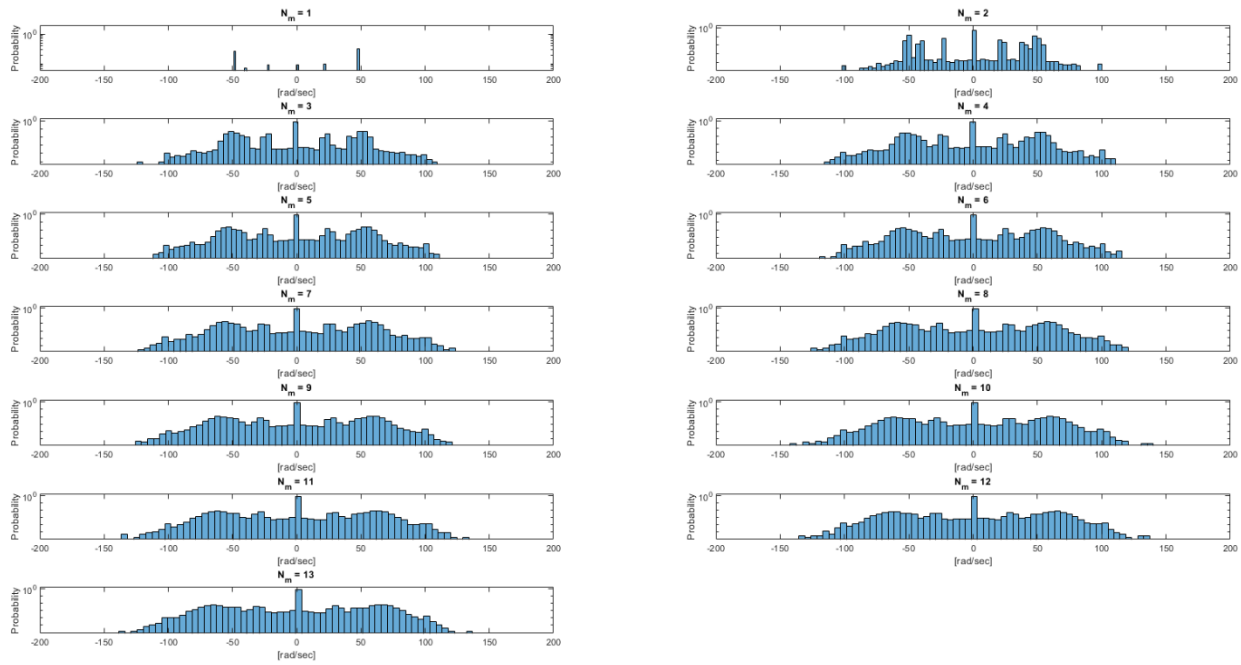

Fig. S11.8 – Distributions of the Angular velocity, ω, for the different (R, N_m) configurations for time intervals equal to MC step times.

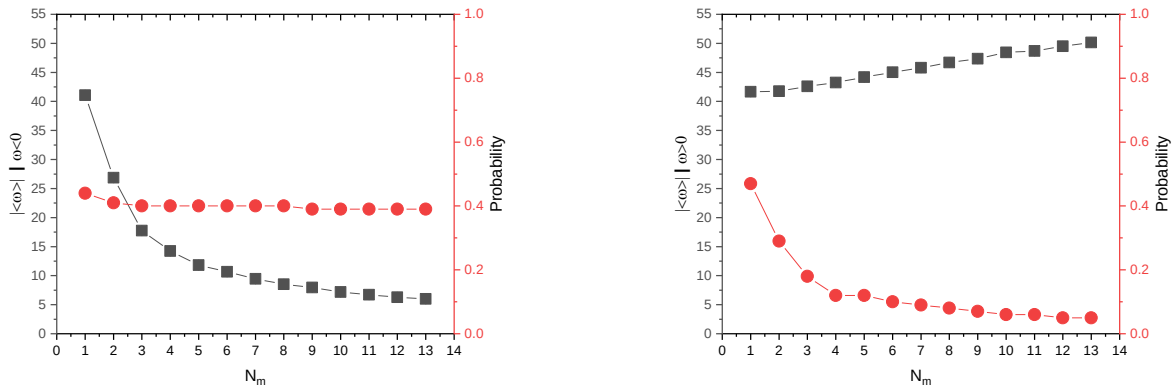

Fig. S11.9 – Instantaneous absolute angular velocity segregated to Left-handed and right-handed components of the distinct (R=20 nm, N_M= 1,2…13) NPs for time intervals equal to MC step times. The separated mean angular velocities are marked by black lines and squares. Also, we show the probabilities for left- or right-handed motion (red line and squares) (A) Left-handed velocity, $|\langle\omega_L\rangle| = |\langle\omega\rangle| \mid \omega < 0$, and probability for left-handed motion. (B) Right-handed velocity, $|\langle\omega_R\rangle| = |\langle\omega\rangle| \mid \omega < 0$, and probability for right-handed motion.

N_m	1	2	3	4	5	6	7
$\langle\omega_L\rangle$	-41.07 ± 0.05	-26.86 ± 0.1	-17.74 ± 0.07	-14.24 ± 0.06	-11.83 ± 0.05	-10.67 ± 0.05	-9.46 ± 0.04
$\langle\omega_R\rangle$	41.66 ± 0.05	41.76 ± 0.08	42.59 ± 0.07	43.25 ± 0.07	44.18 ± 0.07	45.02 ± 0.08	45.79 ± 0.08
N_m	8	9	10	11	12	13	
$\langle\omega_L\rangle$	-8.52 ± 0.04	-7.97 ± 0.04	-7.18 ± 0.03	-6.71 ± 0.03	-6.29 ± 0.03	-5.99 ± 0.03	
$\langle\omega_R\rangle$	46.7 ± 0.08	47.34 ± 0.09	48.44 ± 0.09	48.70 ± 0.09	49.50 ± 0.09	50.15 ± 0.09	

Table. S11.11 – Instantaneous absolute angular velocity segregated to Left-handed and right-handed components of the distinct (R=20 nm, N_M= 1,2…13) NPs for time intervals equal to MC step times (mean $\pm$ SEM).

N_m	1	2	3	4	5	6	7
$\langle\omega\rangle \mid \upsilon_x > 0$	0.6 $\pm$ 0.15	0.5 $\pm$ 0.14	0.3 $\pm$ 0.08	0.024 $\pm$ 0.06	0.03 $\pm$ 0.05	0.14 $\pm$ 0.04	0.07 $\pm$ 0.04
$\langle\omega\rangle \mid \upsilon_x < 0$	6.8 $\pm$ 0.29	2.6 $\pm$ 0.15	1.64 $\pm$ 0.08	1.3 $\pm$ 0.07	1.16 $\pm$ 0.05	0.99 $\pm$ 0.05	0.92 $\pm$ 0.05
N_m	8	9	10	11	12	13	
$\langle\omega\rangle \mid \upsilon_x > 0$	0.09 $\pm$ 0.03	0.005 $\pm$ 0.03	0.07 $\pm$ 0.03	0.09 $\pm$ 0.03	0.06 $\pm$ 0.03	0.08 $\pm$ 0.02	
$\langle\omega\rangle \mid \upsilon_x < 0$	0.83 $\pm$ 0.04	0.8 $\pm$ 0.04	0.66 $\pm$ 0.04	0.65 $\pm$ 0.03	0.60 $\pm$ 0.03	0.56 $\pm$ 0.03	

Table. S11.12 – Instantaneous absolute angular velocity segregated to anterograde, $\langle\omega\rangle \mid \upsilon_x > 0$, and retrograde, $\langle\omega\rangle \mid \upsilon_x < 0$, motions for the distinct (R=20 nm, N_M= 1,2…13) NPs for time intervals equal to MC step times (mean $\pm$ SEM).

N_m	1	2	3	4	5	6	7
$\langle H \rangle$	825 ± 29	832 ± 38	1032 ± 40	1176 ± 46	1503 ± 55	1619 ± 62	1689 ± 68
$\langle \delta H \rangle$	548	570	695	815	1041	1092	1228
F_H	0.25	0.23	0.22	0.22	0.27	0.24	0.24
P_{LH}	0.18	0.24	0.2	0.2	0.25	0.24	0.24
P_{RH}	0.82	0.76	0.80	0.8	0.75	0.76	0.76
N_m	8	9	10	11	12	13	
$\langle H \rangle$	2061 ± 81	2124 ± 80	2533 ± 108	2588 ± 102	2792 ± 116	3091 ± 118	
$\langle \delta H \rangle$	1565	1470	1987	1956	2152	2320	
F_H	0.28	0.26	0.25	0.27	0.25	0.28	
P_{LH}	0.24	0.23	0.22	0.22	0.26	0.23	
P_{RH}	0.76	0.77	0.78	0.78	0.64	0.77	

Table S11.13 – Analysis of the actual NP helical motion from observed (simulated) trajectories, where $\langle H \rangle$ is the mean helical pitch size (mean $\pm$ SEM), $\langle \delta H \rangle$ is the helical pitch size STD, F_H is the fraction of NP trajectories that completed at least one wind around the MT symmetry axis out of the total number of trajectories, P_{LH} is the probability for a left-handed helical motion, and P_{RH} is the probability of a right-handed helical motion. The mean pitch size is calculated by averaging over all the helical pitches of the same (R, N_m) configuration, regardless of their direction (i.e., $\phi = +2\pi$ or, i.e., $\phi = -2\pi$). A helical pitch size equals to the NP accumulated longitudinal motion – towards the MT minus-end – up to the point when a wind around the MT is completed (i.e., $\phi = \pm 2\pi$). Note that the motion does not have to be consistent towards either left-handed or right-handed direction, e.g., a right-handed helix can contain left-handed motion ($\Delta\phi < 0$) and *vice versa*, or in other words, the large transverse fluctuations do not reset the $\phi = \sum \Delta\phi$ count towards a wind completion ($\pm 2\pi$).

N_m	1	2	3	4	5	6	7
$\langle H_L \rangle$	993 ± 97	857 ± 79	1201 ± 106	1185 ± 72	1383 ± 96	1794 ± 133	1746 ± 173
$\langle H_R \rangle$	789 ± 28	824 ± 44	992 ± 42	1173 ± 55	1542 ± 65	1565 ± 70	1671 ± 71
N_m	8	9	10	11	12	13	
$\langle H_L \rangle$	2173 ± 169	2034 ± 183	2383 ± 239	2541 ± 191	2825 ± 237	3169 ± 245	
$\langle H_R \rangle$	2026 ± 92	2151 ± 89	2575 ± 120	2602 ± 119	2780 ± 133	3068 ± 134	

Table S11.14 – Analysis of the actual NP helical motion from observed (simulated) trajectories separated to the left- and right- handed motions (mean $\pm$ SEM). $\langle H_L \rangle$ is the mean helical pitch size for left-handed helices (i.e., $\phi = -2\pi$), and $\langle H_R \rangle$ is the mean helical pitch size for right-handed helices (i.e., $\phi = +2\pi$).

N_m	1	2	3	4	5	6	7
$\langle H \rangle$	825 ± 29	832 ± 38	1032 ± 40	1176 ± 46	1503 ± 55	1619 ± 62	1689 ± 68
$\langle \bar{H} \rangle$	2718 ± 192	2965 ± 265	4344 ± 278	5383 ± 321	8299 ± 544	8035 ± 467	9936 ± 597
N_m	8	9	10	11	12	13	
$\langle H \rangle$	2061 ± 81	2124 ± 80	2533 ± 108	2588 ± 102	2792 ± 116	3091 ± 118	
$\langle \bar{H} \rangle$	10298 ± 554	13045 ± 812	13585 ± 837	12699 ± 696	14967 ± 856	15208 ± 837	

Table S11.15 – Helical pitch size estimated using the mean values of angular and longitudinal velocities, $\langle \bar{H} \rangle = |\frac{2\pi}{\langle \omega \rangle} \langle v_x \rangle|$ (mean $\pm$ error).

SI. 12 Binomial Parameters Estimation

Consider, first, the issue of the number of MT bound motors. The experiment involves adsorption of dynein motors to the NP-PEG-NLS complex, resulting with a fluctuating number of motors between NPs, whose average is constrained by the mean ξ *vis* $\xi = \sqrt{4\pi}\,\mathrm{R}/\sqrt{\langle \mathrm{N_m} \rangle}$. Likewise, we may define the mean variable as the mean surface relative coverage $\theta = \left(\frac{\xi^*}{\xi}\right)^2$. In order to account for these fluctuations, we assume independent site (i.e., PEG-NLS) adsorption with probability θ for adsorption (per site), suggesting the bound motor number distributions is the well-known binomial distribution

$$P(N_m; \theta, N) = \frac{N!}{N_m!\,(N - N_m)!}\,\theta^{N_m}(1-\theta)^{N-N_m}$$

consistent with the mean number of motors obeying $\langle \mathrm{N_m} \rangle = N\theta$.

Yet, since only NPs with $N_m \geq 1$ can bind to the MT, by assumption, we require the conditional probability distribution $P^*(N_m; \theta, N) \equiv (P(N_m; \theta, N|\, N_m \geq 1)$, which is given by

$$P^*(N_m; \theta, N) = \frac{P(N_m; \theta, N)}{1 - (1-\theta)^N}$$

The mean number of motors in those NPs with $N_m \geq 1$ is therefore

$$\langle \mathrm{N_m} \rangle^* = \frac{N\theta}{1 - (1-\theta)^N} = \frac{\langle \mathrm{N_m} \rangle}{1 - (1 - \langle \mathrm{N_m} \rangle / N)^N}$$

Given a value of θ, we can compute the mean motility parameters of the NP ensemble associate with this value of θ, i.e. for a motility variable (i.e., velocities, run-times, etc.) $f(N_m)$, the associated mean is given by

$$\langle f(N_M) \rangle = \sum_{N_m=0}^{N} f(N_m) P^*(N_m; \theta, N)$$

To adjust the binomial distribution to the experimental setup, we used N values that correspond to the estimated value of ξ^* of the most diluted systems: A0, A1, and A2, which have shown to be in agreement with simulation results. For system A0, N is estimated to be ~5, and for systems A1

and A2, $N \cong 10$. Using these N values, we examine the mean motility parameters corresponding to θ values ranging from 0.1 to 1.

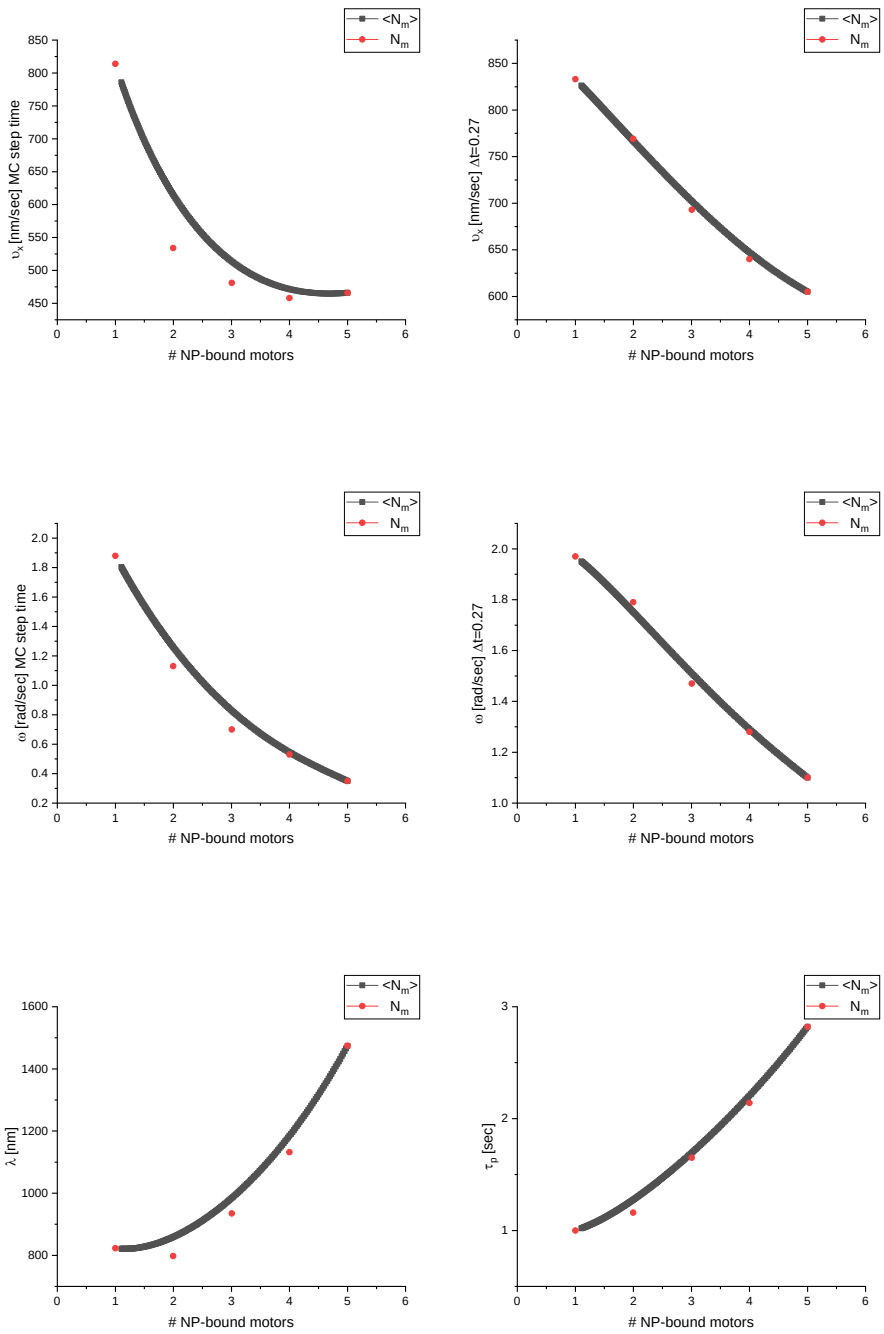

Fig S12.1 –Parameters estimation derived using the binomial coverage probabilities for $N = 5$. Red dots denote the value of the parameter for a deterministic number of NP-bound motors, N_m, such that all the particles have the exact same fixed N_m . Black lines denote the value of the parameter for a mean number of NP-bounded motors, $\langle N_m \rangle$, such that the value of N_m varies between NPs **(A)** Longitudinal velocity, υ_x, for MC step time. (**B**) Longitudinal velocity, υ_x, for 0.27s. interval. **(C)** Angular velocity, ω, for MC step time. (**D**) Angular velocity, ω, for 0.27s. interval. (**E**) Longitudinal run-length, λ. (**F**) processivity time, τ_p.

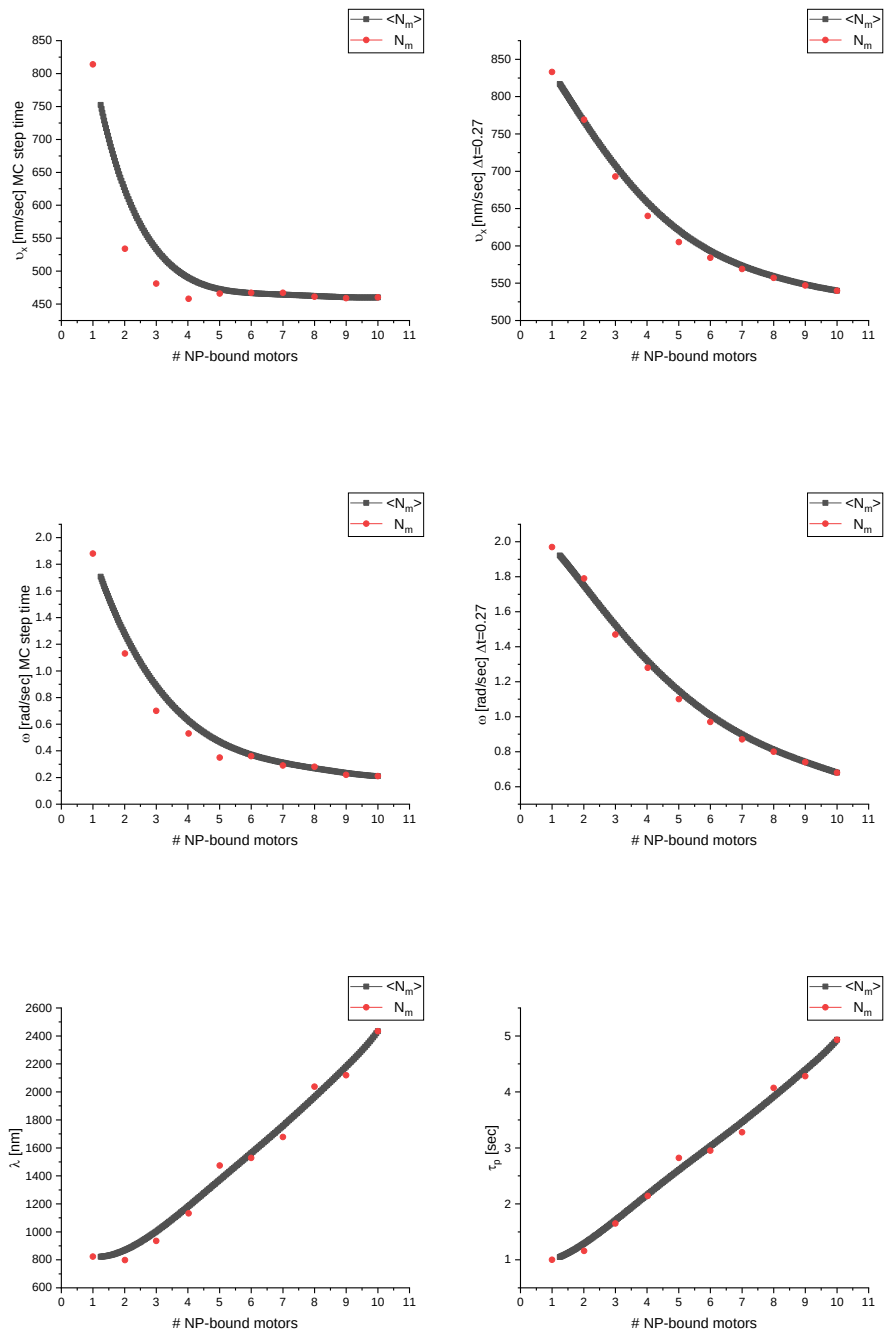

Fig S12.2 –Parameters estimation derived using the binomial coverage probabilities for $N = 10$. Red dots denote the value of the parameter for a deterministic number of NP-bound motors, N_m, such that all the particles have the exact same fixed N_m . Black lines denote the value of the parameter for a mean number of NP-bounded motors, $\langle N_m \rangle$, such that the value of N_m varies between NPs **(A)** Longitudinal velocity, υ_x, for MC step time. (**B**) Longitudinal velocity, υ_x, for 0.27s. interval. **(C)** Angular velocity, ω, for MC step time. (**D**) Angular velocity, ω, for 0.27s. interval. (**E**) Longitudinal run-length, λ. (**F**) processivity time, τ_p.

SI-Movies

In the attached movies (1-4), we show selected trajectories for four NP configurations: (i) **S.Movie 1** depicts the motion of a NP with a single NP-anchored motor ($N_m = 1$), (ii) **S.Movie 2** depicts the motion of a NP with three NP-anchored motor ($N_m = 3$), (iii) **S.Movie 3** depicts the motion of a NP with seven NP-anchored motor ($N_m = 7$), and (iv) **S.Movie 4** depicts the motion of a NP with 13 NP-anchored motor ($N_m = 13$).

SI References

1. Danino D, Bernheim-Groswasser A, & Talmon Y (2001) Digital cryogenic transmission electron microscopy: an advanced tool for direct imaging of complex fluids. *Colloids and Surfaces A: Physicochemical and Engineering Aspects* 183:113-122.
2. Rosano C, Arosio P, & Bolognesi M (1999) The X-ray three-dimensional structure of avidin. *Biomolecular Engineering* 16(1-4):5-12.
3. Israelachvili JN (2011) *Intermolecular and surface forces* (Academic press).
4. De Gennes P (1988) Model polymers at interfaces. *Physical basis of cell-cell adhesion*, (CRC Press Boca Raton, FL), pp 39-60.
5. Delgado ÁV, González-Caballero F, Hunter R, Koopal L, & Lyklema J (2007) Measurement and interpretation of electrokinetic phenomena. *Journal of colloid and interface science* 309(2):194-224.
6. Oesterhelt F, Rief M, & Gaub H (1999) Single molecule force spectroscopy by AFM indicates helical structure of poly (ethylene-glycol) in water. *New Journal of Physics* 1(1):6.
7. De Gennes P-G & Gennes P-G (1979) *Scaling concepts in polymer physics* (Cornell university press).
8. Doi M & Edwards SF (1988) *The theory of polymer dynamics* (oxford university press).
9. Rubinstein M & Colby RH (2003) *Polymer physics* (Oxford university press New York).
10. Lee H, Venable RM, MacKerell Jr AD, & Pastor RW (2008) Molecular dynamics studies of polyethylene oxide and polyethylene glycol: hydrodynamic radius and shape anisotropy. *Biophysical journal* 95(4):1590-1599.
11. Kienberger F, *et al.* (2000) Static and dynamical properties of single poly (ethylene glycol) molecules investigated by force spectroscopy. *Single Molecules* 1(2):123-128.
12. Dobrinski H, Wilkens M, Benecke W, & Binder J (2000) Flexible microfluidic-device-stamp-system with integrated electrical sensor for real time DNA detection. *1st Annual International IEEE-EMBS Special Topic Conference on Microtechnologies in Medicine and Biology. Proceedings (Cat. No. 00EX451)*, (IEEE), pp 33-35.
13. Crocker JC & Grier DG (1996) Methods of digital video microscopy for colloidal studies. *Journal of colloid and interface science* 179(1):298-310.
14. Lacey SE, He S, Scheres SH, & Carter AP (2019) Cryo-EM of dynein microtubule-binding domains shows how an axonemal dynein distorts the microtubule. *Elife* 8.
15. Kon T, *et al*. (2012) The 2.8 A crystal structure of the dynein motor domain. *Nature* 484(7394):345-350.
16. Kon T, Mogami T, Ohkura R, Nishiura M, & Sutoh K (2005) ATP hydrolysis cycle–dependent tail motions in cytoplasmic dynein. *Nature structural & molecular biology* 12(6):513.
17. Anonymous (*The crystal structure of the dimeric human importin alpha 1 at 2.5 angstrom resolution* (http://www.rcsb.org/structure/4E4V).
18. Cingolani G, Bednenko J, Gillespie MT, & Gerace L (2002) Molecular basis for the recognition of a nonclassical nuclear localization signal by importin beta. *Molecular cell* 10(6):1345-1353.
19. Fayer I & Granek R (2019) Directional stepping model for yeast dynein: Longitudinal-and side-step distributions. *Biophysical journal*.
20. Peker I & Granek R (2016) Multimotor Driven Cargos: From Single Motor under Load to the Role of Motor–Motor Coupling. *The Journal of Physical Chemistry B* 120(26):6319-6326.
21. Yildiz A & Canty JT (2019) Private Communication.
22. Elshenawy MM, *et al.* (2019) Cargo adaptors regulate stepping and force generation of mammalian dynein–dynactin. *Nature chemical biology*:1-9.
23. Bickel T, Jeppesen C, & Marques C (2001) Local entropic effects of polymers grafted to soft interfaces. *The European Physical Journal E* 4(1):33-43.
24. DiMarzio EA (1965) Proper accounting of conformations of a polymer near a surface. *The Journal of Chemical Physics* 42(6):2101-2106.
25. Bameta T, Padinhateeri R, & Inamdar MM (2013) Force generation and step-size fluctuations in a dynein motor. *Journal of Statistical Mechanics: Theory and Experiment* 2013(02):P02030.
26. Cohen O & Granek R (2014) Nucleus-targeted drug delivery: theoretical optimization of nanoparticles decoration for enhanced intracellular active transport. *Nano letters* 14(5):2515-2521.